NTNU – Trondheim
Norwegian University of
Science and Technology

# Investigation of the Wake Flow behind a stepped circular Cylinder using Particle Image Velocimetry

Ina Teutsch

Marine Technology
Submission date: June 2012
Supervisor: Bjørnar Pettersen, IMT

Norwegian University of Science and Technology
Department of Marine Technology

# Investigation of the Wake Flow behind a stepped circular Cylinder using Particle Image Velocimetry

Master Thesis

Ina Teutsch

Norwegian University of Science and Technology

June 8, 2012

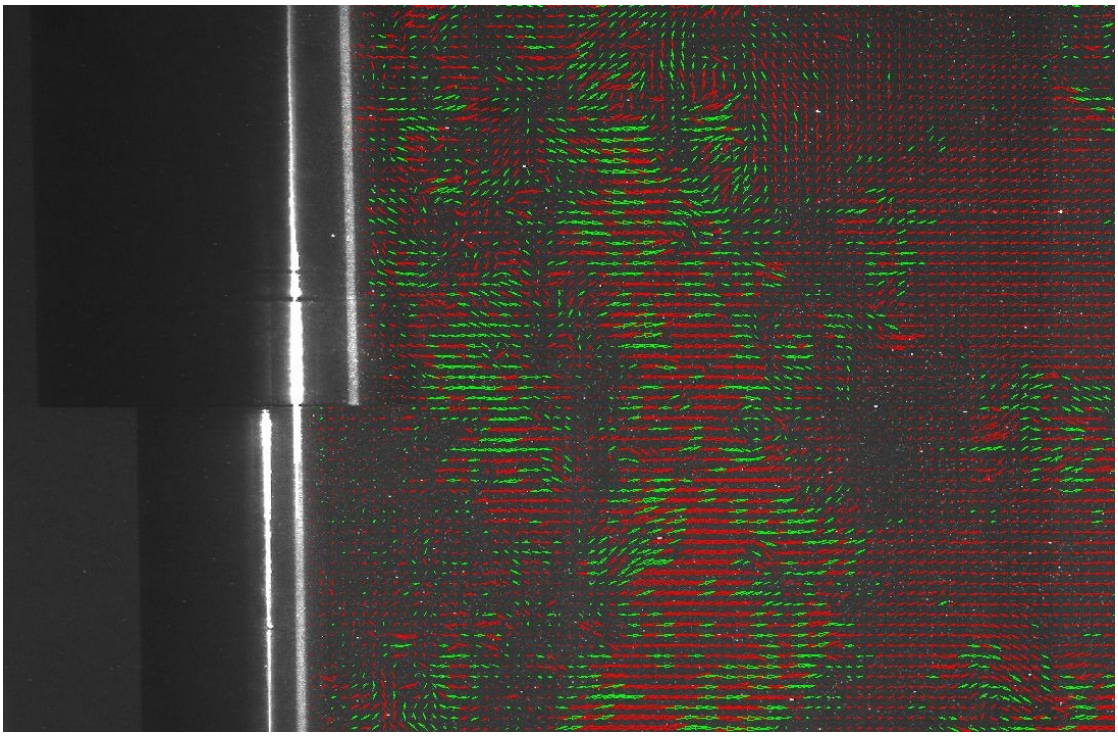

# Contents

**Abstract**

Subject of the present study was the investigation of the wake behind stepped circular cylinders. Experiments were performed using particle image velocimetry (PIV). Cylinder models with diameter ratios D/d=1, D/d=6/5 and D/d=2 were investigated at Reynolds numbers $Re_D = 2243.6, Re_D = 12820.5$ and $Re_D = 51282.1$ with respect to the large diameter. Of main interest were the influences of step size and Reynolds number on the formation of vortex shedding cells. Mean flow characteristics and instantaneous captures of the flow field were analyzed in order to gain insight into vortex development in the wake. Spectral analysis was applied to obtain information on the number of forming vortex shedding cells.

It was found that an increase in $Re_D$ leads to a decrease in eddy formation length $L_f$. At the largest investigated Reynolds number, turbulence gained strong influence on the flow characteristics. An increase in stepsize leads to the development of a large and a small diameter wake with distinct eddy formation lengths $L_{f,L}$ and $L_{f,S}$.

Due to a mismatch in vortex shedding frequencies in the two wakes, vortices that come out of phase connect to subsequent vortices on the same side of the step. This occurs more frequently for a higher diameter ratio.

Several vortex shedding cells were found in the wake of the step cylinders, their number increasing with the step size and differing for different Reynolds numbers.

The wake behind step cylinders was discovered to be strongly three-dimensional. I order to complete the information about flow characteristics, measurements were performed in several parallel vertical and horizontal planes along the cylinder.

PIV proved to be a good method for the investigation of flow features in the wake of step cylinders for the chosen model dimensions and Reynolds numbers.

# 1 Introduction

The flow around circular cylinders has been subject to experimental and numerical investigations for more than a hundred years, see e.g. von Kármán 1911 [6] and Zdravcovich 1997 and 2003 [22]. One reason for this particular interest in the flow

around circular cylinders is the importance of cylindrical bodies in engineering applications. Chimneys and bridge pears can be named as examples, as well as risers and foundations on the sea bottom in marine applications. Despite the long time of preoccupation with circular cylinders, the behaviour of flow in the cylinder wake is still a great challenge for scientists and engineers today.

Sumer and Fredsøe [16] summerized the flow behaviour around a uniform circular cylinder. Laminar vortex shedding begins at approximately $Re_D = 40$. As the Reynolds numer increases, the wake becomes increasingly turbulent.

Recently, the wake flow of uniform circular cylinders has been used as a basis for studies of more complex cylindrical structures. Visscher [20] engaged in a study of the flow behind tapered cylinders. Lewis and Gharib [9] used wavelet analysis to study frequency modulations in the wake of a circular step cylinder. Dunn and Tavoularis [3] focused their electrolytic precipitation study on vortex shedding patterns and vortex interaction in the wake of a step cylinder. Morton and Yarusevych [11, 12] discussed the flow around step cylinders and dual step cylinders, using flow visualization, LDV and numerical simulation.

The mentioned studies showed the common discovery of spanwise vortex shedding in uniform flow. It was found that the tapered [20], as well as the step cylinders [3, 9, 11, 12] created spanwise vortices in multiple cells along their span, each cell characterized by a certain vortex shedding frequency. Distinct vortex shedding cells were found behind large and small diameter section, as well as in the step region [3, 9, 10, 11]. This characteristical vortex shedding in cells took place for $D/d$ >1.55 and $Re_D$>100 [9]. The cell in the step region was characterized by the lowest vortex shedding frequency [3, 9, 11].

Similar flow features as in the experimental studies were found in numerical simulations of step cylinders at different Reynolds numbers, performed by Norberg [14] and Vallès, Andersson and Jenssen [19].

Vortex splitting was discovered especially at high Reynolds numbers and for large diameter ratios [14]: it was discovered that due to the discontinuity, vortex lines came out of phase and formed half-loops with subsequent vortices [19].

In addition to vortex interactions between the distinct cells, downwash from the small into the large diameter region was found [3]. It was seen that the extent of the cell in the step region decreased with increasing Reynolds number [11].

Coming from these findings, the present study investigates the wake flow of step cylinders as shown in Figure 1.1. Step cylinders can apply in marine applications like windmill foundations (see Figure 1.2) and spar buoys for oil storage. The diameter step will play a significant role in the design, as it influences e.g. loads, vibrations and noise emissions of the structures. In marine applications, Reynolds numbers in the transitional and turbulent regime are relevant. Therefore, the present study investigates the wake flow of multiple step cylinders at $Re_D = 2243.6, Re_D = 12820.5$ and $Re_D = 51282.1$.

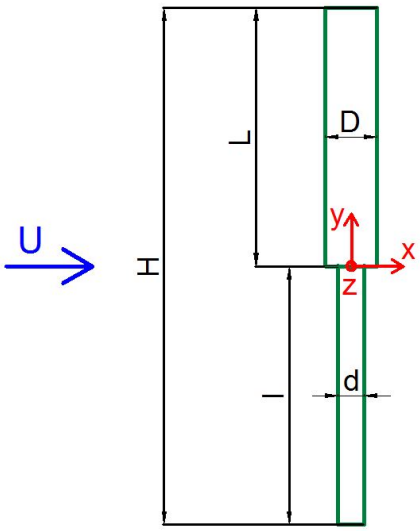


Figure 1.1: Step cylinder, subject to investigations in the present study. Notations as used in the present report.

Figure 1.2: An ocean windmill foundation with a diameter step. [2]

NOMENCLATURE

D- large cylinder diameter

d- small cylinder diameter

D/d- diameter ratio

$f_{ac}$- camera acquisition rate

$f_v$- vortex shedding frequency

H- total cylinder height

L/D- aspect ratio (large diameter section)

l/d- aspect ratio (small diameter section)

$L_f$- eddy formation length

$L_{f,L}$- eddy formation length in the large diameter wake

$L_{f,S}$- eddy formation length in the small diameter wake

PIV- particle image velocimetry PSD- power spectral density $Re = \frac{U_{inflow} * D}{\nu}$- Reynolds number, calculated with respect to the large cylinder diameter

$Re_D$- Reynolds number with respect to the large cylinder diameter

$Re_d$- Reynolds number with respect to the small cylinder diameter

rms- root mean square $St = \frac{f_v * D}{U}$- Strouhal number

$St_D$- Strouhal number with respect to large cylinder diameter U- streamwise velocity component

$U_{inflow}$- inflow or free stream velocity

$U_{mean}$- average value of the streamwise velocity component U during one experiment

V- vertical velocity component

$V_{max}$- maximum value of the spanwise velocity component V during one experiment

$V_{min}$- minimum value of the spanwise velocity component V during one experiment

VC- vortex core

W- spanwise velocity component

x, y, z- cylinder-fixed coordinate system

x', y', z'- tunnel-fixed coordinate system

$\nu$- kinematic viscosity

# 2 Experimental setup

The analysis in the present study is based on experiments performed in a circulating water tunnel in spring 2012.

The circulating water tunnel had a closed transparent test section of 2.5m length with a squared cross section of 0.61x0.61m. The water temperature during the tests was measured as 22 °C. The kinematic viscosity of the water in the tunnel was then found by interpolation from the table in Figure 2.1 as $0.959\frac{mm^2}{s}$.

| Temp. °C | Density $\rho$, kg/m³ | Viscosity $\mu$, $\mu$Pa s from [5] | Viscosity $\mu$, $\mu$Pa s | Kinematic viscosity $\nu$, mm²/s | Uncertainty $\Delta\nu$ | Relative uncertainty $\Delta\mu/\mu$ or $\Delta\nu/\nu$, % | Deviation from [5] % |
|---|---|---|---|---|---|---|---|
| 10 | 999. 7281 | 1306. 9 | 1307 | 1. 307 | 0. 008 | 0. 06 | −0. 02 |
| 15 | 999. 1286 | 1138. 2 | 1138 | 1. 139 | 0. 0015 | 0. 13 | −0. 03 |
| 20 | 998. 2336 | 1002. 0 | 1002 | 1. 003 | 0. 0022 | 0. 22 | −0. 01 |
| 25 | 997. 0751 | 890. 3 | 889 | 0. 892 | 0. 0031 | 0. 35 | −0. 10 |
| 30 | 995. 6783 | 797. 5 | 796 | 0. 800 | 0. 0039 | 0. 49 | +0. 18 |
| 35 | 994. 0635 | 719. 5 | 718 | 0. 723 | 0. 0047 | 0. 65 | +0. 15 |
| 40 | 992. 2473 | 653. 5 | 652 | 0. 658 | 0. 0058 | 0. 89 | +0. 15 |
| 45 | 990. 24 | 596. 3 | 595 | 0. 601 | 0. 0064 | 1. 08 | +0. 16 |
| 50 | 988. 07 | 547. 1 | 547 | 0. 553 | 0. 0071 | 1. 30 | +0. 11 |
| 55 | 985. 73 | 504. 2 | 504 | 0. 511 | 0. 0078 | 1. 55 | +0. 03 |
| 60 | 983. 24 | 466. 6 | 467 | 0. 475 | 0. 0085 | 1. 82 | −0. 09 |
| 65 | 980. 59 | 433. 4 | 434 | 0. 443 | 0. 0092 | 2. 12 | −0. 17 |
| 70 | 977. 81 | 403. 9 | 405 | 0. 414 | 0. 0098 | 2. 42 | −0. 26 |

Figure 2.1: Viscosity of water with respect to the water temperature. [7]

The tunnel provided operation within a speed range of $0.03\frac{m}{s}$ to $1.0\frac{m}{s}$. The turbulence intersity was known to be less than 0.01 of the mean flow speed.

For the stereoscopic PIV performance, polyamid seeding particles with a mean particle diameter of $50\mu m$ were used. A schematic drawing of the PIV performance is presented in Figure 2.2. A detailed description of the procedure in stereoscopic PIV is described by Visscher [20], page 5.

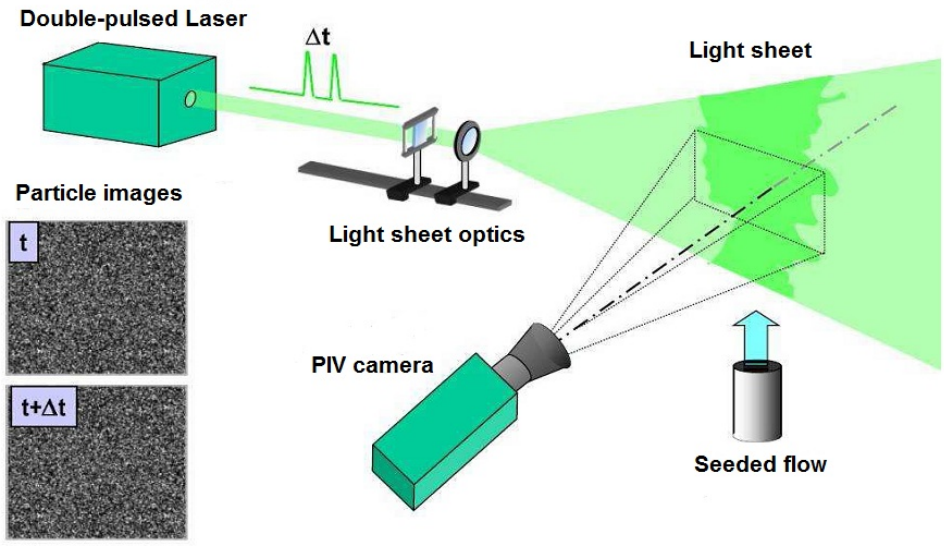


Figure 2.2: Scheme of the PIV performance [23]. Light sheet optics transform the laser beam into a thin light sheet. The laser flashes two times in a short distance $\Delta t$. The particles in the seeded flow are enlightened and the PIV camera captues an images for each flash. The resulting images are compared with respect to the particle positions, in oder to define motions in the flow. Stereoscopic PIV (3C-PIV) uses multiple cameras to capture three-dimensional features in the flow.

The cylinder models were made from PVC in a 3D printer. The coating of the models contained rhodamine particles in order to minimize unintentional reflections of the laser light during the PIV measurements. The models were screwed into a PVC frame with a wall thickness of 4mm, exactly fitting the cross section of the tank (see Figure 2.4). The upstream and downstream edges of the model frame were tapered and rounded in order to avoid interaction of the frame with the fluid (see Section 3.4).

Figure 2.3 shows a plan view of the test section with the measurement setup. The laser was situated at the downstream end of the measurement section. The light-sheet followed the center line of the test section. Two PIV cameras "FlowSense 2M" with a resolution of 1600x1200 px and a maximum double frame rate of 15Hz were positioned on both tunnel sides. 35mm lenses were used on both cameras. The water-filled prisms on the tank sides guaranteed a straight view of the cameras onto the measurement plane through air, glass and water. Figure 2.3 also indicates the field of view for each camera with its respective center line. The cylinder model

was mounted on the upstream end of the measurement plane, in order to be able to capture as much as possible of the wake behind the cylinder.

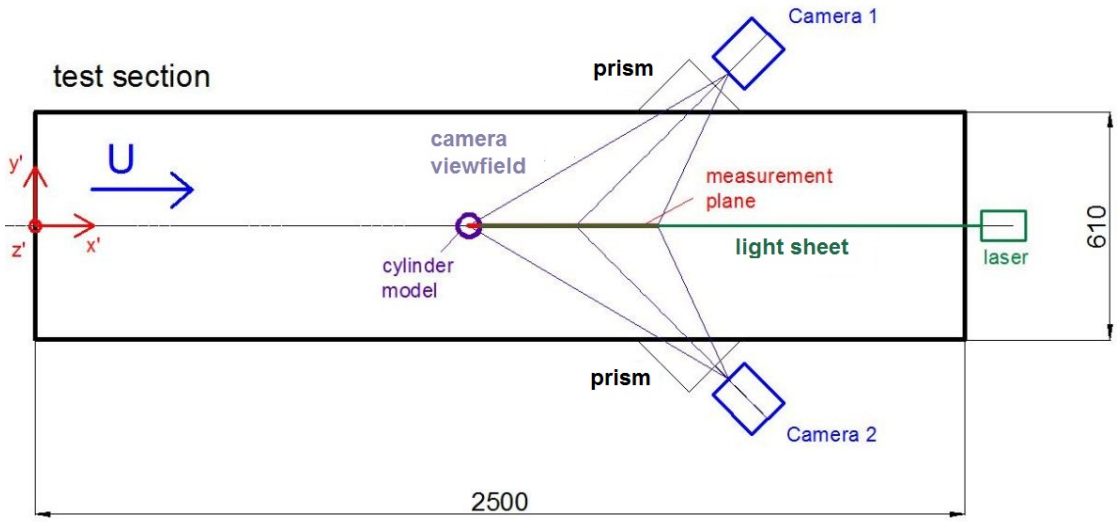


Figure 2.3: Experiment setup (plan view).

Figures 2.4 to 2.6 show captures of the experimental setup. Figure 2.4 presents the measurement section with the model in its frame. Figure 2.5 shows the measurement section from the direction of one of the PIV cameras. In front of the camera, the prism is seen. Figure 2.6 presents the lightsheet optics on the backside of the tank. The laser beam is guided through the light arm and sent through the light sheet optics that transform the beam into a thin lightsheet.

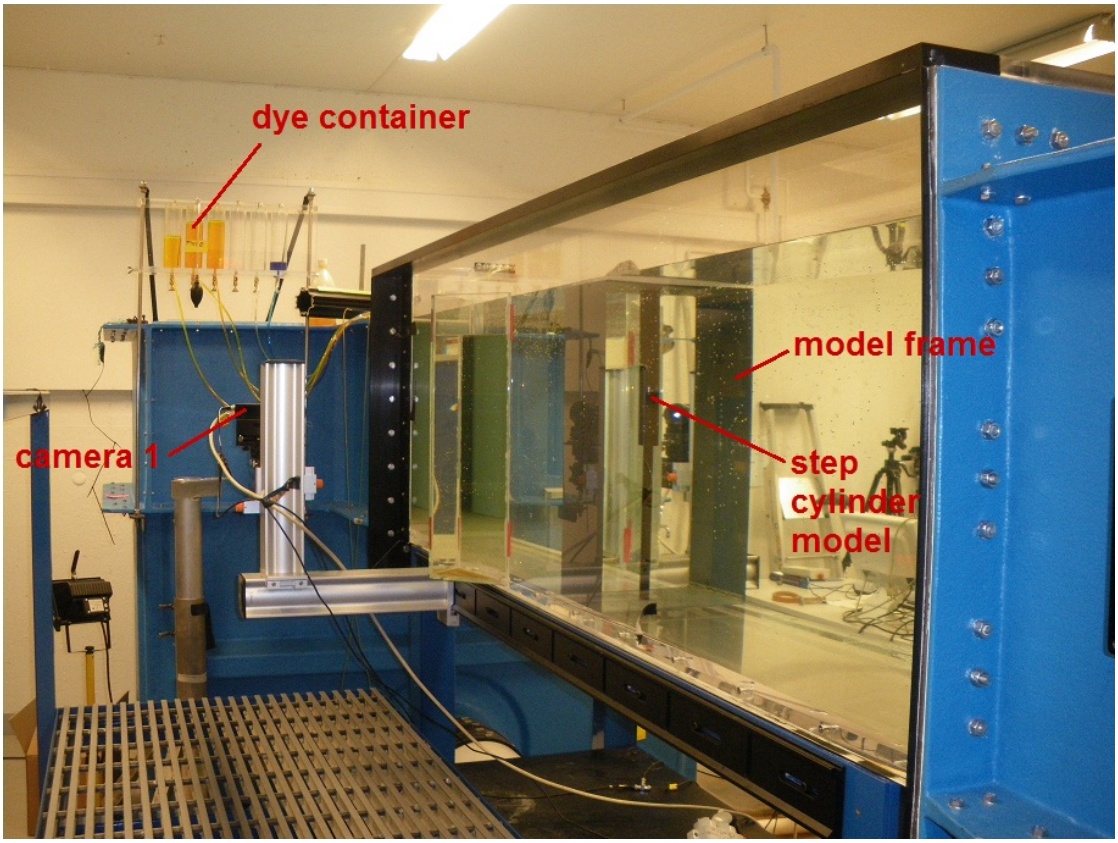


Figure 2.4: View on the measurement section with a step cylinder model.

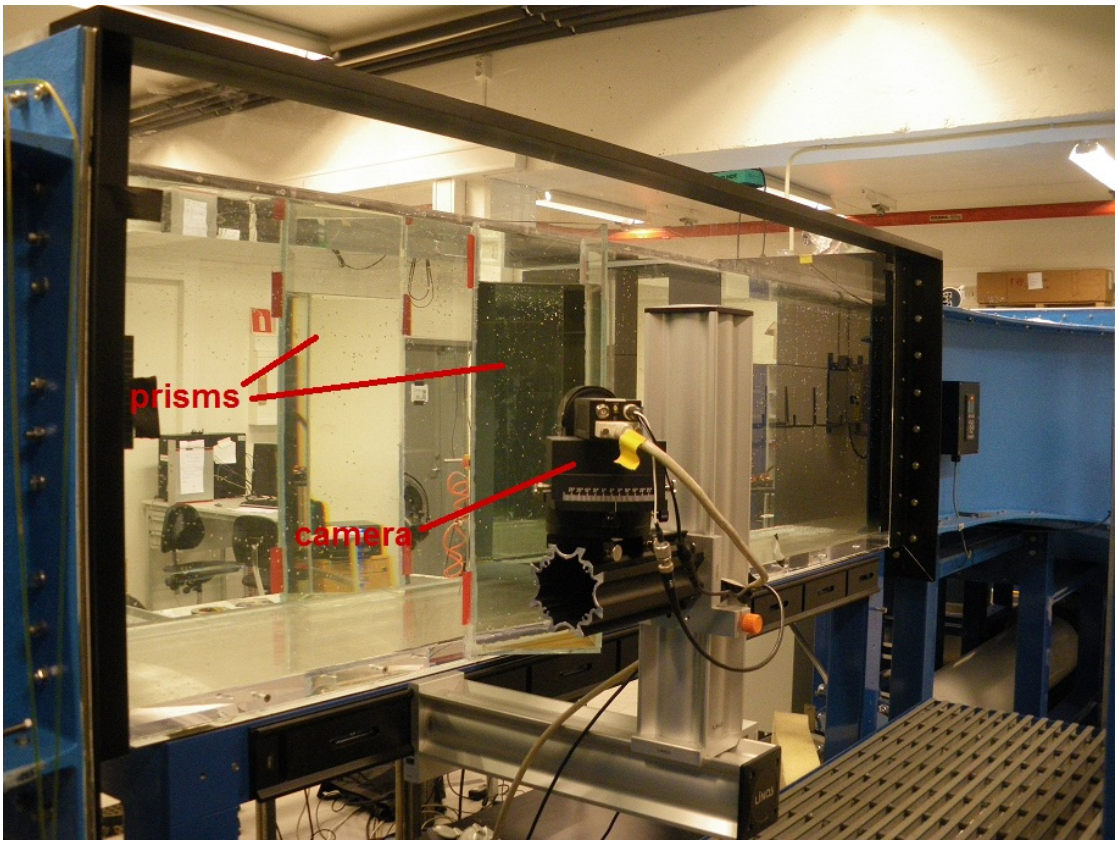


Figure 2.5: Camera view on the measurement section.


Figure 2.6: The lightsheet optics that transform the laser beam into a lightsheet.

# 3 Experimental environment

## 3.1 Tank boundary layer

With the turbulence level in the tunnel being lower than 0.01 of the mean flow speed, the boundary layer in the measurement area was assumed to be sufficiently thin not to influence the experiments.

## 3.2 Laser and Camera Calibration

In the following, the procedure of aligning the laser light sheet to the symmetry plane of the water tunnel and calibrating the cameras to it is described in detail. As a first step, the desired location of the measurement plane and hence the position of the light sheet is to be defined. In the present case, the light sheet position corresponded to the symmetry plane of the water tunnel (see Figure 2.3).

The position of the measurement plane in x'-direction was determined by the position of the prisms and hence the available camera view field. The alignment of the light sheet was done by introducing a self-leveling laser (see Figure 3.1). This laser was placed on the downstream end of the test section and matched with the positions of three independent markings on the symmetry plane of the section (see Figure 3.2). This way, an auxiliary light sheet, representing the symmetry plane of the tank, was spanned. The PIV laser was then aligned to the auxiliary light sheet.

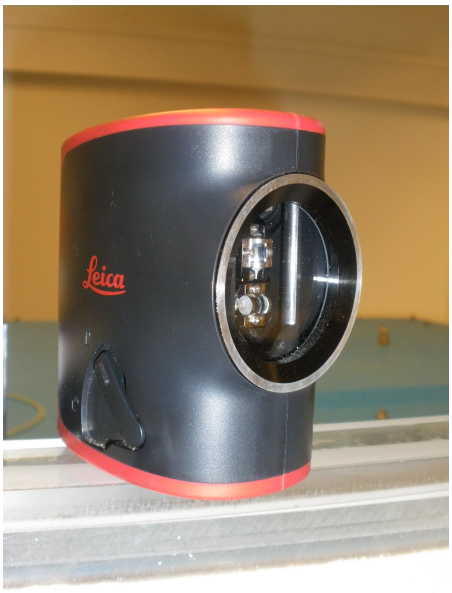


Figure 3.1: Self-leveling laser, used to calibrate light sheet and cameras. Produces horizontal and vertical light sheets. Their orientation is guaranteed by a mechnism of water levels inside the laser. This apparatus is seen inside the laser's eye.

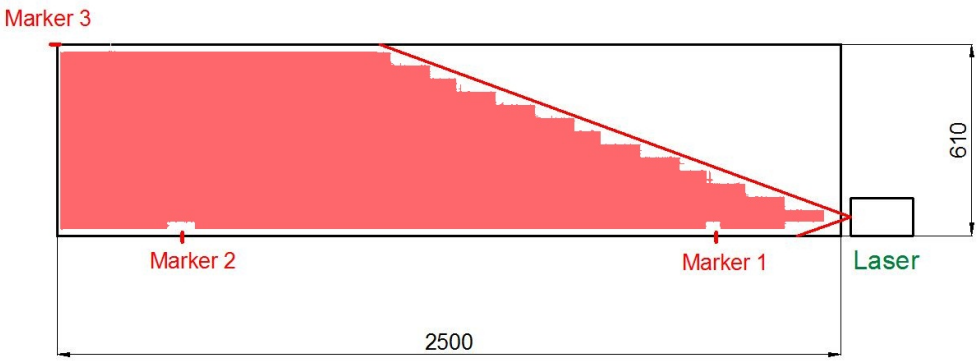


Figure 3.2: Creation of an auxiliary light sheet in the symmetry plane of the measurement section. The light sheet coming from the laser on the right is matched with three markers on the symmetry plane.

Subsequent to adjusting the position of the light sheet, the cameras were focused on it. For this purpose, a calibration target was used. The target consisted of a dark squared plate with a number of equispaced white crosses (see Figure 3.3). The target was placed in the tank in the desired field of view.

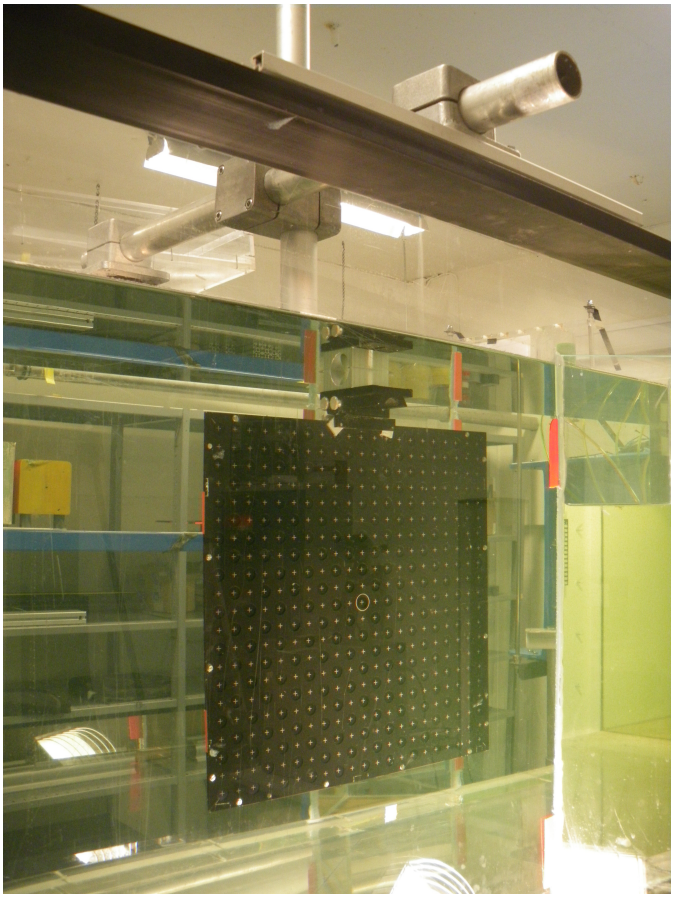

Figure 3.3: Calibration target, mounted in the tank. White crosses are placed in horizontal and vertical distances of 20mm. The middle cross is encircled with a white ring.

The target was adjusted to the symmetry plane of the tank. The position of the target with respect to rotation about z' (see tunnel coordinate system in Figure 2.3) was adjusted with the aid of the self-leveling laser in Figure 3.1: the horizontal line of crosses on the target was adjusted to the horizontal beam produced by the laser, as shown in Figure 3.4. The accuracy of the alignment of the calibration target was highly dependent on the human eye, which led to minimal misalignment of laser and target, which later on caused trouble in data processing (see Chapter 5).

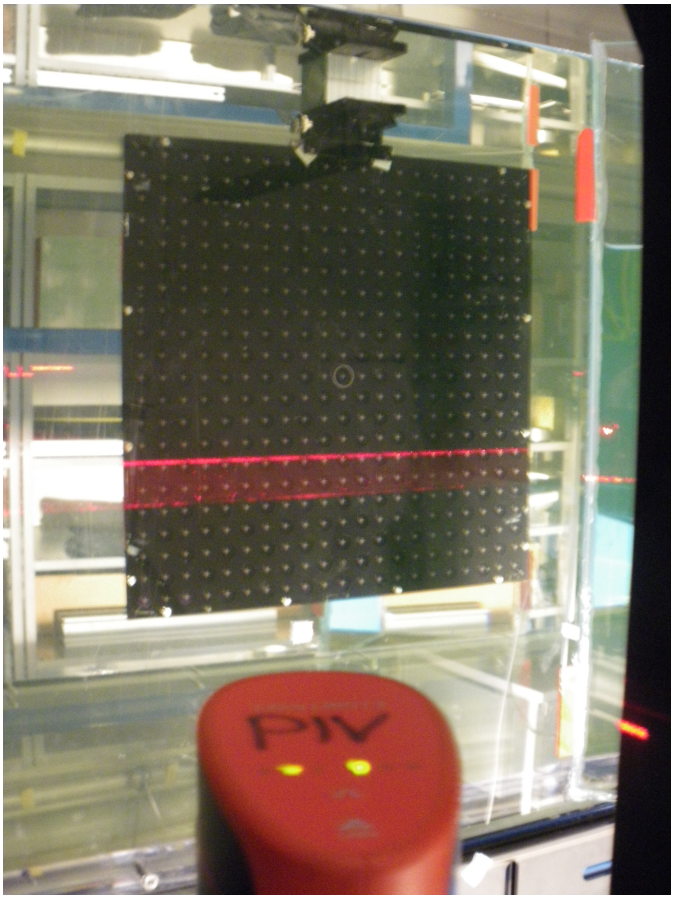


Figure 3.4: The orientation of the target with respect to rotation about z' is being evaluated by producing a perfectly horizontal line with the auxiliary laser (at the bottom of the image) and checking a line of crosses on the target against it. Here, the span of the light sheet becomes visible between the target and the tunnel wall.

Subsequently, the two PIV cameras were aligned to the calibration target. Here, several requirements had to be met:

- The Scheimpflug angle on both cameras had to be fixed at 0° and after adjusting the focus increased until the edges of the images came into focus.
- Both cameras had to see approximately the same field of view (see Figure 3.5). Data was later calculated for all white crosses common to both cameras and interpolated for the additional view outside the field of crosses. Data which was not common data was lost for analyzing.

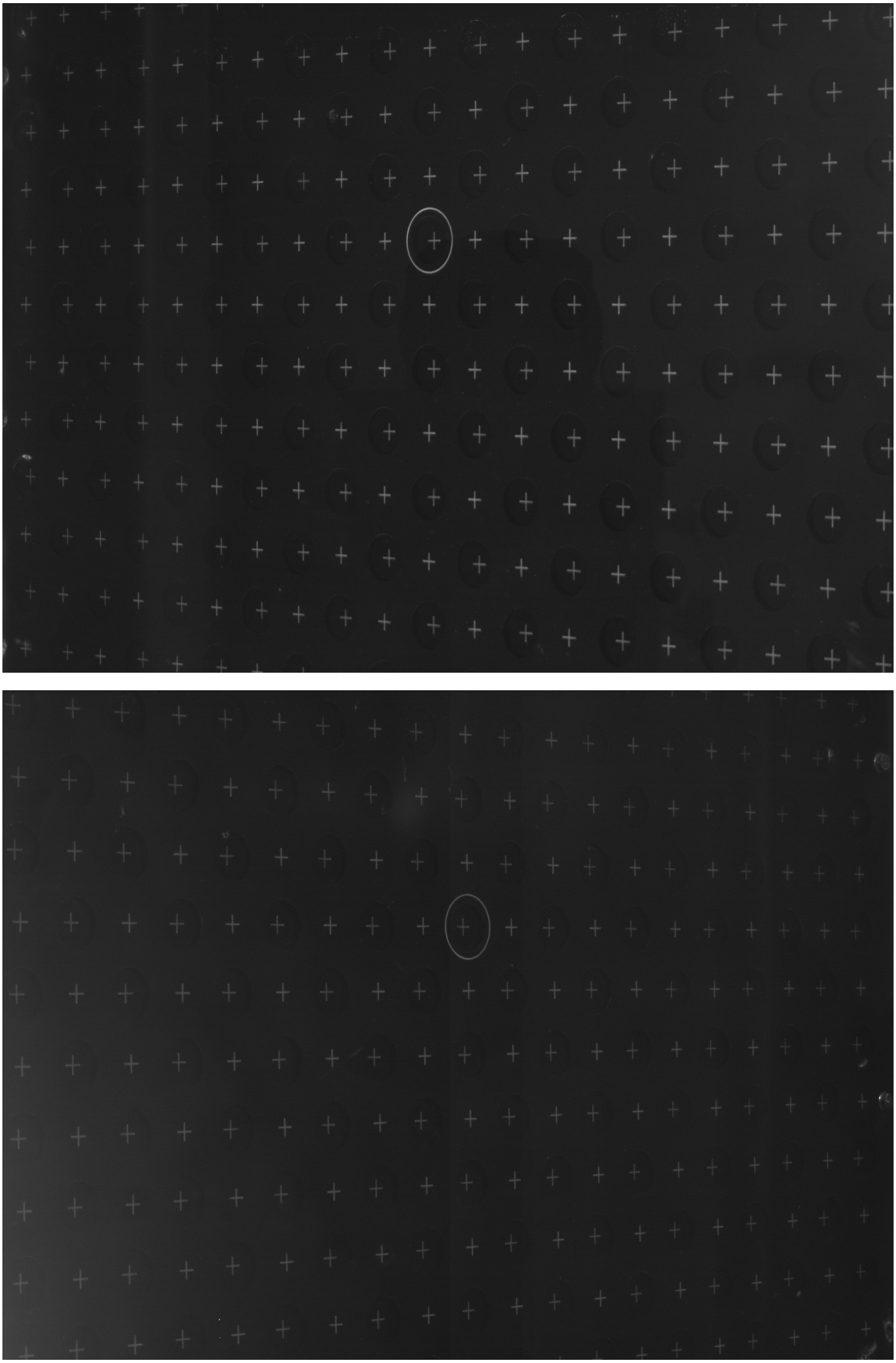

Figure 3.5: View field for camera 1 (top) and camera 2 (bottom). It is important for both cameras to see the same field, since everything seen by less than two cameras will be lost for stereo PIV calculation.

The result of the calibration was a straight laser light sheet, following the symmetry plane of the water tunnel, and the two cameras in focus on a common section of the light sheet.

## 3.3 Light sheet optics

A very thin light sheet is required in PIV performances. In the setup of the present case, where cameras were positioned on both sides of the light sheet, a special requirement was set on both cameras to be able to capture the same particles. Only when this was guaranteed, the software was able to superimpose both camera images. Therefore the light sheet had to be so thin that only a small amout of particles found place in its thickness.
Generally, the light sheet is produced by light sheet optics that transform the laser beam. The optics contain at least one diverging and one converging lense [21]. The configuration of the light sheet optics for the example of two cylindrical lenses is shown in Figure 3.6.

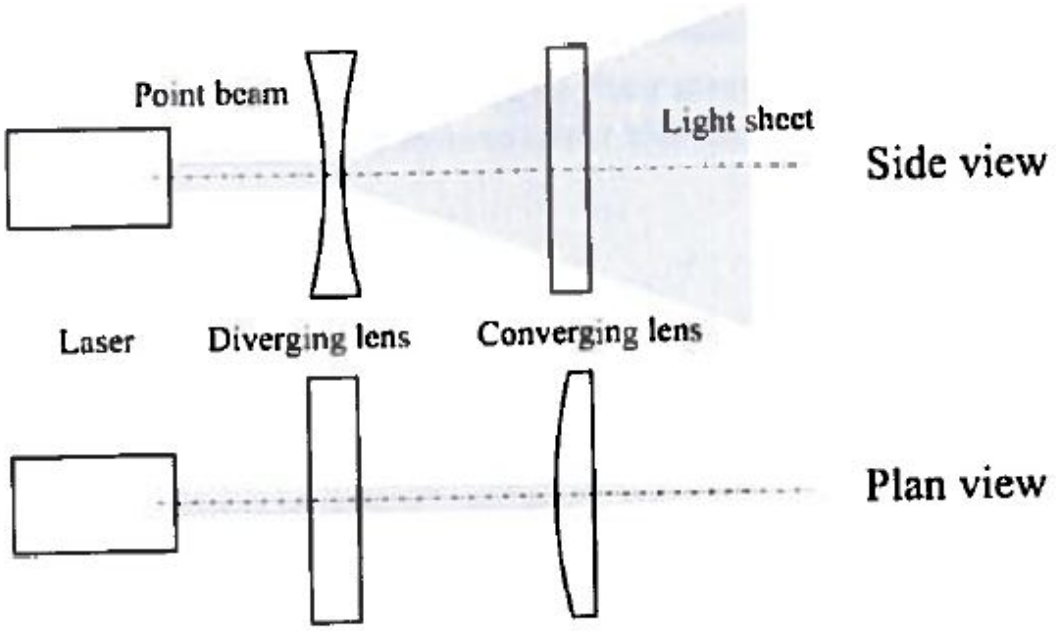


Figure 3.6: Side and plan view of light sheet optics as they are used in PIV. The diverging lens transforms the laser beam into a light sheet, with the converging lens realizing a sufficiently low thickness. [21]

The plan view in Figure 3.6 leads to the conlusion that the lightsheet does not

maintain constant thickness along its entire length. It will rather become thinner until it reaches its waist, and subsequently widen again. It is of interest that the measurement plane is positioned close to the beam waist, in order to gain a possibly thin light sheet and therefore accurate measurement results. From figure 3.6 one can imagine that the axial distance between both lenses has an effect on the position of the beam waist. The measurement location in the present case was predetermined by the position of the prisms (see Figure 2.3) and consequently the view field of the cameras. The preferable position of the beam waist was therefore known. Several spacers for variation of the distance between the lenses in the optics were available. Those were subsequently inserted into the light sheet optics and the corresponding distance of the beam waist from the exit of the light sheet optics was measured. This test was done in air. Table 3.1 presents the results of the test.

| Spacer] | Beam waist position |
|---|---|
| 0 | 1640mm |
| 6mm | 900mm |
| 20mm | 470mm |
| 40mm | 250mm |

Table 3.1: Beam waist position with respect to the position where the light sheet leaves the light sheet optics.

The table shows that the shorter the distance between the lenses, the further away from the optics the position of the beam waist. As a result, no spacer except for the built-in spacer of the hardware was used in the present study, in order to guarantee a beam waist close to the measurement plane. The light sheet thickness measured at the position of the cylinder model was 2mm.

## 3.4 Influence of the model frame

All cylinder models were fixed in the tank by a model frame (see Chapter 2). Before starting the cylinder experiments, the influence of the model frame on the flow field was investigated and compared to free stream measurements. The evaluation method is described in Chapter 5. It was found that the model frame did not change the features of the incoming flow in the measurement plane.

# 4 Experiment matrix

Several cylinder models, each with a certain diameter ratio, were exposed to an amount of constant flow speeds in the tank. The models and experiment cases are presented in Figure 4.1 and in Table 4.1, respectively. The cylinder models had a common height of H=600mm. The step was located in the middle of the cylinder span. In the regular setup, the models were mounted vertically, with the large above the small diameter section.

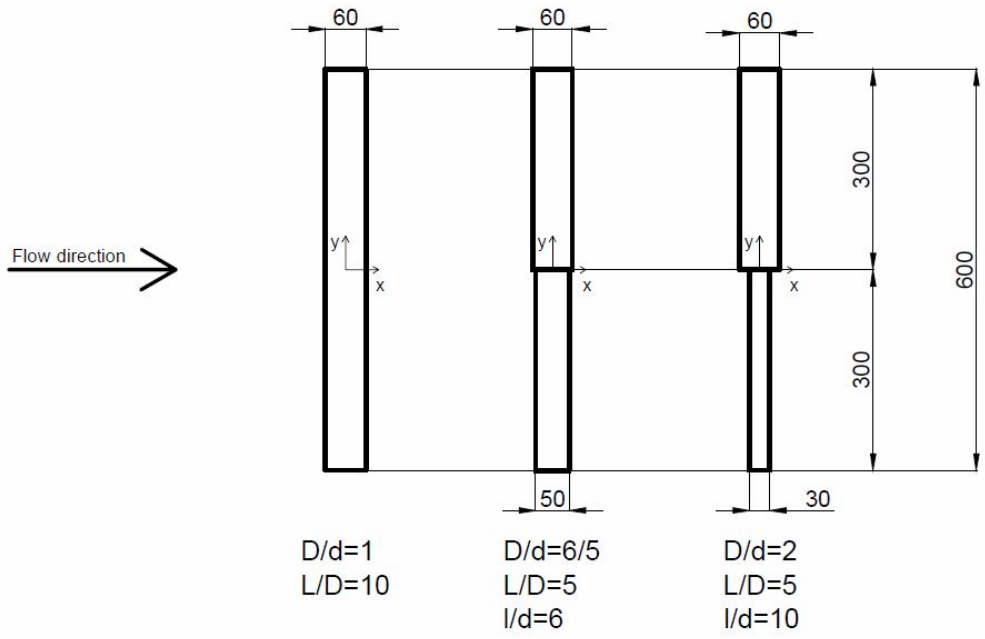


Figure 4.1: Examined cylinder models with their diameter and aspect ratios. Aspect ratios are given for the large and the small diameter section respectively as L/D and l/d. Cylinder-fixed coordinate systems. All dimensions in mm.

| Experiment no. | Setup | Diameter ratio D/d | Aspect ratio L/D (l/d) | Flow velocity [m/s] | $Re_D(Re_d)$ |
|---|---|---|---|---|---|
| 4.051 | regular | 60/60=1 | 600/60=10 | 0.8 | 51282.1 |
| 4.052 | | | | 0.2 | 12820.5 |
| 4.054 | | | | 0.035 | 2243.6 |
| 4.024 | | 60/50 | 300/60=5 (300/50=6) | 0.035 | 2243.6 (1869.7) |
| 4.041 | | 60/30=2 | 300/60=5 (300/30=10) | 0.8 | 51282.1 (25641.0) |
| 4.042 | | | | 0.2 | 12820.5 (6410.3) |
| 4.044 | | | | 0.035 | 2243.6 (1121.8) |
| 5.054 | displacement 15mm | 60/60=1 | 600/60=10 | 0.035 | 2243.6 |
| 5.044 | | 60/30=2 | 300/60=5 (300/30=10) | 0.035 | 2243.6 (1869.7) |
| 5.154 | displacement 22.5mm | 60/60=1 | 600/60=10 | 0.035 | 2243.6 |
| 5.144 | | 60/30=2 | 300/60=5 (300/30=10) | 0.035 | 2243.6 (1869.7) |
| 5.254 | displacement 30mm | 60/60=1 | 600/60=10 | 0.035 | 2243.6 |
| 5.244 | | 60/30=2 | 300/60=5 (300/30=10) | 0.035 | 2243.6 (1869.7) |
| 6.041 | Lightsheet in x-z-plane | 60/30=2 | 300/60=5 (300/30=10) | 0.8 | 51282.1 (25641.0) |
| 6.044 | | | | 0.035 | 2243.6 (1869.7) |
| 6.144 | Displaced x-z-lightsheet, 15mm | 60/30=2 | 300/60=5 (300/30=10) | 0.035 | 2243.6 (1869.7) |
| 6.244 | Displaced x-z-lightsheet, 30mm | 60/30=2 | 300/60=5 (300/30=10) | 0.035 | 2243.6 (1869.7) |
| 6.344 | Displaced x-z-lightsheet, -15mm | 60/30=2 | 300/60=5 (300/30=10) | 0.035 | 2243.6 (1869.7) |
| 6.444 | Displaced x-z-lightsheet, -30mm | 60/30=2 | 300/60=5 (300/30=10) | 0.035 | 2243.6 (1869.7) |

Table 4.1: Matrix of experiments discussed in the present report. Experiment numbers according to Teutsch [18] created from experiment series, variation, cylinder model and inflow velocity. Reynolds numbers are given for large and small diameter sections respectively. The matrix shows a selection of experiments from a larger set of measurements performed in this connection.

As the vortex shedding frequency in the cylinder wake varies with the Reynolds number, the aqcuisition frequency of the PIV cameras was adjusted to the respective inflow velocity in order to be able to capture vortices in a comparable manner for all cases. This was done by initially assuming a Strouhal number of $St_D = 0.2$

for all cases. The vortex shedding frequency for each inflow velocity was then calculated as $f_v = \frac{St_D * U_{inflow}}{D}$. The acquisition frequency was chosen 10 to 20 times the calculated vortex shedding frequencies, in order to capture full development of the vortices with a sufficient resolution in time. Here, the maximum double frame rate of 15Hz of the PIV cameras had to be respected. Values for the calculation of the acquisition frequency are presented in Table 4.2.

| Inflow velocity $U_{inflow}[\frac{m}{s}]$ | Assumed $St_D$ | Calculated $f_v[\frac{1}{s}]$ | Calculated $f_{ac}$ | Chosen $f_{ac}$ |
|---|---|---|---|---|
| 0.035 | 0.2 | 0.117 | 20*0.117=2.3Hz | 2Hz |
| 0.2 | 0.2 | 0.667 | 15*0.667=10.0Hz | 10Hz |
| 0.8 | 0.2 | 2.667 | 15*2.667=40.0Hz | 15Hz |

Table 4.2: Choice of the acqusition frequency of the cameras for the respective velocity conditions. Calculation with respect to an assumed Strouhal number of 0.2.

# 5 Data processing

## 5.1 General

The PIV postprocessing program VidPIV was used to treat the data delivered by the PIV cameras. Postprocessing included the correlation of the two frames from both cameras to each other, data filtering and the transformation from 2D to 3D velocity results. The final result was created by applying a grid with an interrogation size of 16x16 px and an overlap of 8x8 px. This image was imported into MATLAB, where velocity and vorticity plots were created.

The first data sets imported into the VidPIV postprocessing program were the results of free stream measurements without the presence of any cylinder in the flow. After running the postprocessing procedure and importing the resulting files into MATLAB, conspicuous features were observed in the plots for the averaged velocity components (see Figure 5.1): while the flow field without a present model was expected to show a constant velocity component in x-direction, with zero velocity along the remaining axes, all plots included a certain distortion. This was assumed to be a result of misalignment of laser light sheet and calibration target,

due to the inaccuracy of the human eye (see Chapter 2). The problem appeared at all measured inflow velocities. As an example, results from an inflow velocity of $U_{inflow} = 0.035\frac{m}{s}$ are shown in the following.

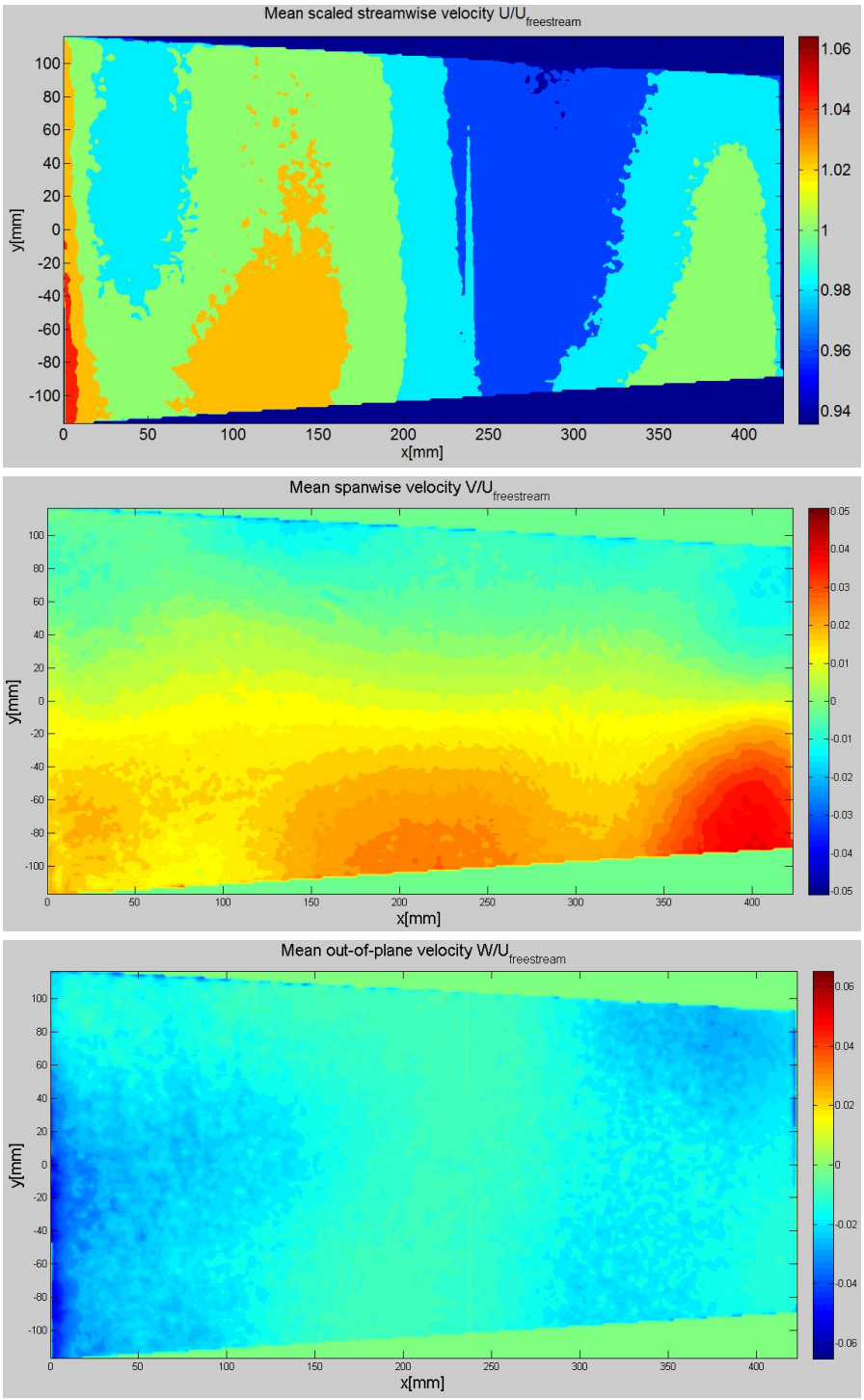


Figure 5.1: Distortion in the mean velocity plots of a freestream measurement at $U_{inflow} = 0.035\frac{m}{s}$. Velocity components from top to bottom: U, V, W. All velocity components have been normalized with the inflow velocity.

## 5.2 Alternative approaches

Several methods were applied in order to eliminate the distortions. Those methods and their achievements are outlined in this section.

### 5.2.1 Disparity map

At first, a disparity map was applied. This is an optimization tool that is included in the VidPIV software. The disparity between the images from the two cameras shall be minimized. The procedure of creating and implementing a disparity map is done in the following way:

To begin, a sample of images from the data set is imported into VidPIV and de-warped. The PIV file is saved as the original file. After the de-warping step, the disparity map node is introduced (see Figure 5.2). In its grid description, the largest possible interrogation size is chosen, which corresponds to windows of size 256x256px. A grid separation of 128px is applied.

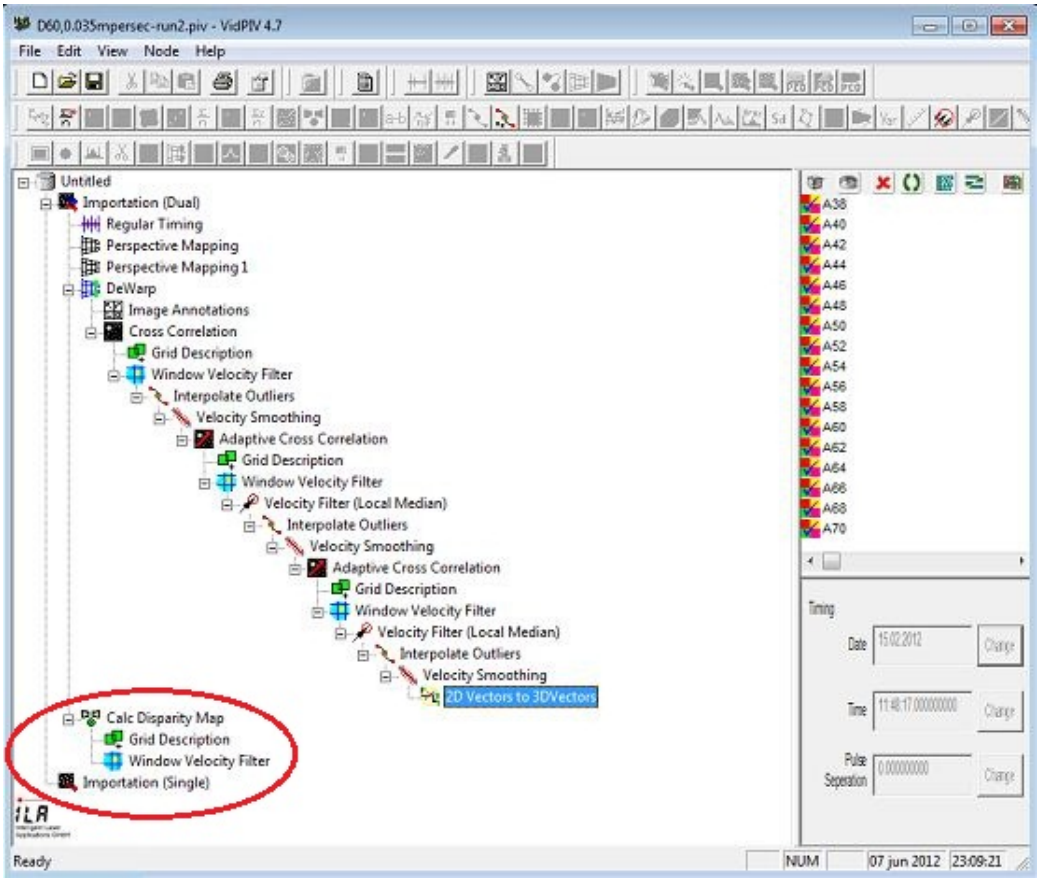


Figure 5.2: The VidPIV postprocessing tree, including a node for the creation of a disparity map.

In the disparity map properties, "simple shift" is chosen for the 3D camera setup (see Figure 5.3, left image). It is not obvious which of the possible parameter combinations will lead to the strongest minimization of disparity. All possible parameter combinations must be tried out.

The influence of the chosen parameters is investigated in the following manner: a screenshot of the selected properties is taken as done in Figure5.3. After calculating the disparity map for all images, a window filter is introduced (see Figure 5.2). Figure 5.3, right image, shows the properties of the window velocity filter after calculating a disparity map for all imported images. A screenshot of the window filter properties is taken. Preferably, the data cloud is located symmetrically about the origin of the coordinate system. At the end of the procedure, the screenshots will be compared with the result, in order to verify the success of the disparity correction.

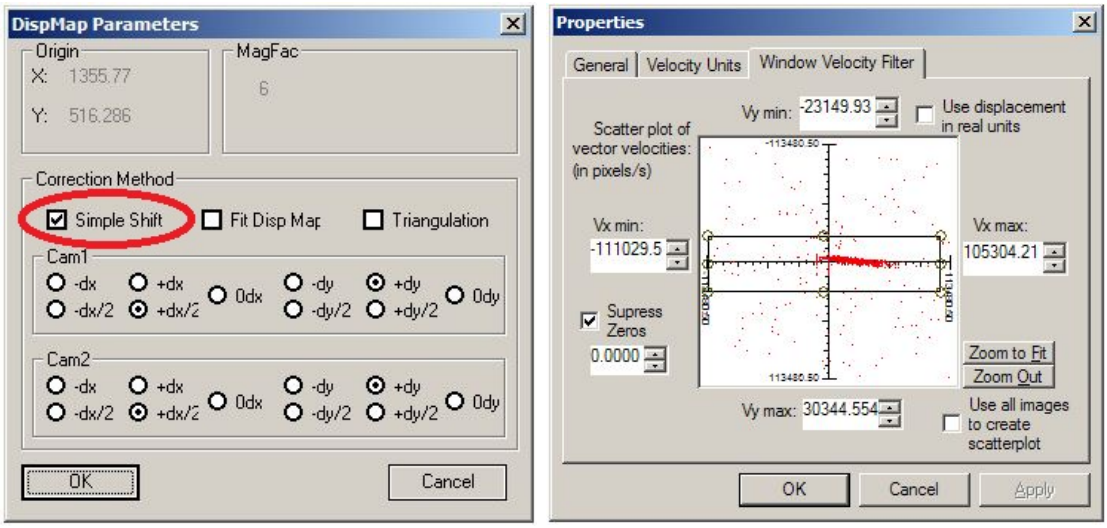


Figure 5.3: Left image: Disparity Map parameters. In the case of a 3D camera setup, "simple shift" must be selected. The final result is influenced by the choice of the parameter combination. Right image: Arrangement of the data cloud after the calculation of disparity maps.

The filter helps finding a vector plot with few extreme values (see Figure 5.4). This plot will be used for further calculations.

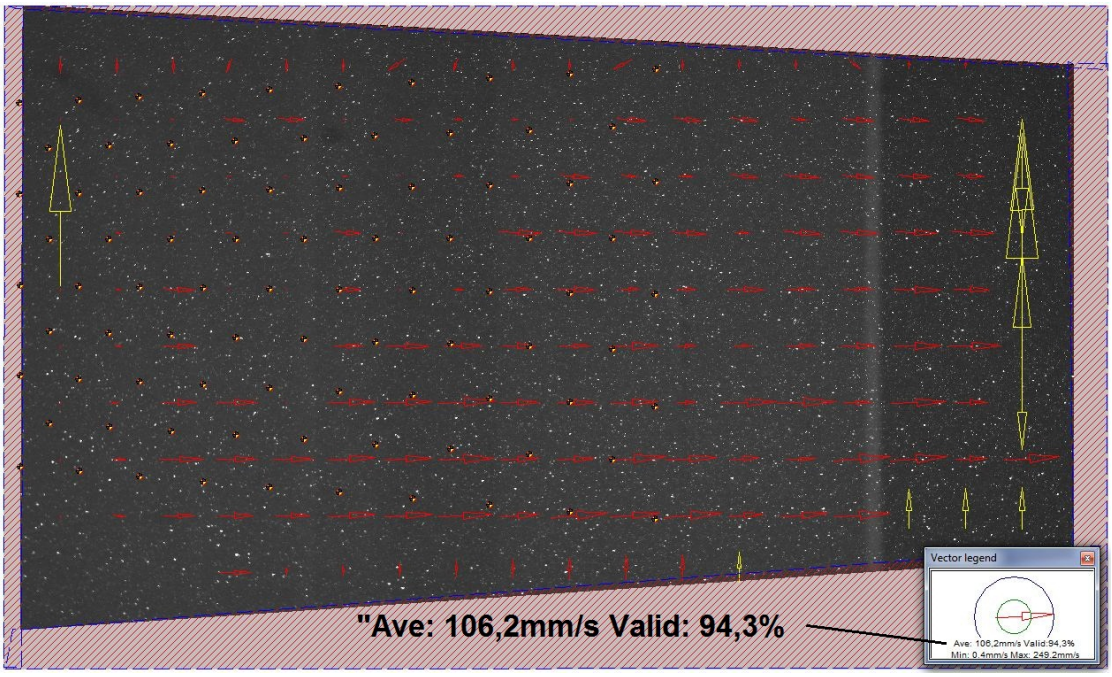


Figure 5.4: Resulting plot after the application of the window filter. With 94.3%, this is a plot with few outliers.

The node "window velocity filter" is now deleted from the postprocessing tree. Back to the plot in the disparity map node, "Draw grid-point" and "Don't draw filtered vectors" are chosen in the properties of the plot (see Figure 5.5). Vectors that obviously represent extreme values can now be filtered out manually by clicking on the grid-point (see Figure 5.6).

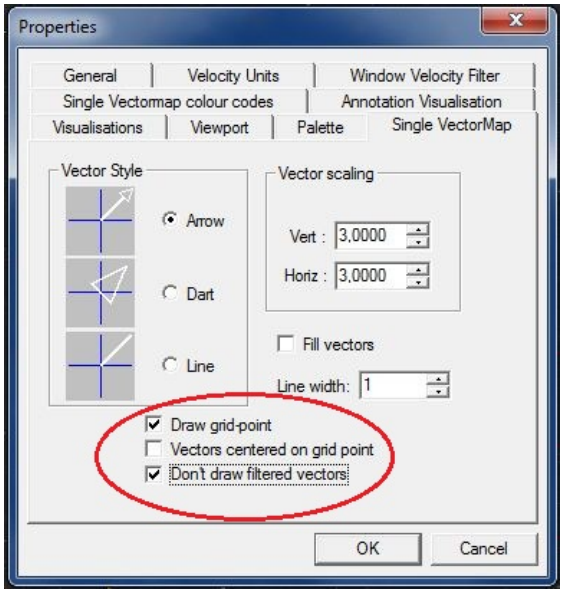


Figure 5.5: Properties of the resulting plot after applying the disparity map.

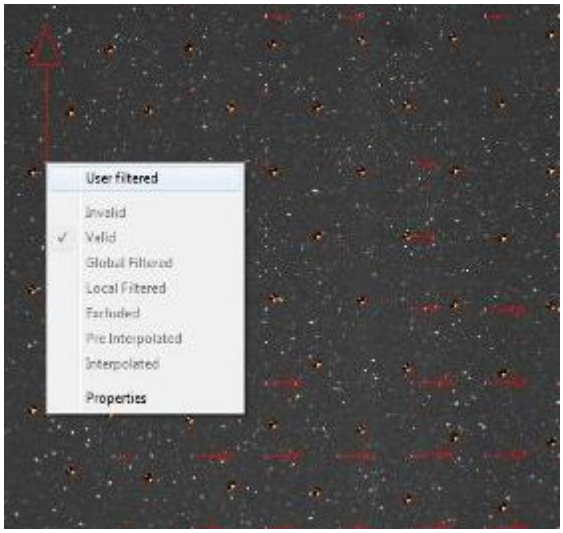


Figure 5.6: User-filtering of outlying vectors.

The corrected plot is immediately exported as a vector map: the disparity map has been created. The export includes five files. The files with endings ".dm1" and ".dm2" are used in the following.
The disparity map is introduced to the mapping nodes on top of the processing tree. In the first mapping, the file ending on ".dm1" is loaded and applied by pressing "optimize". A pop-up window confirms the optimization (see Figure 5.7). In the second mapping node, the same is done for the file with the ending .dm2. Again, "opimize" is pressed and the confirmation appears.

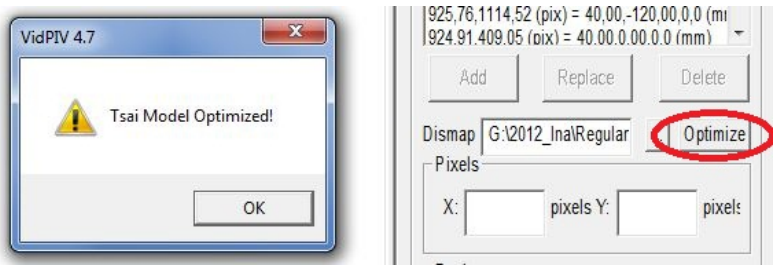


Figure 5.7: Minimizing the disparity beween the images by including the created disparity map in the data mapping.

In a next step, the de-warped images are deleted from the original file and the de-warping is repeated with the optimized mapping. In the disparity map node, the chosen parameters are applied once more and from the data cloud in the filter node, it is seen whether the disparity map has caused any improvement. This is

the case if the data cloud has moved closer to the origin of the coordinate system. If not, another set of parameters should be selected and the procedure repeated. In the present case, Figure 5.8 presents the result of the procedure when using the parameter set in Figure 5.3, left image. Compared to the screenshot taken in the beginning of the procedure (Figure 5.3, right image), this is not optimal, since the data cloud has shifted even further away from the origin. Figure 5.9 presents the data cloud resulting from an alternative set of parameters (see left image in the figure). The data cloud is now arranged closely and almost symmetrically to the origin. This parameter set was therefore chosen for the final disparity map.

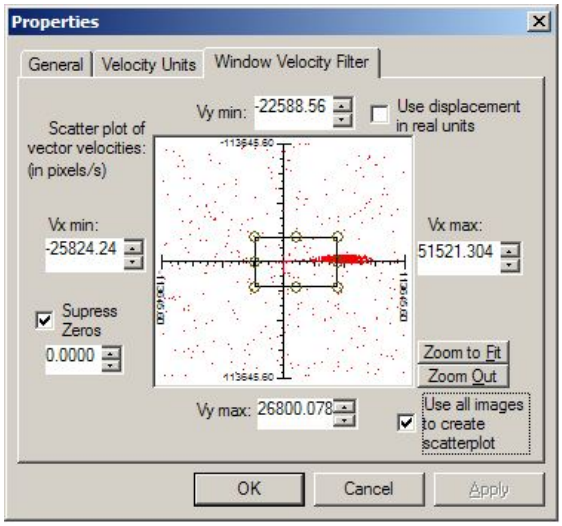


Figure 5.8: Properties of the window velocity filter that follows the disparity map calculation. In an ideal case, all data points are arranged symmetrically about the coordinate origin.

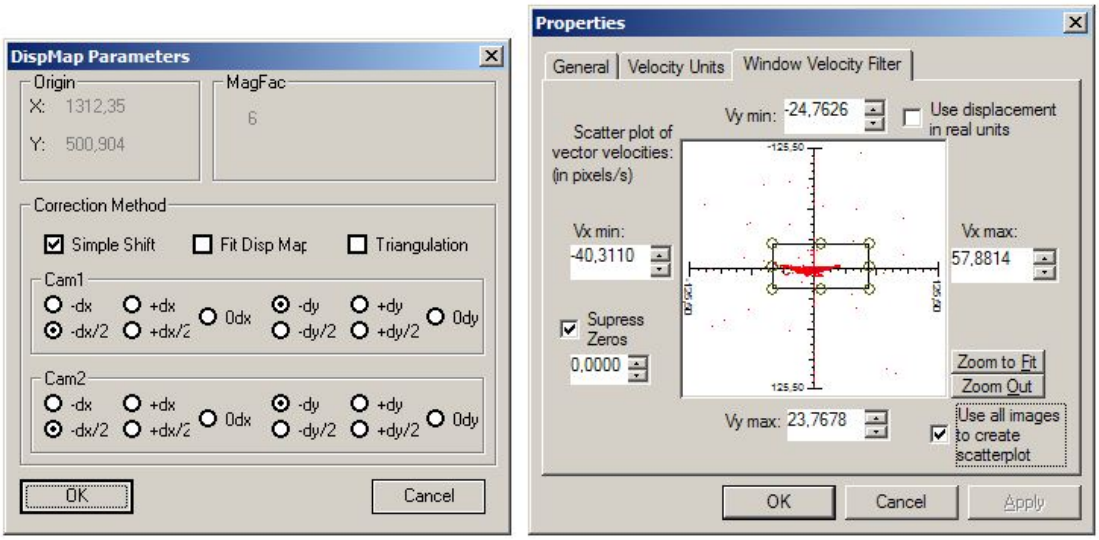


Figure 5.9: Another possible choice of disparity map parameters with the resulting data cloud in the velocity filter. This set of parameters is to prefer in the present case, since it arranges the data cloud closer to the origin of the coordinate system than the previously selected parameter combination.

In Figure 5.10, the effect of the introduction of a disparity map is shown in terms of a resulting mean velocity plot in comparison with the freestream run processed without optimization. The streamwise velocity component U was chosen for the comparison. It is seen that the introduction of a disparity map slightly reduced the distortion, but with an altogether low effect. Minimum and maximum magnitude of the distortion seem to have remained the same. The application of a disparity map was therefore not effective in this case. For quantitative comparison, Table 5.1 lists the meanvalues of the streamwise velocity for all applied procedures. In the present case it is seen that despite the application of a disparity map, the mean value did not change and remained higher than the true value.

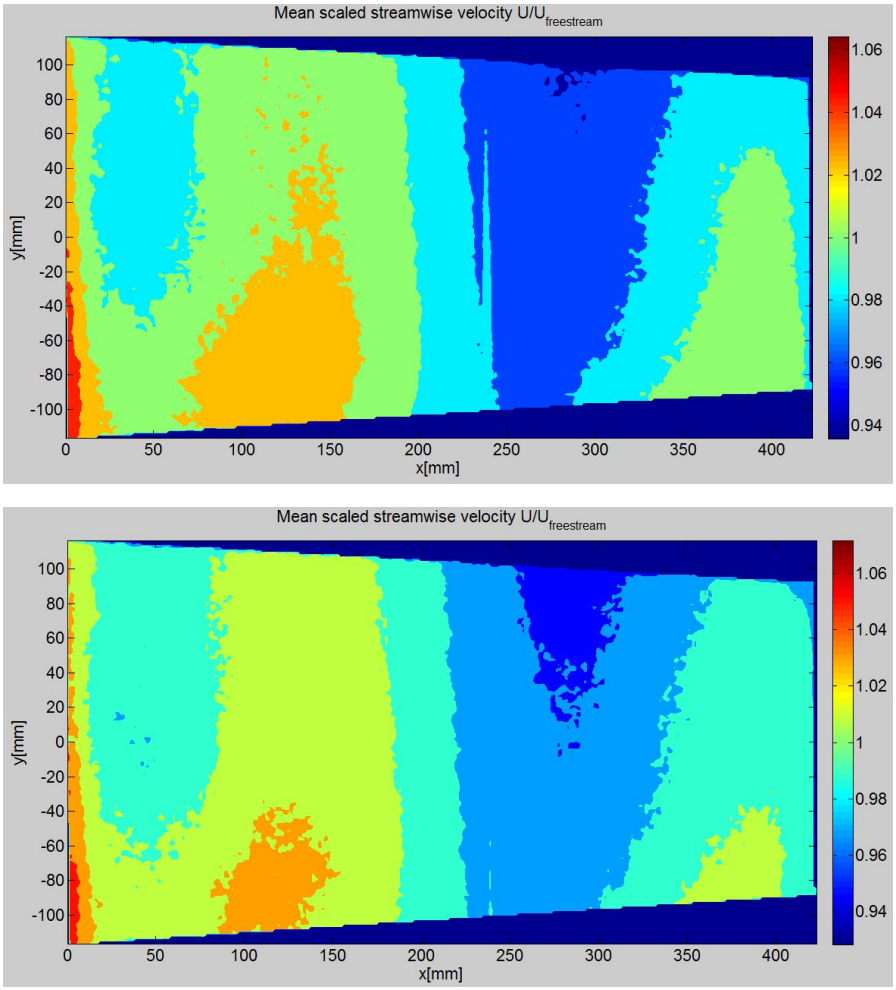


Figure 5.10: Comparison of the free stream result without (top plot) and with (bottom plot) disparity map.

### 5.2.2 Postprocessing program PivView

Since the application of a disparity map did not result in the desired elimination of the distortion, the camera data was now imported into another postprocessing program, called PivView, with the expectation of a more effective de-warping strategy. Just like in VidPIV, a number of filters and interrogation steps were applied.

In a first approach, the data was processed without the application of a disparity map. A second run included the optimization with a disparity map. Figure 5.11 shows the result from the PivView runs with and without disparity map.

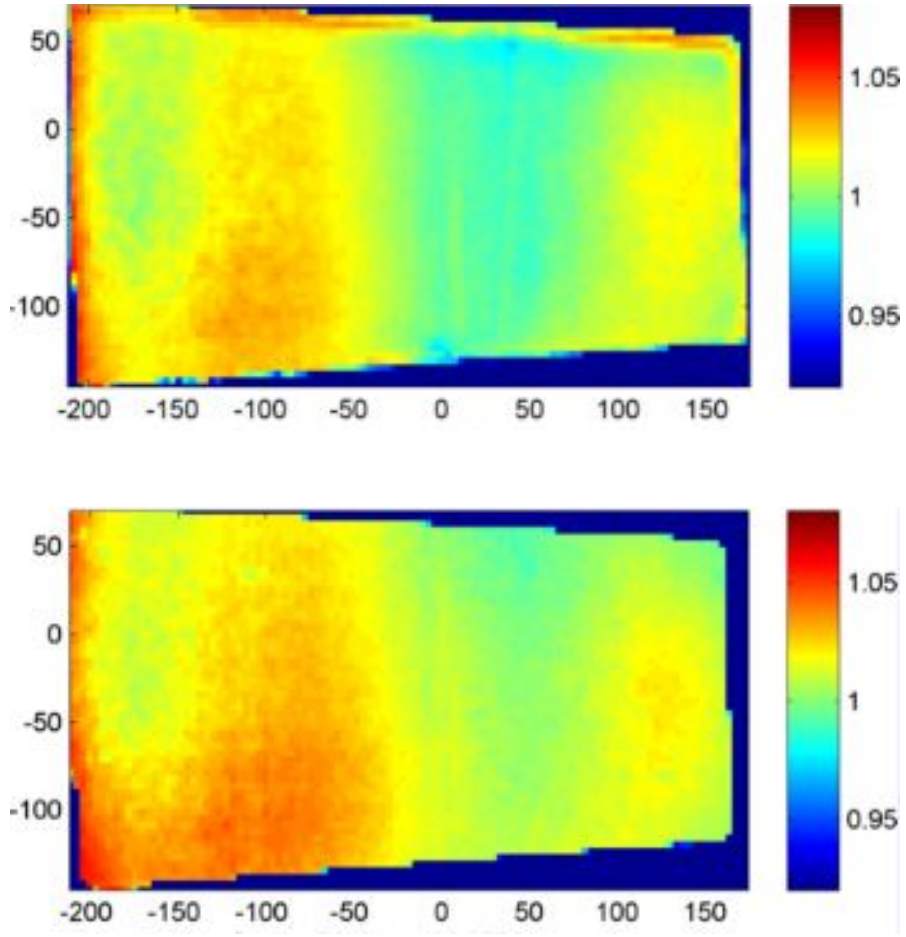


Figure 5.11: Results of the postprocessing procedures in Pivview for a freestream run at $U_{inflow} = 0.035m/s$. Top image: no disparity map; bottom image: processed with disparity map.

It is obvious that although the distortion could be reduced by using Pivview and even further diminished by the application of a disparity map, deviations are still present. The images however prove by a shape of the distortion similar to the one in Figure 5.1 that the distortion was not internally created in VidPIV. Values for U are found in Table 5.1.

### 5.2.3 Variation of the camera setup

Since the use of another program, even with the application of a disparity map, did not prove to be satisfying with respect to the elimination of the distortion, it was now tested if a setup with both cameras on the same side of the water tunnel resulted in a more logical mapping. This setup will be refered to as Setup 2. It is sketched in Figure 5.12. In order to remain with a 3C setup, able to handle all

velocity components, Camera 1 was positioned in front of the prism, while camera 2 looked straight into the tank. In order to achieve the largest possible field of view, a lens of size 24mm was now used on camera 2. However, the positioning of Camera 2 altered the size of the field of view from 380x180mm in the previous setup to 300x220mm in the new setup.

A freestream run at $U_{inflow} = 0.035m/s$ was captured and processed in VidPIV. This was done with and without the application of a disparity map. The resulting streamwise velocity plots are given in Figure 5.13.

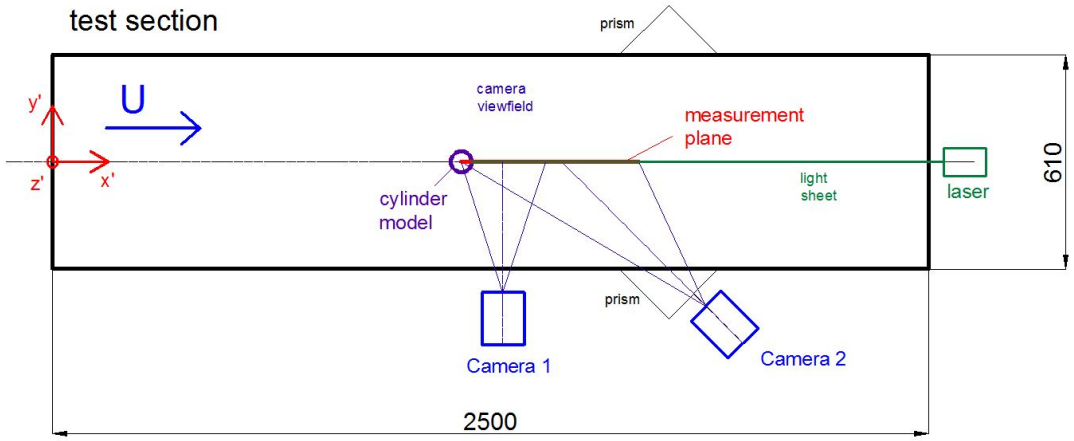


Figure 5.12: Alternative setup with both cameras on the same side of the measurement section.

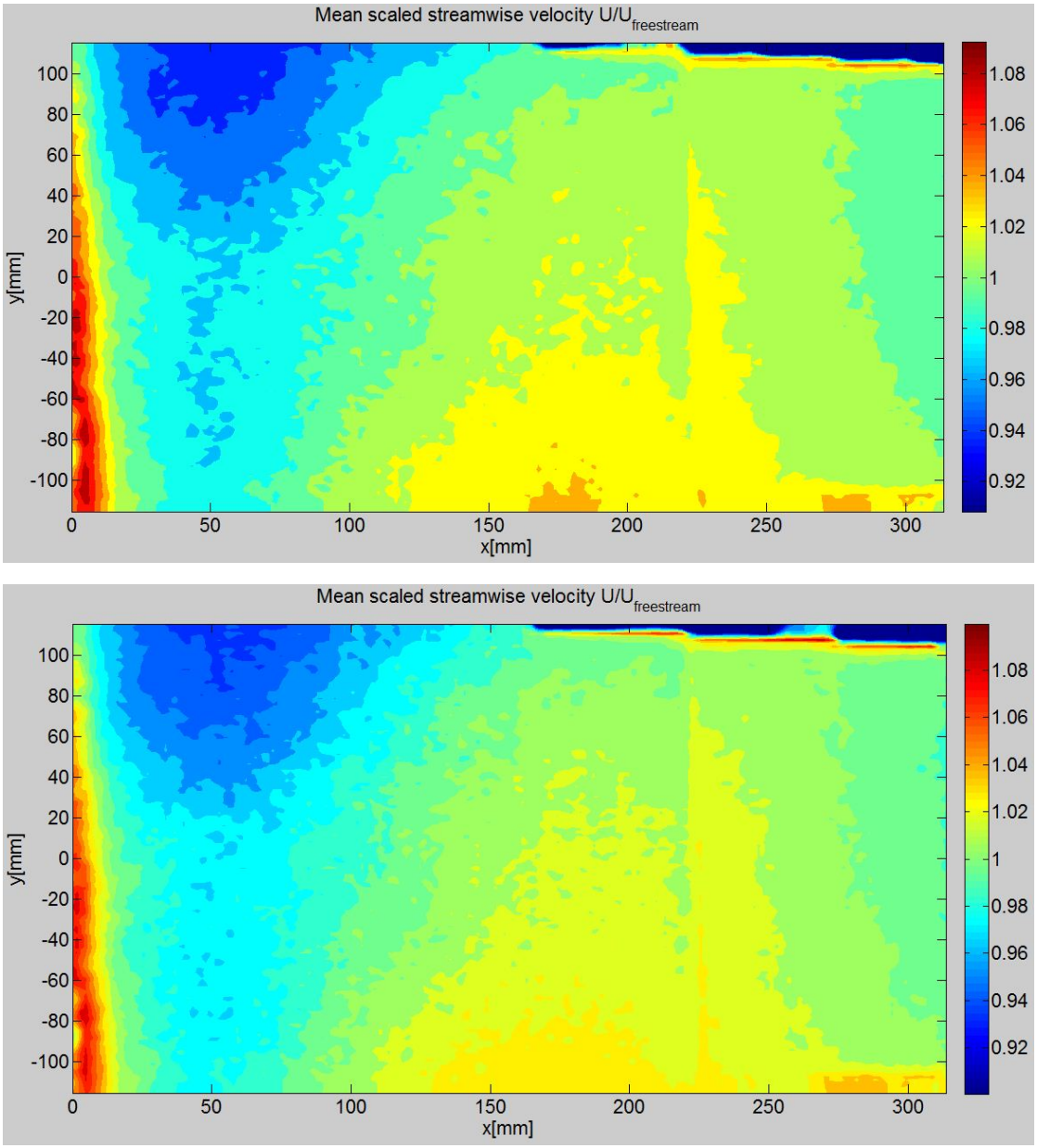


Figure 5.13: Comparison of postprocessing results from Setup 2 without (top image) and with (bottom image) disparity map. Freestream run at $U_{inflow} = 0.035m/s$.

Once more it must be stated that the improvement is minimal. The distortion has changed in its appearance, but it could not be eliminated by changing the camera setup.

### 5.2.4 Result

The present chapter described three methods that can be used to improve results from PIV experiments: the implementation of a disparity map, the use of alternative software and a change in the camera setup. Table 5.1 presents the average values of the streamwise velocity for all applied methods. The deviation from the real streamwise velocity is given in % for all cases.

| Method | $U_{mean}[\frac{m}{s}]$ | Deviation from the real velocity |
|---|---|---|
| VidPIV | 0.0405 | 15.7% |
| VidPIV with disparity map | 0.0405 | 15.7% |
| PivView | 0.0367 | 4.86 |
| PivView with disparity map | 0.0365 | 4.86% |
| Setup 2 | 0.0383 | 9.43 |
| Setup 2 with disparity map | 0.0383 | 9.43% |

Table 5.1: Average values of the streamwise velocity U for the use of different postprocessing methods. All methods were performed with and without the application of an optimizing disparity map. The real free stream velocity of $U_inflow = 0.035m/s$ was measured by the flowmeter of the tank and verified with data given in the water tunnel manual.

It has shown that none of the applied methods led to a major improvement regarding the distortion in the captures of the free stream run. It was therefore chosen to return to the initial postprocessing method in VidPIV and to apply a correction to all mean velocity plots in MATLAB.

# 6 Experiment results

## 6.1 Mean velocity fields

First of all, an overview over the occurrences in the flow past a step cylinder is aimed for. In order to gain first insights, PIV data from the measurements was used to create mean velocity plots. Presented here are plots of the mean velocity in streamwise direction x, as well as the mean standard deviation in z, both averaged over the duration of the presently evaluated experiment. The mean component V is usually close to zero in the entire view field. It is only presented in cases of strong deviations.

Furthermore, the present section investigates the influence of both Reynolds number and diameter step size on the wake flow features by comparing the mean velocity plots for different cylinder models. All discussed plots are found in the appendix in Section 6.1 at the end of the present chapter. All velocity components have been normalized with the respective inflow velocity. For the step cylinder models, the location of the diameter step has been indicated by a horizontal black line. For the plain cylinder, the left edge of the flow field plots coincides with the downstream edge of the cylinder. In the cases of step cylinders, the large diameter section is partly seen, in order to be able to calculate the position of the cylinder axis.

### a) Reference cylinder

A cylinder with a uniform diameter of D=60mm is used as a reference model for the step cylinders (compare Figure 4.1). The comparison with the reference cylinder facilitates the interpretation of the wake flow behind the step cylinders.

Figure 6.2 displays the streamwise velocity component U in the wake of the reference cylinder in experiments 4.051-4.054. The three plots show the flow field at three different Reynolds numbers, increasing from top to bottom. In all three plots, the wake shows an area of negative streamwise velocity close to the cylinder, leading to the conclusion that the presence of the cylinder creates backflow. Further downstream, the flow regains speed. In neither of the cases does the flow return to its initial velocity before leaving the camera view. However, it is observed

that the higher the Reynolds number, the further upstream in the plot take place both backflow and acceleration. The velocity in the plot for the highest Reynolds number is not continuously smooth, but fluctuates irregularly at some locations. It is assumed that turbulence gains an increased influence on the flow at this level. In Figure 6.3, a sectional view along x was taken from the mean plot for each Reynolds number at approximately y/H=0. A comparable plot with a similar development of the mean velocity component U was previously found from spectral element computation at low Reynolds number by Griffin [5]. The graph is presented for comparison in Figure 6.4. The plot in Figure 6.3 confirms the observation in Figure 6.2 with respect to increase in Reynolds number: the maximum of U is located further upstream, the higher the Reynolds number. The green rings highlight backflow regions. Here as well it shows that for the lowest Reynolds number, backflow takes place further downstream.
The observations lead to the conclusion that for high Reynolds numbers, flow characteristics are developed closer to the cylinder than for low Reynolds numbers.

Regular vortex shedding is expected in the wake of the plain cylinder. It is therefore little enlightening to investigate the mean velocity field for the out-of-plane velocity, since it will cancel itself due to the shedding of contrarious vortices. Instead, the root mean square (rms) fluctuation of the out-of-plane velocity component was estimated, also denoted as the standard deviation from its mean value. This method was suggested in previous studies, as statet e.g. by Green and Gerrard [4]. The procedure is used to determine the length of the vortex formation region. The vortex or "eddy formation length $L_f$ [is] defined by the distance downstream from the cylinder axis to the point where the rms velocity fluctuations are maximized on the wake central line" [1]. This has been illustrated by Griffin [5], as shown in Figure 6.5.
In the present case, the standard deviation was estimated at all locations in the view field, averaged over all plots from the experiment and subsequently normalized with the respective inflow velocity. The calculated field of values is presented in Figure 6.6. The eddy formation length was found at approximately $L_f = 3D$.
Figure 6.7 shows cross-sectional profiles of the velocity fluctuation in W. The blue line confirms the results in Figure 6.6: at a Reynolds number of $Re_D = 2243.6$, the

maximum rms is found at x=3.021D downstream from the cylinder axis. With increasing Reynolds number, the maximum of the curve experiences a shift upstream towards the cylinder. This observation is qualitatively supported by Zdravkovich [22]. From the table in Figure 6.1, it is seen that within the studied Reynolds number regime of 1000-2000 to 20000-40000, the eddy formation length $L_f$ is supposed to decrease with increasing Reynolds number.

**Table 1.1** *Epitome of disturbance-free flow regimes*

| STATE | | REGIME | | *Re* RANGES | $L_w/L_f$ | $C_D$ |
|---|---|---|---|---|---|---|
| L | LAMINAR | 1 | NO-SEPARATION | 0 to 4–5 | NONE | ↘ |
| | | 2 | CLOSED WAKE | 4–5 to 30–48 | ↗ | ↘ |
| | | 3 | PERIODIC WAKE | 30–48 to 180–200 | ↘ | ↗ |
| Tr W | TRANSITION IN WAKE | 1 | FAR-WAKE | 180–200 to 220–250 | ↘ | ↗ |
| | | 2 | NEAR-WAKE | 220–250 to 350–400 | ↗ | ↘ |
| Tr SL | TRANSITION IN SHEAR LAYERS | 1 | LOWER | 350–400 to 1k–2k | ↗ | ↘ |
| | | 2 | INTERMEDIATE | 1k–2k to 20k–40k | ↘ | ↗ |
| | | 3 | UPPER | 20k–40k to 100k–200k | SAME | SAME |
| Tr BL | TRANSITION IN BOUNDARY LAYERS | 0 | PRECRITICAL | 100k–200k to 300k–340k | ↗ | ↘ |
| | | 1 | SINGLE BUBBLE | 300k–340k to 380k–400k | (?) | ↓ |
| | | 2 | TWO-BUBBLE | 380k–400k to 500k–1M | (?) | ↓ |
| | | 3 | SUPERCRITICAL | 500k–1M to 3.5M–6M | NONE | ↗ |
| | | 4 | POSTCRITICAL | 3.5M–6M to (?) | (?) | SAME |
| T | FULLY TURBULENT | 1 | INVARIABLE | (?) to ∞ | (?) | SAME |
| | | 2 | ULTIMATE | | (?) | (?) |

$L_w$=length of near-wake (only for L2 regime), $L_f$=length of eddy formation region (from L3 to T2 regimes), Abbr. ↗ increase, ↘ decrease, ↓ rapid decrease, (?) not known.

Figure 6.1: Characterization of flow regimes [22]. In the present study, the eddy formation length was investigated for the highligthed Reynolds number range.

The investigation of the flow field behind the reference cylinder illustrated general flow characteristics. Backflow and subsequent acceleration were observed in all cases. Activity in the out-of-plane direction occurred, which, with the help of rms and reference to previous literature, could be identified as spanwise vortex activity.

At the same time, it was seen that an increase in Reynolds number influenced the flow characteristics in a way of letting them experience a shift upstream towards the cylinder.

**b) Step cylinder**

After having discussed the flow characteristics behind the plain cylinder, results for the step cylinder models from experiments 4.024-4.044 are investigated. By examining the wake of two different step cylinder models (as presented previously in Figure 4.1), the effect of the step size on the wake flow characteristics is estimated. A Reynolds number of $Re_D = 2243.6$ was chosen for the discussion, as an example. The results are compared to the results of the reference cylinder wake.
Figure 6.8 presents mean values for the streamwise velocity field behind all cylinder models. The upper plot, showing the result of the measurement behind the reference cylinder, was discussed in a).
It catches the eye that as the step size increases (middle and lower plot), the influence of the step becomes significant. The backflow region behind the large diameter section expands further in streamwise direction than behind the small diameter section. This happens in the same dimension as suggested by the diameter ratio.

In addition, the mean spanwise velocity component V is displayed in Figure 6.9 for all cylinder models. While the velocity magnitude behind the plain cylinder (upper plot) does not exceed a limit of $\mp 11\%$ of the incoming velocity, the values increase with an increasing diameter step. Furthermore, the values become strongly positive for an increase in step size. While maximum values for V do not exceed $0.12U_{inflow}$ for cylinder D/d=6/5, positive, as well as negative velocity values reach up to 25% behind cylinder D/d=2. Accurate values are presented in Table 6.1, in comparison with V at other Reynolds numbers. In the plot for Cylinder D/d=2, negative velocity is found underneath the step and just behind the cylinder. Further downstream the flow is characterized by an upwards trend of the flow towards the region in the wake of the large diameter section. This has been stated to be a consequence of a loss in base pressure, so-called downwash [8].

Since the velocity fluctuation in W provides important information about the location of vortex formation, the mean rms of the fluctuation in W is presented in Figure 6.10. The step size of the cylinder increases from top to bottom plot.

It shows that the diameter step leads to unlike developments in the small and the large diameter wake. The eddy formation region behind the large diameter section $L_{f,L}$ is longer than the eddy formation region in the small diameter wake, $L_{f,S}$. This is pronounced stronger for the large step.

In order to be able to discuss the effect of an increasing Reynolds number on the streamwise velocity behind a step cylinder, Figure 6.11 presents U for the cylinder D/d=2 at three different Reynolds numbers. The Reynolds number increases from top to bottom plot. According to the discussion concerning the reference cylinder in a), it is expected that an increasing Reynolds number will lead the development of flow characteristics to take place further upstream. This expectation is satisfied. While the earliest acceleration to positive velocity in the small diameter wake takes place at approximately x=2D, the velocity turns positive already at approximately x=0.5D for the higher Reynolds number. In the middle and bottom plot, a stronger acceleration is observed in the large than in the small diameter wake. A transformation from the middle to the bottom plot is observed in the disappearence of the backflow region in the large diameter wake. At the lowest Reynolds number, a small arm of positive velocity connects the region of accelerating flow with the step. This leads to the insight that at this Reynolds number, the step inhibits backflow.

In Figure 6.12, the vertical velocity component V behind the step cylinder D/d=6/3 is discussed with respect to the Reynolds number influence. The upper plot is known from the previous discussion in Figure 6.9. A strongly negative component was observed just behind the cylinder, followed by an area of strong upwards flow (downwash) further downstream.
As the Reynolds number increases, in Figure 6.12 from top to bottom, the area of downwards flow disappears, while the strong upwards flow region is mostly limited to the wake of the large diameter section. The magnitude of the upwards trend behind the small diameter section is less articulated than at the lower Reynolds number. These findings are documented in concrete values in Table 6.1.

The recent observations show that the presence of the cylinder has a stronger

influence on the wake for low than for high Reynolds numbers with respect to vertical flow exchange. In Table 6.1, the flow at $Re_D = 2243.6$ shows to return the strongest magnitudes in y. For the cylinder with the largest diameter step, positive values show a much stronger deviation from zero than negative values.

| Cylinder model | $Re_D$ | $\frac{V_{min}}{U_{inflow}}[\%]$ | $\frac{V_{max}}{U_{inflow}}[\%]$ |
|---|---|---|---|
| D60 | 2243.6 | -10.5 | 8.6 |
| D/d=6/5 | 2243.6 | -7.7 | 11.9 |
| D/d=6/3 | 2243.6 | -22.5 | 25.27 |
| D/d=6/3 | 12820.5 | -2.62 | 24.0 |
| D/d=6/3 | 51282.1 | -2.95 | 29.8 |

Table 6.1: Percentage of the streamwise flow component V with respect to the inflow velocity. Minimum and maximum values are compared for all examined cylinder models at $Re_D = 2243.6$.

Finally, the out-of-plane velocity component W is of central interest. From the upper plot in Figure 6.13, it is seen that the eddy formation length $L_f$ differs along the cylinder span for the step cylinder. The x-values corresponding to the fluctuation maxima in Figure 6.14 define $L_f$ behind the small diameter section, the large diameter section and the step.
In addition, Figure 6.13 presents the change in in the eddy formation region with increasing Reynolds number. From the top to the middle plot, it is observed that the increase in Reynolds number leads to a shorter $L_f$. At the same time, the distance between $L_{f,L}$ and $L_{f,S}$ becomes larger. The bottom plot with the highest Reynolds number shows significant noise in the signal. The eddy formation region is identifyable, but fluctuation in the out-of-plane velocity component is present in the entire view field. This is interpreted as an effect of increasingly turbulent flow.

The present section has shown that the introduction of a step to the cylinder model strongly affects the wake flow behavior. It was observed that characteristics like flow acceleration in flow direction and maximum velocity fluctuation take

place further downstream behind the large diameter section than behind the small diameter section. At the same time, the step leads to the development of a strong upwards component, leading the flow into the wake of the large diameter section. This result is explained by the phenomenon of downwash.

In addition, the influence of the Reynolds number on the wake characteristics of a step cylinder with a diameter ratio of D/d=2 was discussed. At an increased Reynolds number $Re_D$, the region of upwards flow experiences a shift towards the cylinder. Generally, the observed flow characteristics are less pronounced at higher velocities. At the highest investigated Reynolds number, turbulence obtains increasing influence.

After having investigated the mean characteristics and knowing trends of the flow, it is now important to specifically look into the development of the flow characteristics with time.

### c) Appendix: mean velocity plots

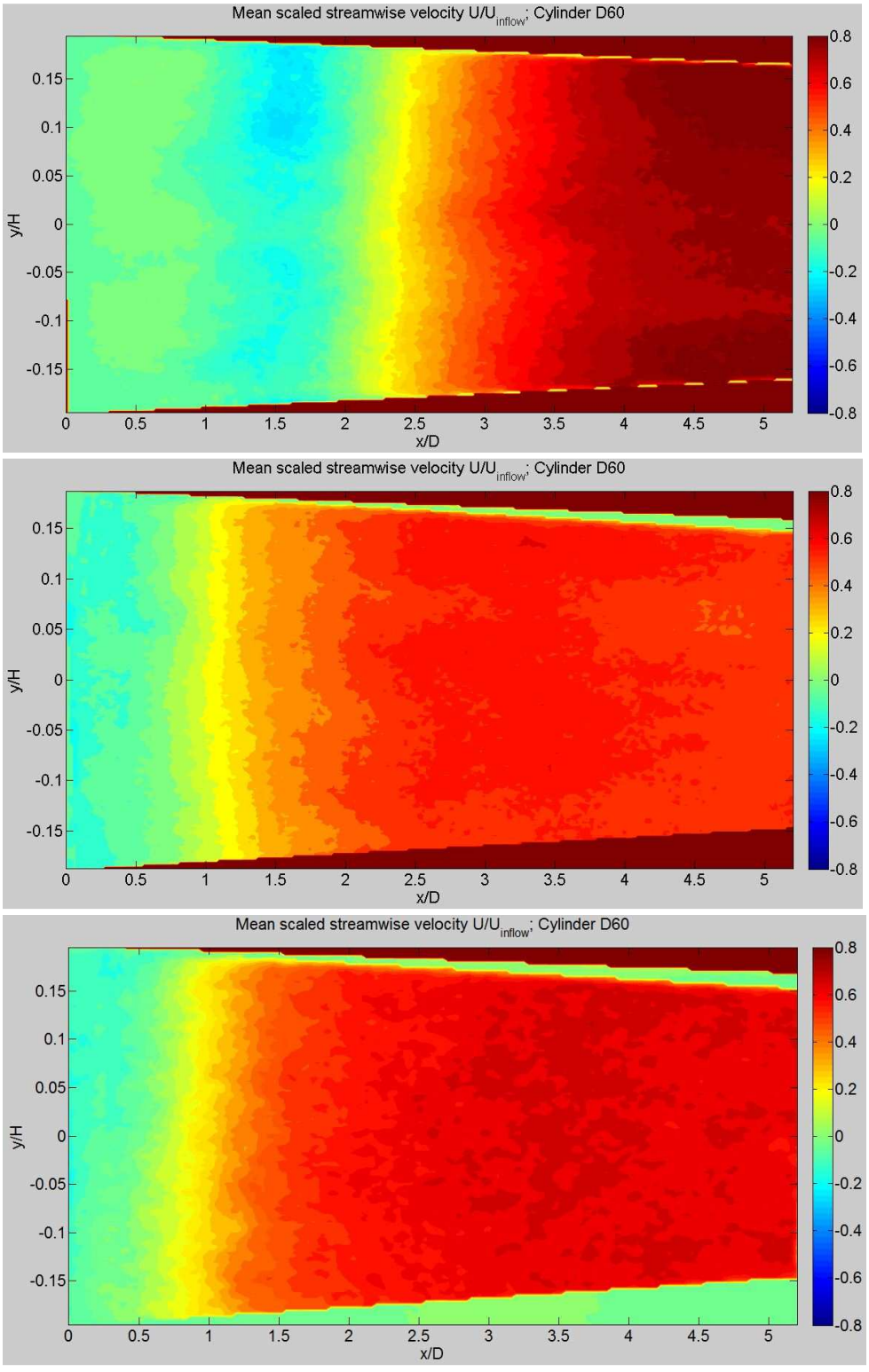


Figure 6.2: Streamwise velocity component U, estimated from experiments 4.054, 4.052 and 4.051. From top to bottom: Re(D)=2243.6; 12820.5; 51282.1. The velocity has been scaled with the inflow velocity. Note different scales for different plots.

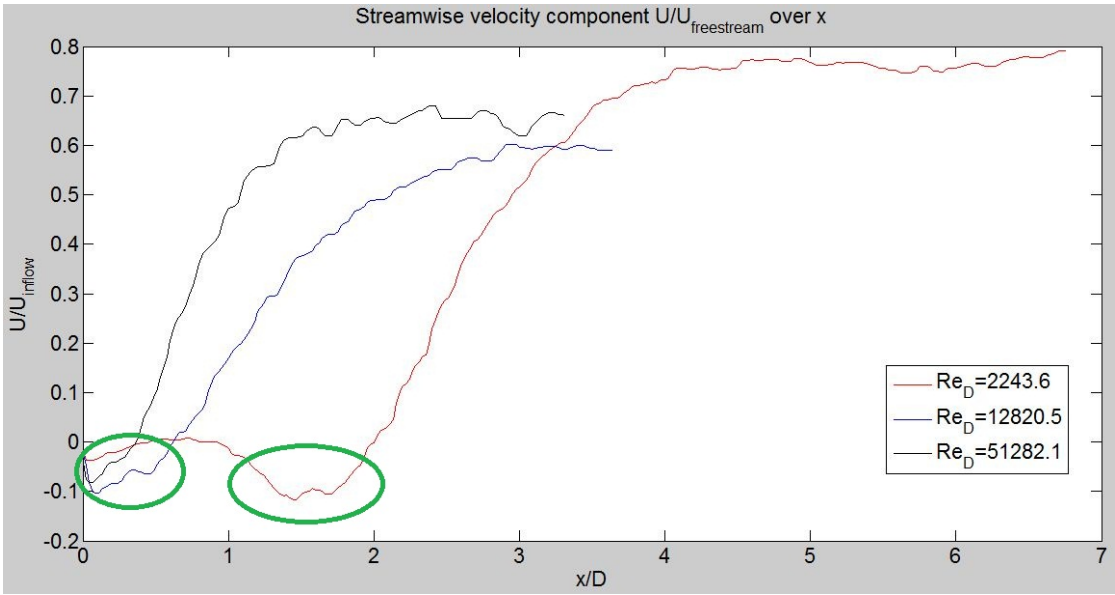


Figure 6.3: Sectional view of the mean plots for U, compared for three Reynolds numbers. Backflow areas are marked in green.

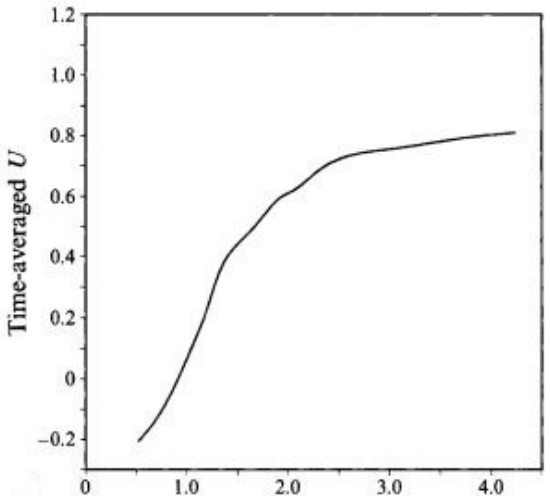


Figure 6.4: Development of the streamwise velocity component with x/D. Found by Griffin [5] from spectral element computation at $Re_D = 200$. The graph corresponds to the observations seen in the previous figure: strong inclination up to x=1.5D and continuous leveling until an almost constant level is reached at about x=4D.


Figure 6.5: Definition of the eddy formation length $L_f$, as observed from flow visualization in the wind tunnel by Griffin [5].

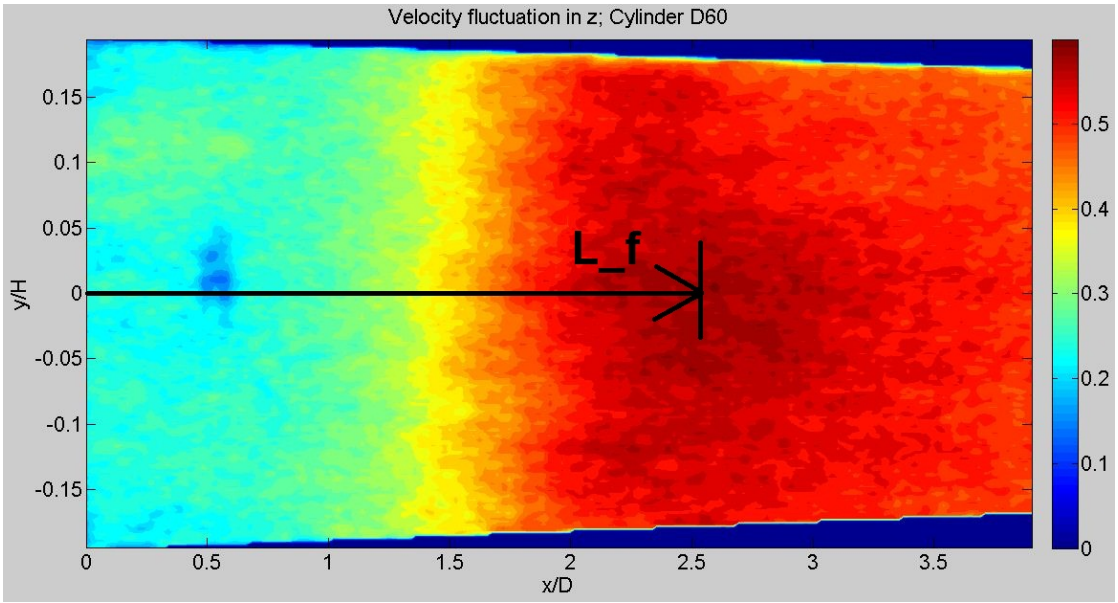


Figure 6.6: Fluctuation of the out-of-plane velocity component in the wake of cylinder D60 at $Re_D = 2243.6$. The fluctuation from the mean value is represented by the standard deviation, normalized with $U_{inflow}$. The eddy formation length is found at the location of strongest activity. Note: the left edge of the plot coincides with the downstream edge of the cylinder. In order to obtain the entire eddy formation length, 0.5D must be added to the visible length.

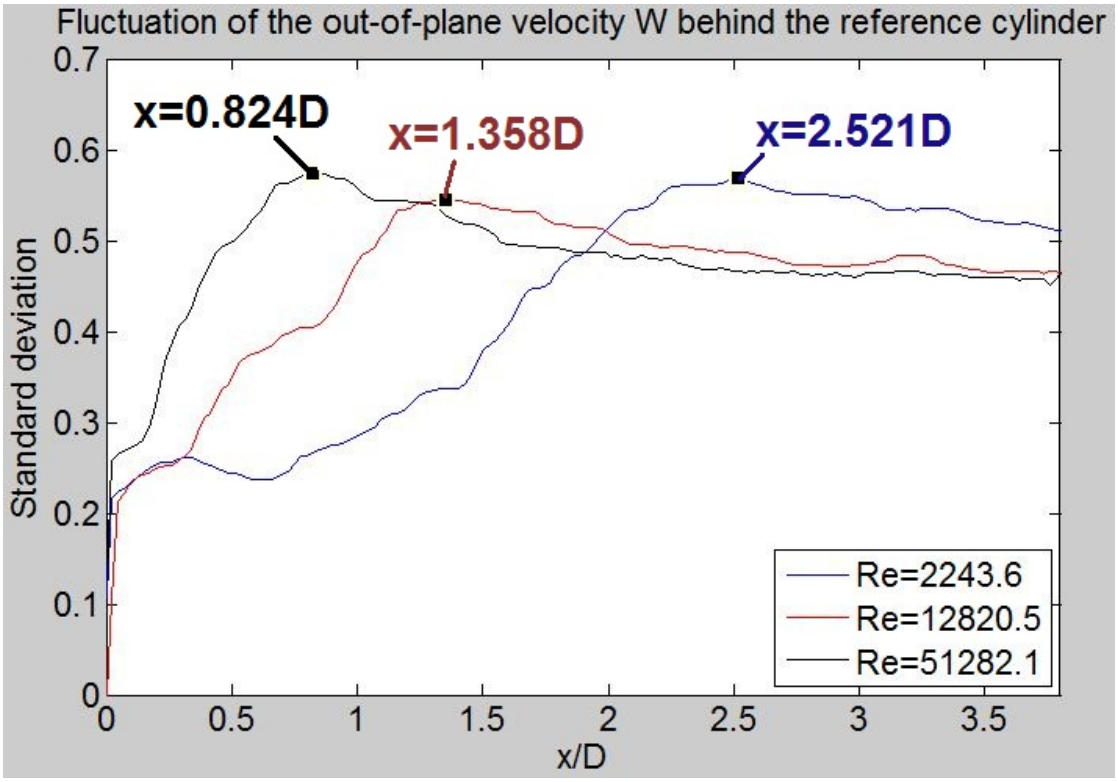


Figure 6.7: Profiles of the velocity fluctuation at three different Reynolds numbers, represented by the rms, at y=0 (middle of cylinder span). The rms has been normalized with the inflow velocity.

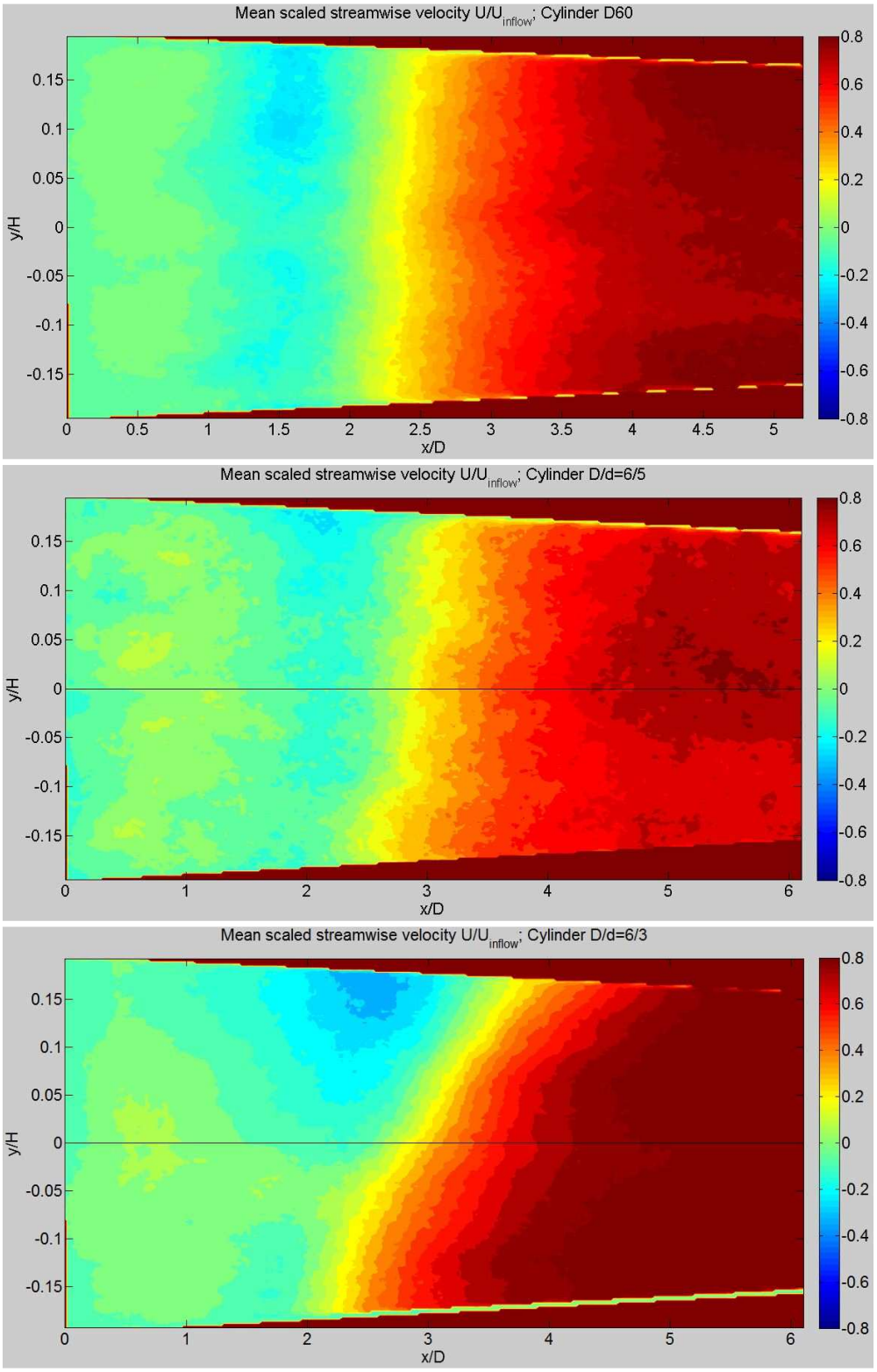


Figure 6.8: Mean velocity plots of the streamwise velocity (scaled with the inflow velocity). Results from experiments 4.054, 4.024 and 4.044. From top to bottom with increasing diameter step size. The location of the step in y is represented by a horizontal black line.

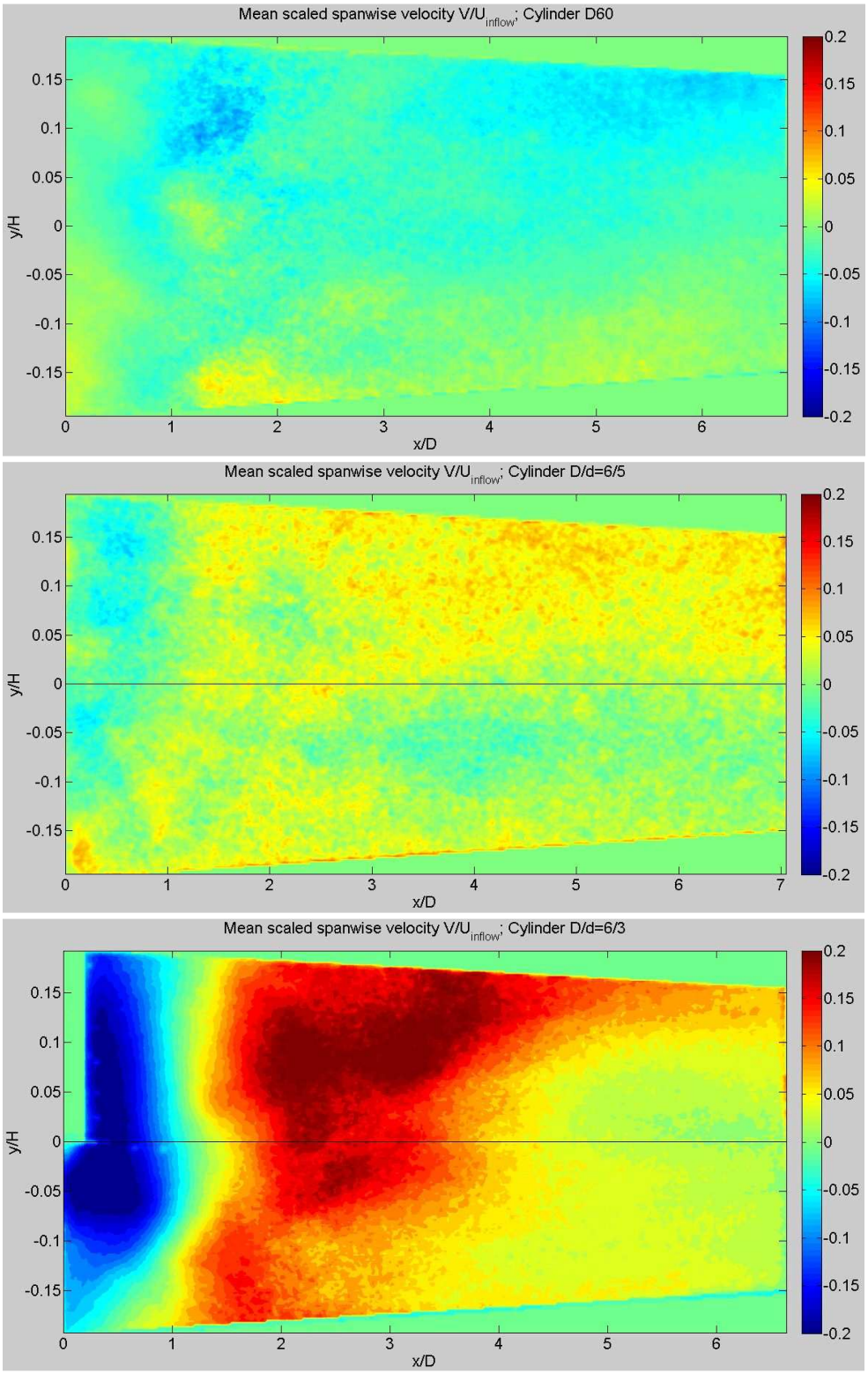


Figure 6.9: Mean plots of the spanwise velocity (scaled with the inflow velocity). From top to bottom with increasing diameter step size. In the bottom plot, the large diameter section is seen on the left edge, represented by a region of zero velocity.

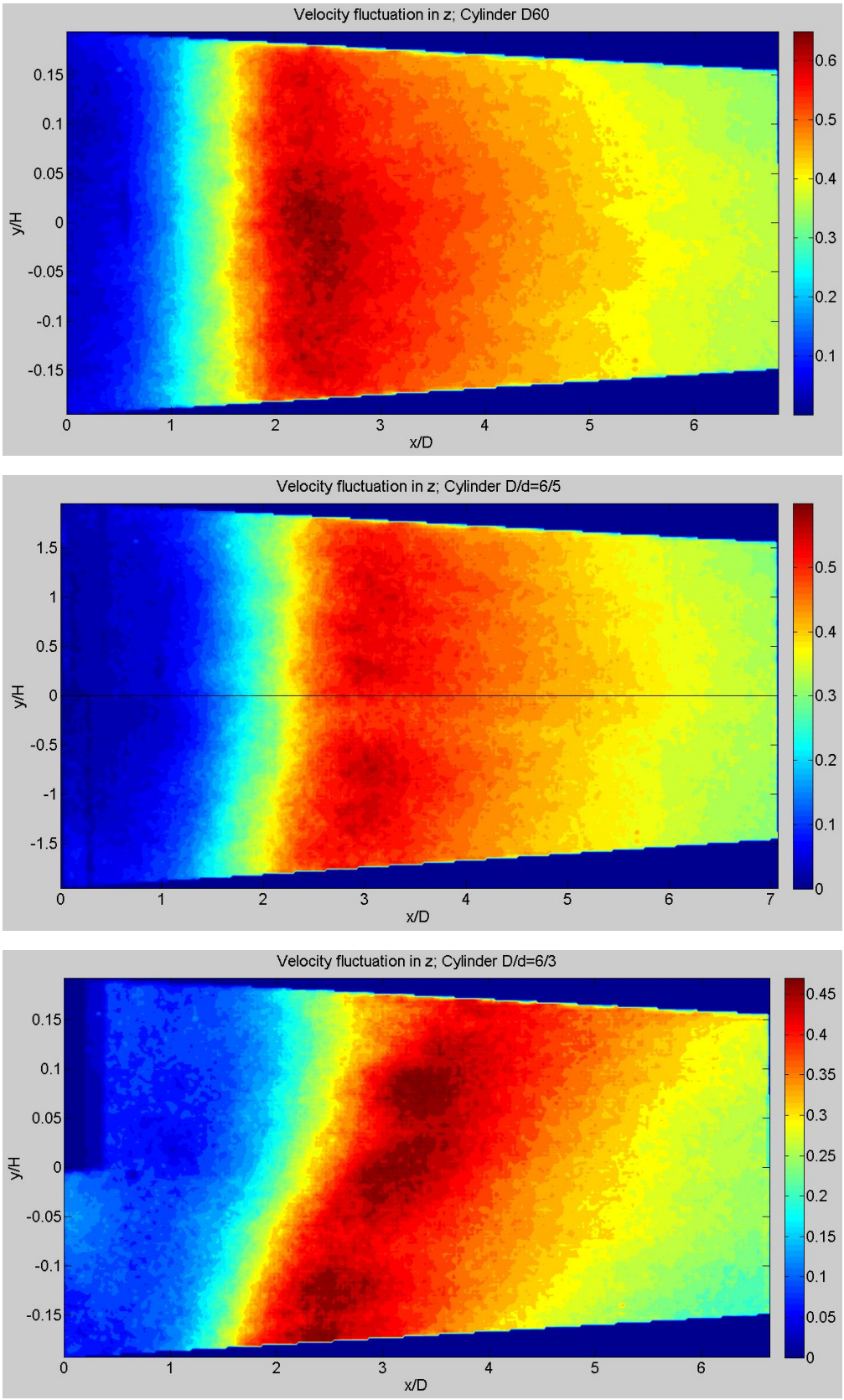


Figure 6.10: rms of the fluctuation in z, averaged over the duration of the corresponding experiment. Note that the color map was chosen differently for the respective plots.

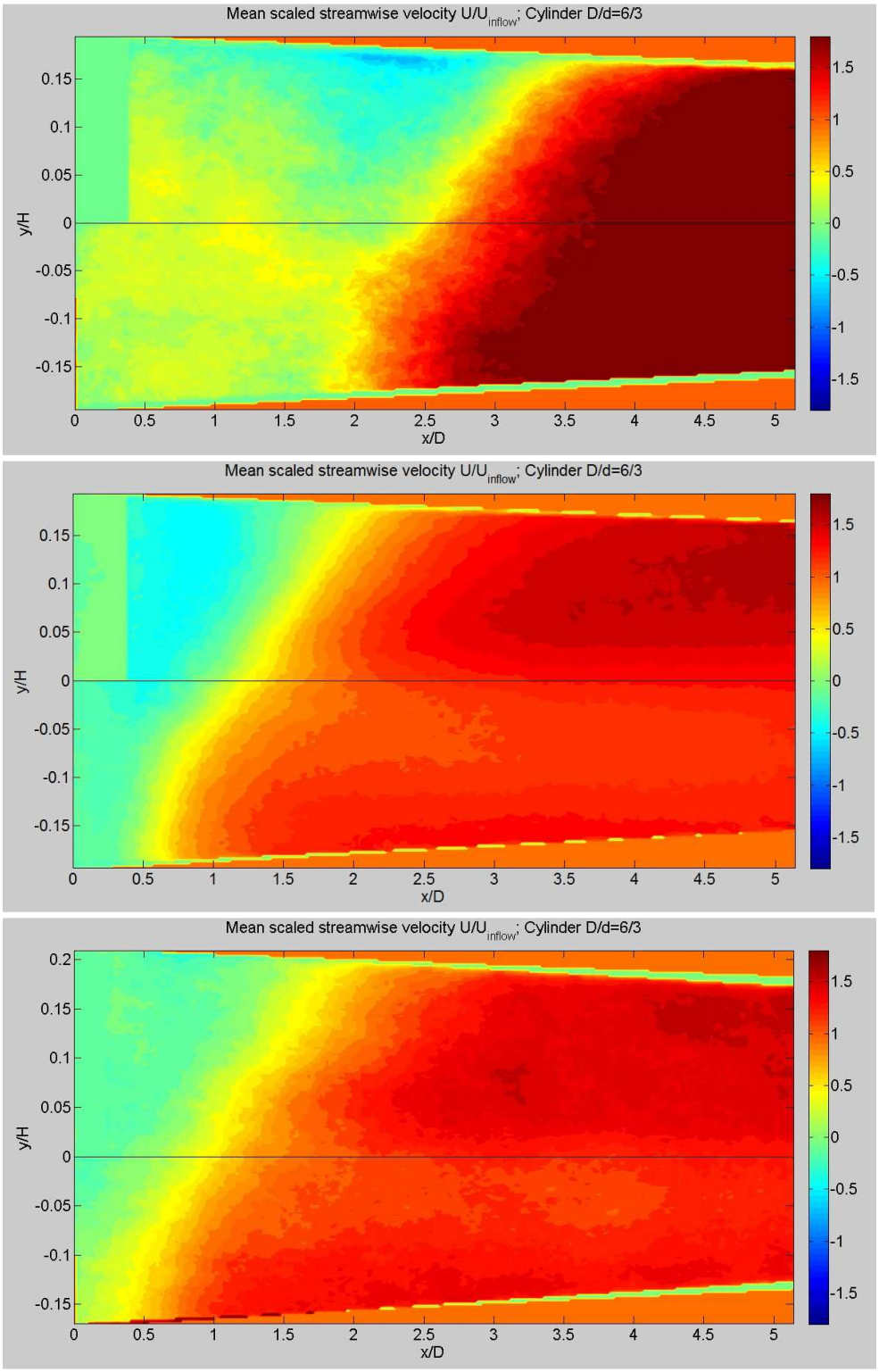


Figure 6.11: Mean velocity plots of the streamwise velocity, scaled with the inflow velocity. From top to bottom with increasing Reynolds number. Experiments 4.041, 4.042, 4.044.

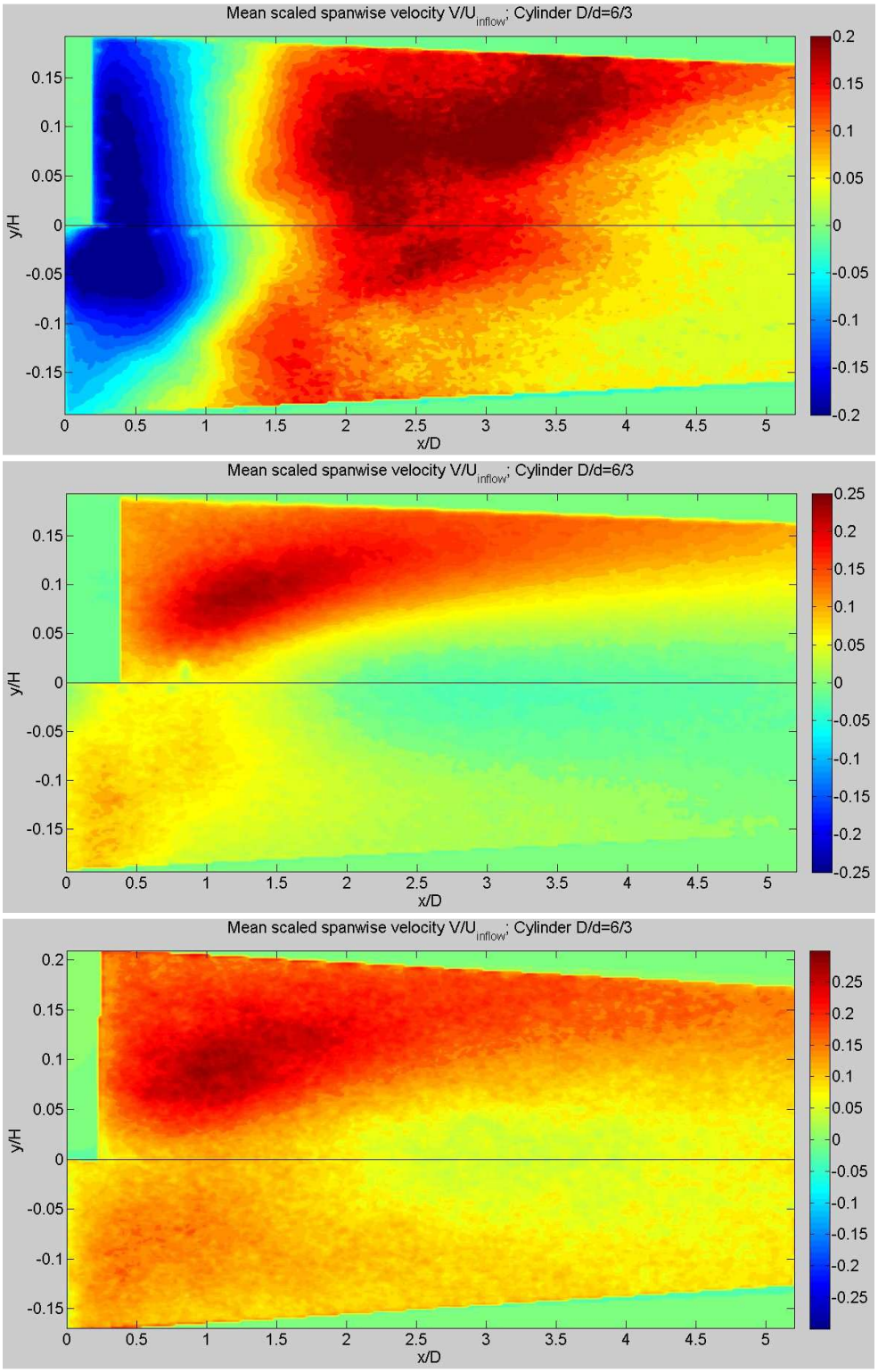


Figure 6.12: Mean velocity plots of the spanwise velocity behind the cylinder D/d=6/3, scaled with the inflow velocity. From top to bottom with Reynolds numbers $Re_D = 2243.5; 12820.5; 51282.1$. Note the change in scale for the respective plots.

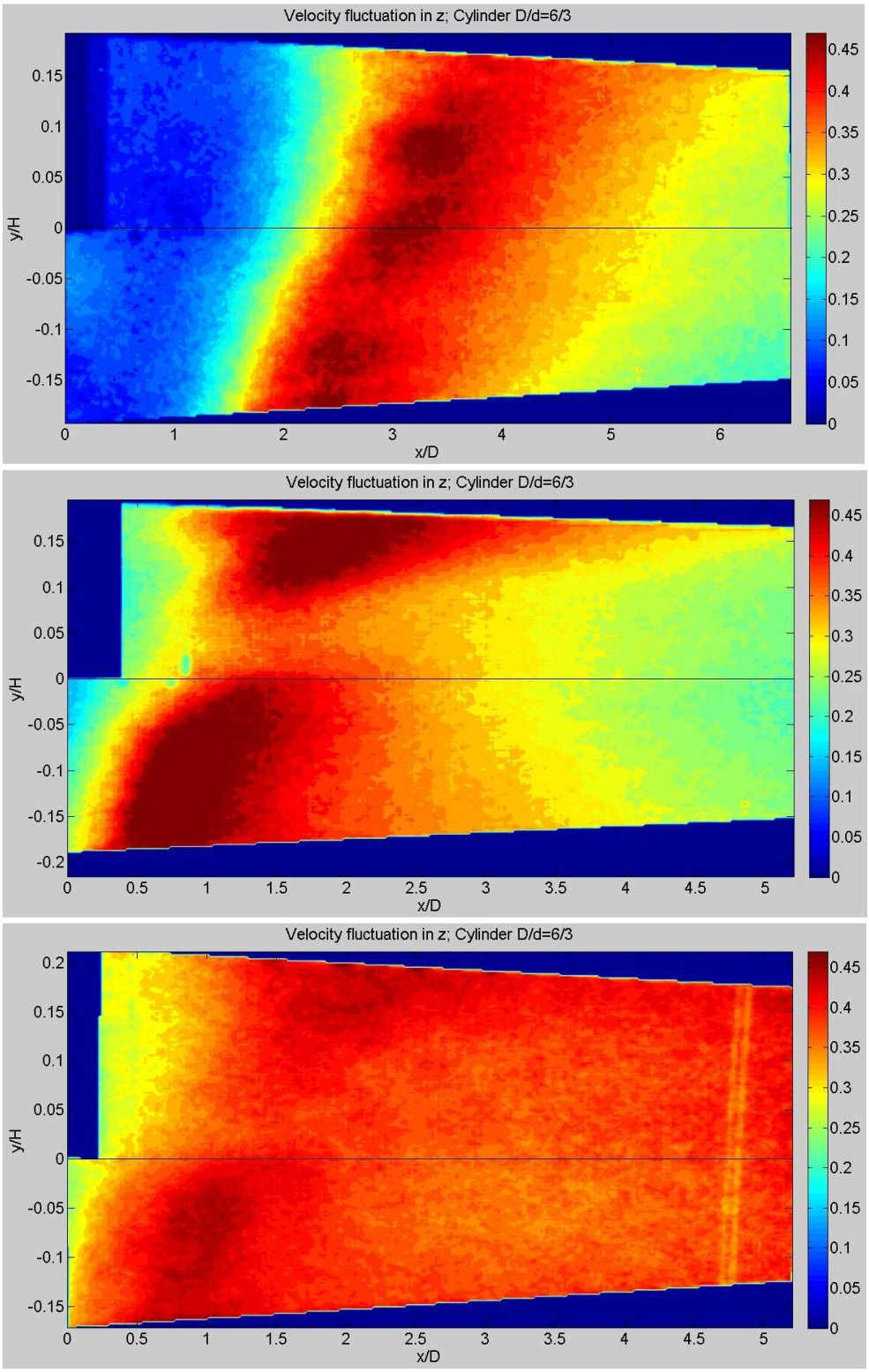


Figure 6.13: Fluctuation of the out-of-plane velocity component in the wake of cylinder D/d=6/3 at $Re_D = 2243.6, 12820.5, 51282.1$.

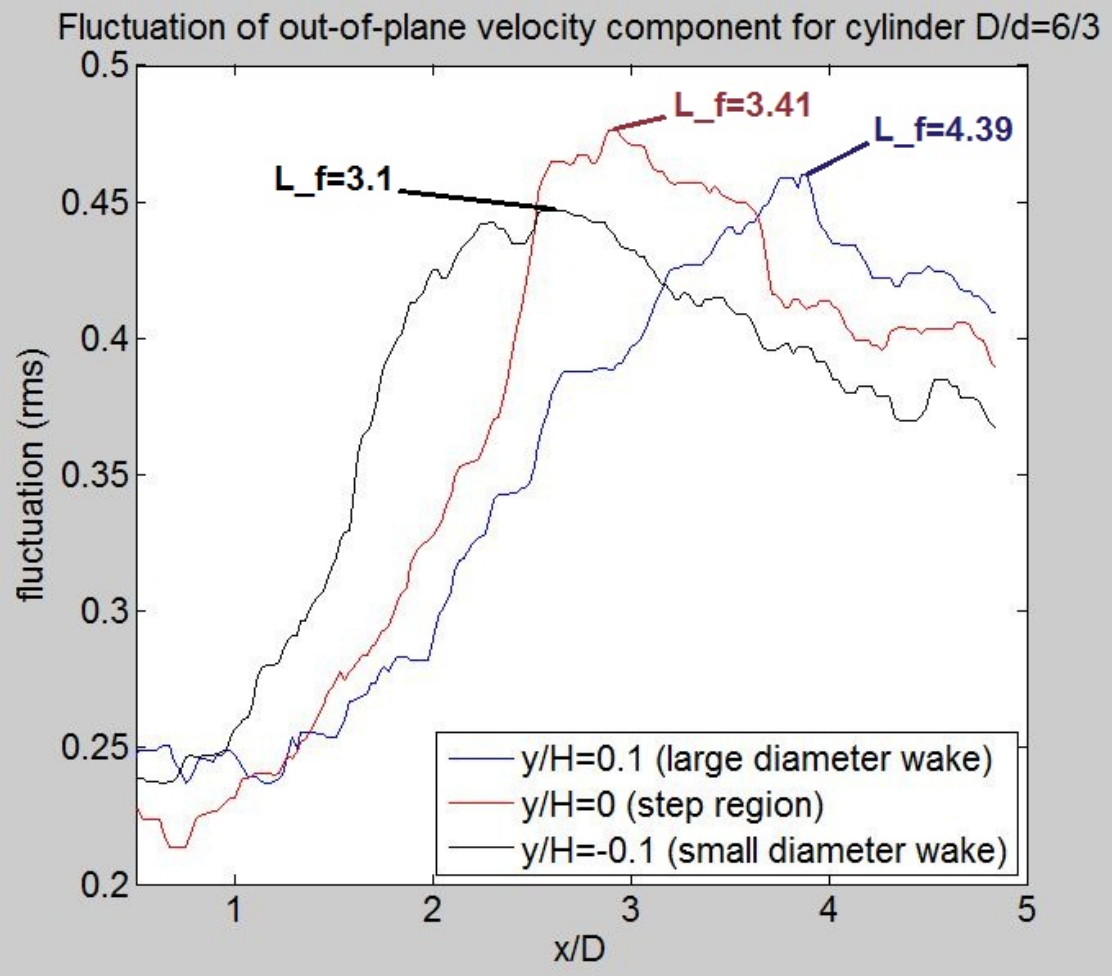


Figure 6.14: Fluctuation of the out-of-plane velocity component W behind small diameter section, large diameter section and step, respectively. The fluctuation is expressed by the rms of the velocity signal. The eddy formation region $L_f$ is defined by the location in x with the strongest fluctuation. $Re_D = 2243.6$.

## 6.2 Flow development over time

Dunn and Tavoularis [3] developed a schematic sketch of the vortex occurence around and behind step cylinders. The sketch is presented in Figure 6.15. The present chapter investigates the vortex development behind step cylinders by analyzing instantaneous velocity data. The sketch by Dunn and Tavoularis [3] is here used as a starting basis and will help understand the occurances in the wake. In addition to the principles presented in the sketch, the present section deals with interactions between vortices in small and large diameter wake.

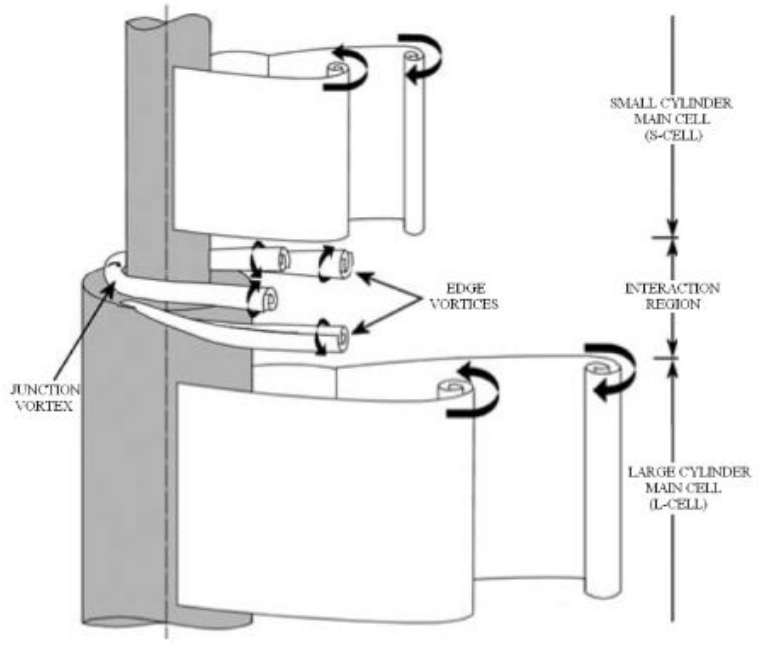


Figure 6.15: Schematic drawing of vortex occurances behind and around step cylinders [3].

At first, instantaneous velocity components of the wake flow behind the reference cylinder are investigated in detail, starting from a random instant during the measurement. Figure 6.16 presents the velocity component U in three successive time instants, each with a time distance of $\Delta t = 1s$. The data was collected in experiment 4.054.

All three plots support the observations from the mean velocity plot, previously presented in Figure 6.2, upper plot. Just behind the cylinder, the flow slows down. In the mean plot, backflow towards the cylinder was discovered, beginning at about

x=D, up to approximately x=2D. Backflow is also observed in the instantaneous plots. The magnitude of the backflow is seen to be higher than estimated from the mean plots, while its expansion varies with time. Starting at about x=2D and further downstream, the flow is re-accelerated. The instantaneous plots show an interesting feature that was impossible to see in the mean plot: the flow acceleration is not a continuous process. In a spacial distance of 3 diameters respectively, here marked by vertical green lines in the lower half of the plots, the streamwise flow is pulled back towards the cylinder. This development is expected to be a consequence of spanwise vortex shedding in the cylinder wake. Next, the plots are compared to plots for the out-of-plane component, in order to verify this hypothesis. [1]

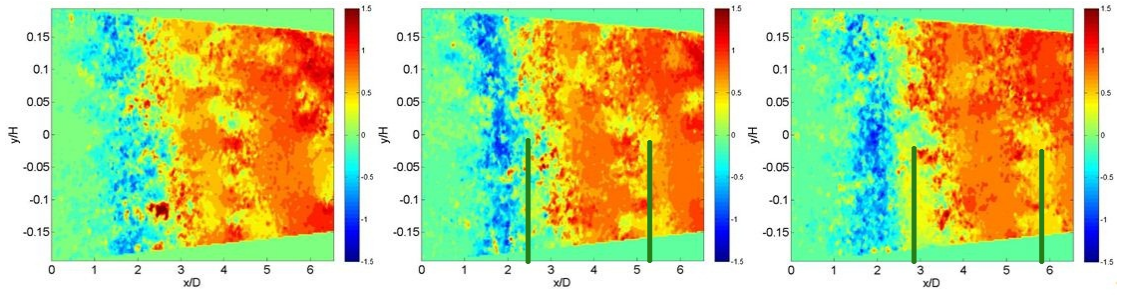


Figure 6.16: Instantaneous plots of the streamwise velocity U, starting at a random instant in time, with a time distance of $\Delta t = 1s$. $Re_D = 2243.5$. Green lines mark areas where the streamwise velocity is slowed down.

Figure 6.17 displays the instantaneous development of the out-of-plane velocity component W. In all plots, regions of positive velocity are followed by regions of negative velocity. This observation corresponds to the theory of vortex shedding in the wake of circular cylinders [22]. In the present case, it is assumed that one positive and one negative region together represent a vortex, with the vortex center located between the two regions, as it is indicated in the first plot in Figure 6.17. According to this interpretation, the vortices then have a spatial distance of approximately 3 large cylinder diameters, which corresponds to the observation

[1] In this section, little attention was payed to the readability of axis and colormap labels. In this connection it is however mostly of interest to observe trends in the flow, rather than specific magnitudes. Colorbars for velocity sequences of the same kind (e.g. streamwise velocity) are labeled with the same colormap. All colormaps are symmetrical to zero. Velocity magnitudes can be estimated from the previously discussed mean velocity plots.

in Figure 6.16. The vortex cores marked VC1 and VC2 can be followed through the sequence. According to Figure 6.6, vortices are not fully developed before the end of the eddy formation region, which was in this case found to be $L_f = 3D$, corresponding to x/d=2.5 from the downstream edge of the cylinder in the present plot.

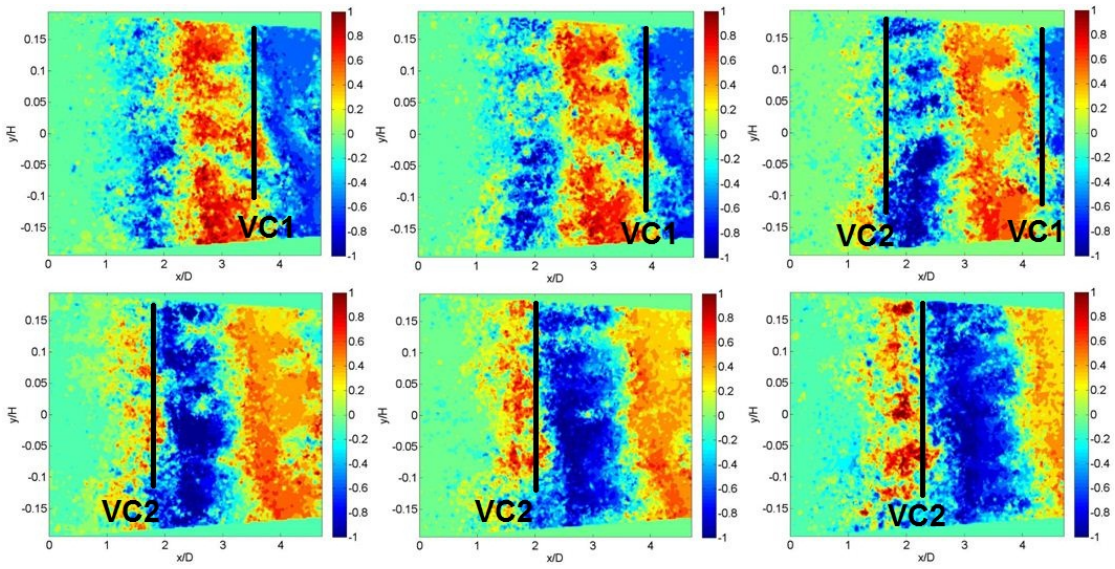


Figure 6.17: Sequence of instantaneous plots of the out-of-plane velocity W, starting at a random instant in time, with a time distance of $\Delta t = 1s$. Two probable vortex cores are marked VC1 and VC2 in all plots.

With the knowledge about the flow development behind the reference cylinder, the development of the wake behind step cylinders is now investigated. In Figure 6.18, the streamwise velocity component in the wake of step cylinder D/d=6/5 is presented (experiment 4.024). From the mean velocity plot in Figure 6.8, flow acceleration in streamwise direction behind the large diameter section is expected to happen further downstream than for the reference cylinder. The acceleration in the wake of the small diameter section however should start approximately at the same position as for the plain cylinder.

These expectations are fulfilled by the instantaneous plots. The observation is interesting, since the small diameter section is thinner than the reference cylinder, while the large diameter section has the same diameter as the reference cylinder. In contrast to the flow development behind the plain cylinder, it is difficult to draw conclusions on exact positions of spanwise vortices from the instantaneous

streamwise velocity plots for cylinder D/d=6/5.

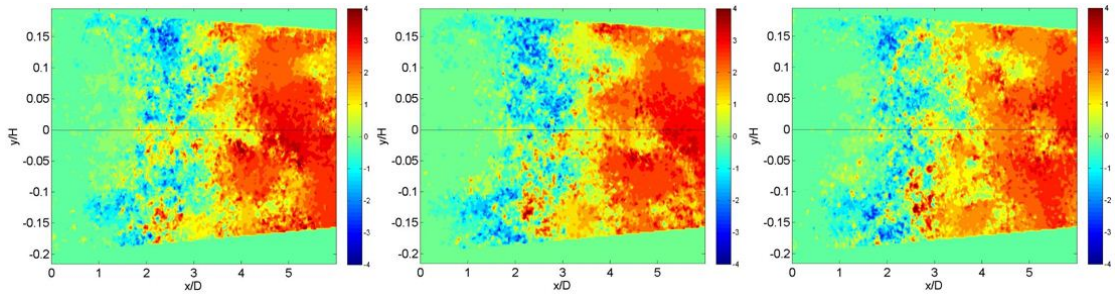


Figure 6.18: Instantaneous plots of the streamwise velocity U in the wake of cylinder D/d=6/5, starting at a random instant in time, with a time distance of $\Delta t = 1s$. $Re_D = 2243.6$.

Figure 6.19 shows a sequence of instantaneous out-of-plane velocity plots in the wake of cylinder D/d=6/5. As for the previous case, a vortex core is indicated and followed through the series. Here, the behavior of vortex cores differs for the regions behind the small and the large diameter sections. Behind the large diameter section, the regions lean back towards the cylinder. When analyzing plots over the entire duration of the experiment, it becomes clear that this inclination angle alternates with time. At its highest value, the inclination towards the cylinder amounts to 57°. Later in the sequence, the small diameter wake inclines towards the cylinder as well.

The present series of plots shows an additional interesting feature, compared to the sequence for the plain cylinder: red circles indicate locations where vortices connect to subsequent vortices. This happens for the first time in the last plot in the second row. Here, a connection builds up from the positive velocity region that is a part of the vortex with core VC1, to the subsequent region with positive out-of-plane velocity. This connection takes place in the wake of the small diameter section. Two plots further in the sequence however, a similar connection is observed in the wake of the large diameter section. The connection remains visible in the following two plots. The following plot shows residuals of both observed connections. Backwards connections are also discovered in the last three plots. One of those builds up behind the step, the other one in the wake of the large diameter section.

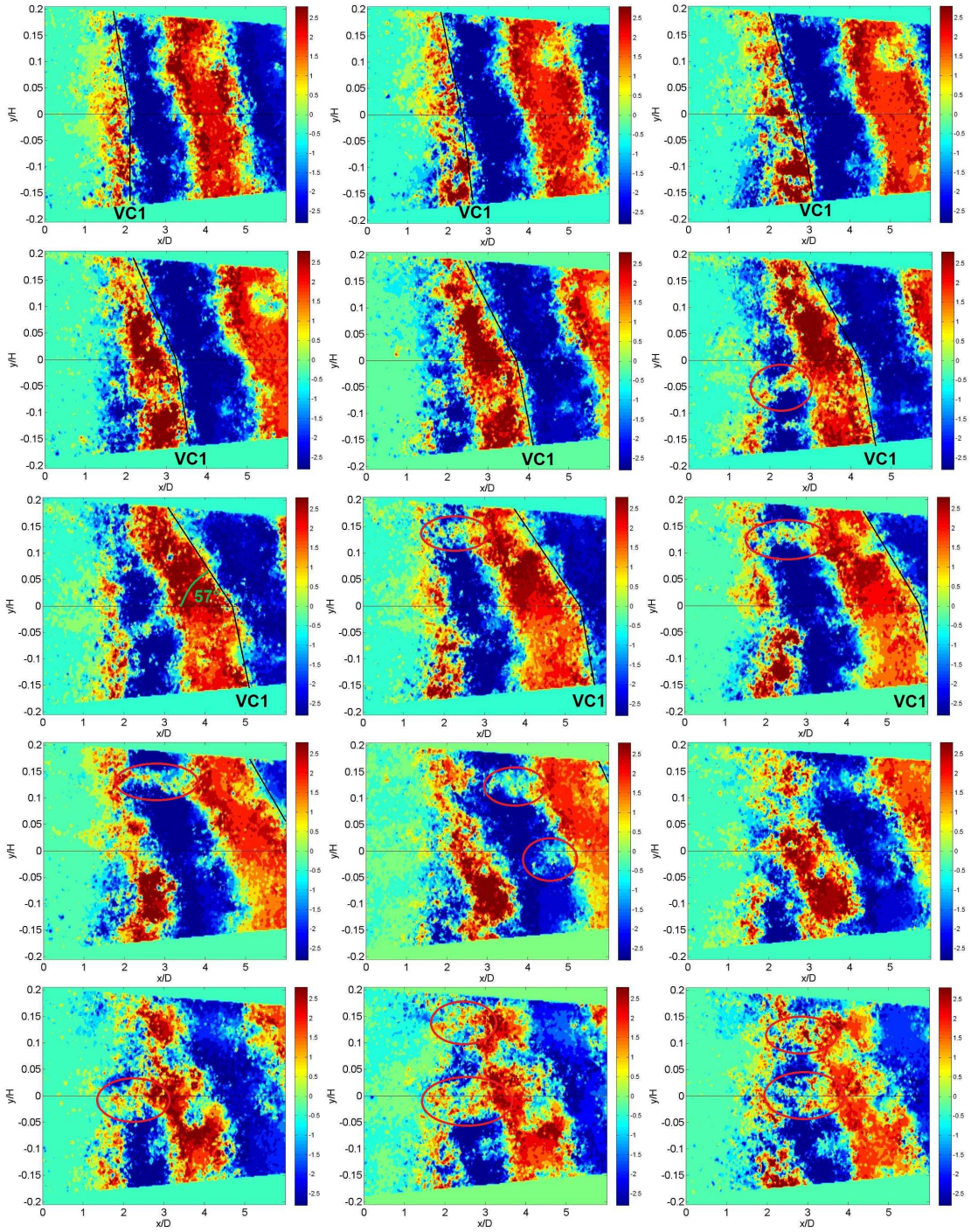


Figure 6.19: Instantaneous plots of the streamwise velocity W in the wake of the cylinder D/d=6/5, starting at a random instant in time, with a time distance of $\Delta t = 1s$. $Re_D = 2243.6$.

In Figure 6.20, the development of the streamwise velocity component is presented for the cylinder D/d=2 (experiment 4.041). Here as well, the interpretations of the corresponding mean velocity plot in Figure 6.8 are confirmed: the area with zero velocity just behind the cylinder is followed further downstream by a backflow region, starting at about x=1.5D. In the wake of the small diameter section, the backflow area lasts until approximately x=2D, while behind the large diameter section it expands downstream to approximately x=3D.
The following area of flow acceleration in the instantaneous captures is not smooth, but characterized by chaotic features with no clear hint to regular vortex shedding.

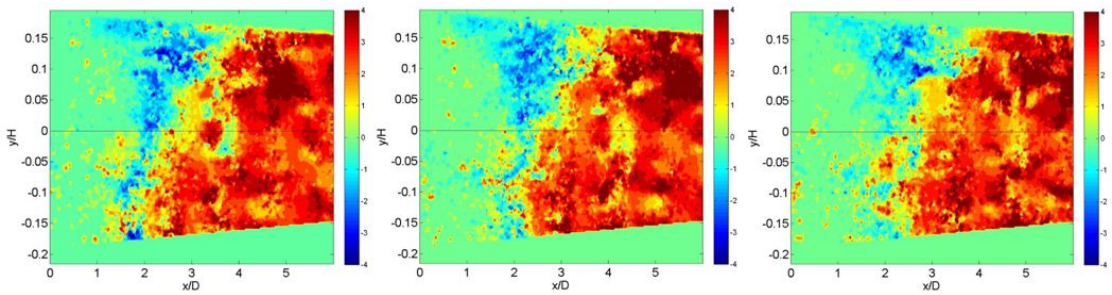


Figure 6.20: Instantaneous plots of the streamwise velocity U in the wake of the cylinder D/d=6/3, starting at a random instant in time, with a time distance of $\Delta t = 1s$. $Re_D = 2243.6$.

Figure 6.21 shows the corresponding out-of-plane velocity W. As in previous sequences, a possible vortex core VC1 is followed from its creation through the series. In the present case however, velocity regions below and above the step do not necessarily connect to each other across the step region. Initially, the vortex with core VC1 is only identifyable in the wake of the small diameter wake, however it is expanding vertically over the step with time. In the last plot in the second row, a backwards connection starts establishing from the negative velocity region of vortex VC1 to the subsequent negative velocity region. This connection strengthens in the course of the third row. The subsequent negative velocity region expands along the entire cylinder span, regardless the step. In the last plot of the third row, a second vortex core VC2 can therefore be marked along the whole cylinder span. In this plot, the positive velocity region of VC1 starts to build up a connection to its aforegoing positive velocity region. At the same time, the connection of the negative velocity regions of VC1 and VC2 dissolves. In the fourth

row of plots, an almost regular vortex movement is observed, until in the last row both regions of VC2 start connecting to their subsequent vortex.
The first plot in the series shows five pronounced velocity regions in the small diameter wake, while only four are observed in the wake of the large diameter section. This is a sign for the vortex shedding frequency being higher in the small than in the large diameter wake.

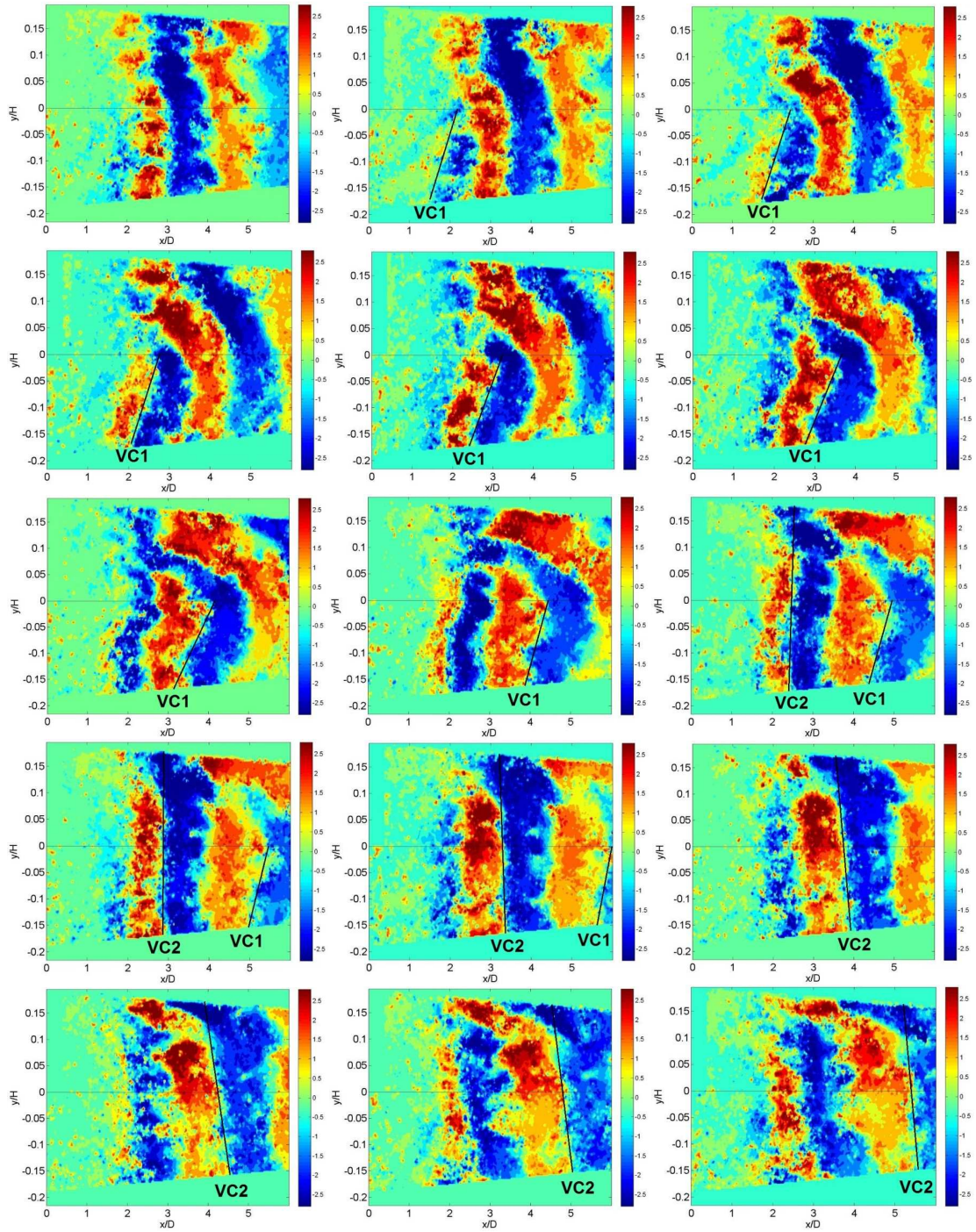


Figure 6.21: Instantaneous plots of the out-of-plane velocity W in the wake of cylinder D/d=2, starting at a random instant in time, with a time distance of $\Delta t = 1s$. $Re = 2243.6$.

Until here, the investigation of the instantaneous velocity has shown that a step in diameter is reponsible for an increasing mismatch in vortex shedding frequency behind small and large diameter section, respectively. Therefore it is not always possible for vortices in the two wakes to connect across the step region. Backwards connections to subsequent vortices on the same side of the step region are the result. Furthermore, an increase in step size leads to an increased amount of pronounced backwards connections. For the highest investigated diameter ratio, backwards connections were observed only in the large diameter wake.
The phenomenon of backwards connections in the step region was first observed by Lewis and Gharib: "The vortex lines are interrupted along a plane, which we call the interface. [...] Vortices connect across the interface when they are in phase (or nearly so). As they become more out of phase, the vortices form linkages to one another on the same side of the interface." ([9], p. 106).

After having seen the effect of an increasing diameter ratio on the vortex shedding pattern, it is now of interest to have a look at the effect of an increasing Reynolds number. For this purpose, two time series of velocity plots were created from the results of experiment 4.041 with a Reynolds number of $Re_D = 51282.1$. The first resulting sequence, presented in Figure 6.22, shows the streamwise velocity component U in the wake of the step cylinder D/d=2. The trends of backflow and subsequent flow acceleration are present as in all previously shown mean and instantaneous plots. The peculiar characteristic of the present plots is that the streamwise velocity is clearly influenced by spanwise vortex shedding: where the flow accelerates in streamwise direction, regions of stronger and weaker velocity can be distinguished. The regions of weaker velocity magnitude where the flow is pulled back towards the cylinder, are interpreted as locations of vortex cores. Those are indicated by black lines in the figure.

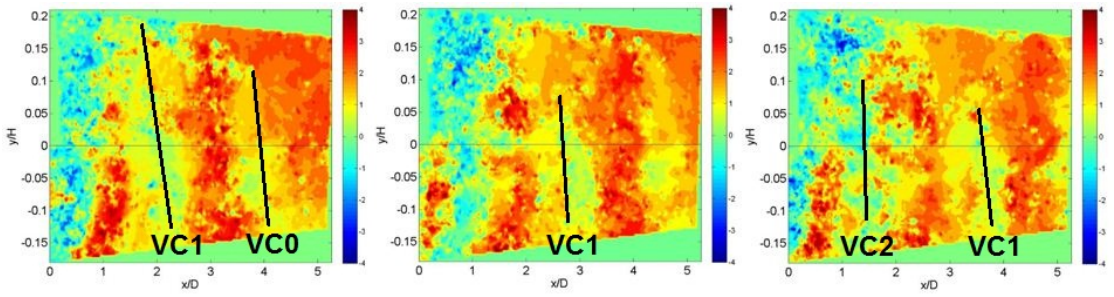


Figure 6.22: Instantaneous plots of the streamwise velocity U in the wake of cylinder D/d=2 at $Re_D = 51282.1$. Due to the high velocity and vortex shedding frequency, plots with a time distance of $\Delta t = \frac{1}{15}s$ were chosen.

Figure 6.23 shows the development of the out-of-plane velocity in the course of time. The first three pictures derive from the same time instants as the streamwise velocity plots in the previous figure. It is clearly seen that the locations of weak out-of-plane velocity in Figure 6.22 correspond to locations of vortex cores, as they are marked in Figure 6.23. Since vortices in this case could be identified from the streamwise velocity plots, it is assumed that a high Reynolds number leads to the creation of stronger vorticity in the cylinder wake than a low Reynolds number. In the present plots, vortex cores cannot be defined over the entire span. The small cylinder produces a higher number of vortices than the large diameter section does in the same time. As previously observed behind the step cylinder, vortices cannot always connect across the step region. This leads to connections with subsequent vortices, as seen in the encircled regions in the middle plots in middle and bottom rows.

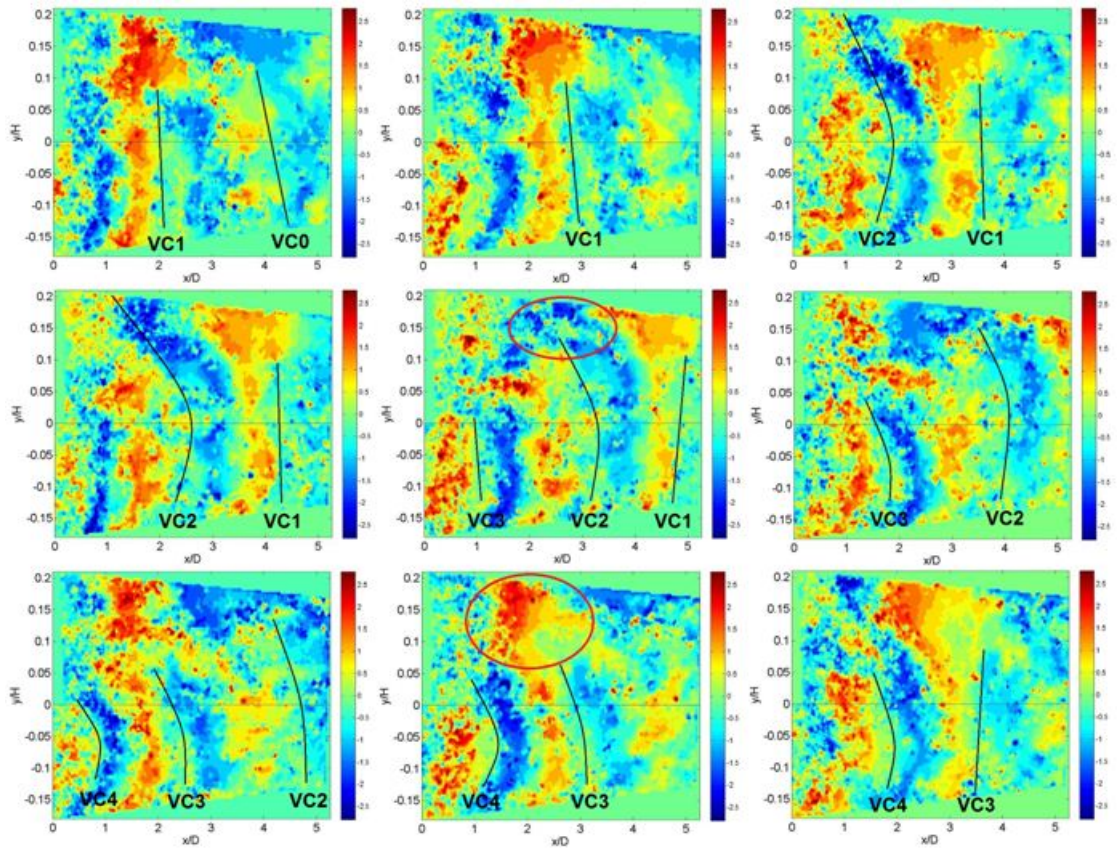


Figure 6.23: Instantaneous plots of the out-of-plane velocity component W in the wake of the cylinder D/d=2 at $Re_D = 51282.1$. The time distance between the respective plots is $\Delta t = \frac{1}{15}s$.

The present section discussed the instantaneous development of the flow field behind step cylinders in comparison with the reference cylinder. All figures were found in accordance with the mean plots presented in the previous chapter. The instantaneous sequences of plots gave further insight into the occurrences in the wake flow. Arguments for the occurence of vortex shedding were found in all investigated cases.

Comparing the results of the step cylinder experiments to those found from the analysis of the reference cylinder, a significant influence of the step on spanwise vortex shedding was discovered. The vortices behind the plain cylinder were present over the entire cylinder height. The cylinder with the small diameter ratio developed vortices with different shedding frequencies behind the large and the small diameter section, respectively. These connected across the step region with the result of an inclination angle. For the cylinder with the large diameter ratio,

connections over the step region were not always possible. In cases where vortex shedding in the wake of the small diameter section occured much faster, the vortices behind the small diameter region found their connecting partners in subsequent vortices.

From the presented results, a question arises concerning the effect of the step on the vortex shedding frequency. The discussed sequences are too imprecise to calculate the exact number of vortices shed in a specific time. The following chapter will therefore extract concrete vortex shedding frequencies in the cylinder wake from the collected data.

## 6.3 Spectral analysis

Vortex shedding frequencies and cells are found in the following by a spectral analysis of the measured flow fields. A vortex shedding cell is characterized by a specific, constant vortex shedding frequency, as e.g. found and described by Dunn and Tavoularis [3]. The spectral analysis provides a plot displaying the power spectral density (PSD) as a function of the vortex shedding frequency. Dominating shedding frequencies are located at maxima of the power spectral density. In the present case, the spectral analysis helps detecting the effect of the diameter step on the vortex shedding frequency when comparing results of the spectral analysis of step cylinders and the plain cylinder.

### a) Spectral analysis for cylinders with different diameter ratios

The spectral analysis was performed for all three examined cylinder models (see Figure 4.1). The effect of the step size on the vortex shedding frequency and on the number of distinct vortex shedding cells is investigated.

Spanwise vortices show by fluctuations of the out-of-plane velocity, as it was seen in Section 6.1. Therefore the power spectrum is obtained from the out-of-plane velocity signal. The results from the experiments with a Reynolds number of $Re_D = 2243.6$ for all cylinder models were chosen as an example for the comparison. The effect of an increase in Reynolds number on the vortex shedding frequencyis treated further down.

The spectral analysis starts out from the out-of-plane velocity in the wake of the

cylinder as a function of time. The calculation of this function is performed at one line in the wake. The location of this line was chosen at the eddy formation length $L_f$, since this location delivers the strongest signal (see Section 6.1).
Figure 6.24 presents the development of the out-of-plane velocity with time behind the reference cylinder D60. The plot is characterized by defined areas of postitive, alternating with areas of negative velocity, an indication of regular vortex shedding. Each vertical border between a positive and a negative velocity region that has negative region to the left and positive region to the right, is considered a vortex core. An example is indicated by a vertical yellow line in the Figure at approximately t=80s. The plot then shows 27 vortex cores within the displayed experiment duration of 206s. As a first estimate, a vortex shedding frequency of $f_v = \frac{27}{206s} = 0.131\frac{1}{s}$ is expected as a result of the spectral analysis. This frequency can be expressed in terms of the Strouhal number as $St = \frac{f_v * D}{U_{inflow}} = \frac{0.131\frac{1}{s} * 60mm}{35\frac{mm}{s}} = 0.225$.

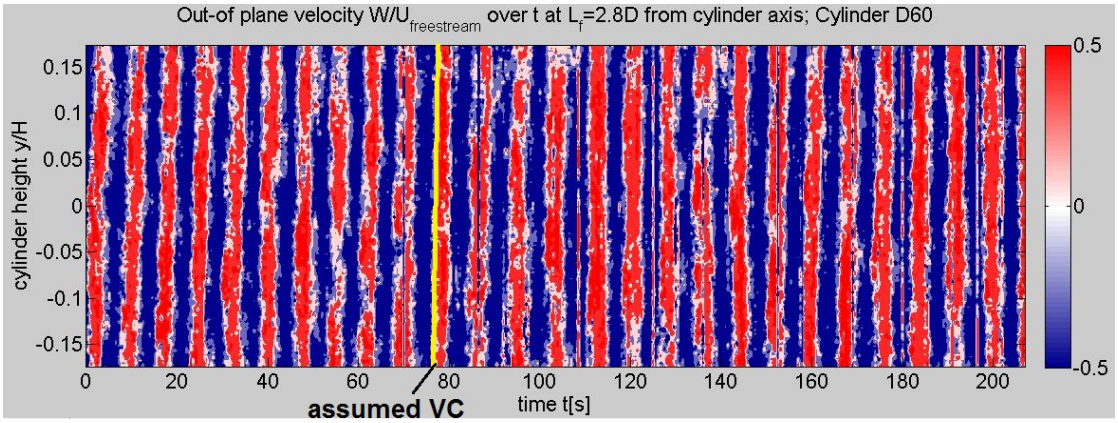


Figure 6.24: Out-of-plane velocity in the wake of the reference cylinder as a function of time, measured at $L_f$. $Re_D = 2243.6$.

Next, each row in the plot in Figure 6.24 is interpreted as a signal. Spectra were created from the signals, using Welch's method. This method was chosen over FFT and Covariance, as in this case it resulted in the clearest presentable spectra. After having been processed, the signals were written into a common matrix, representing the power spectral density over the entire cylinder span. In Figure 6.25, the power spectral density (PSD) was plotted for the reference cylinder. The x-axis shows the Strouhal number as a dimensionless vortex shedding frequency. The y-axis represents the cylinder span, normalized with the cylinder's total height H.

A distinct peak is identified at a Strouhal number of $St_D = 0.221$. This is the main frequency with which vortices are shed from the plain cylinder. It is very close to the expected Strouhal number of 0.225 from the first estimate.

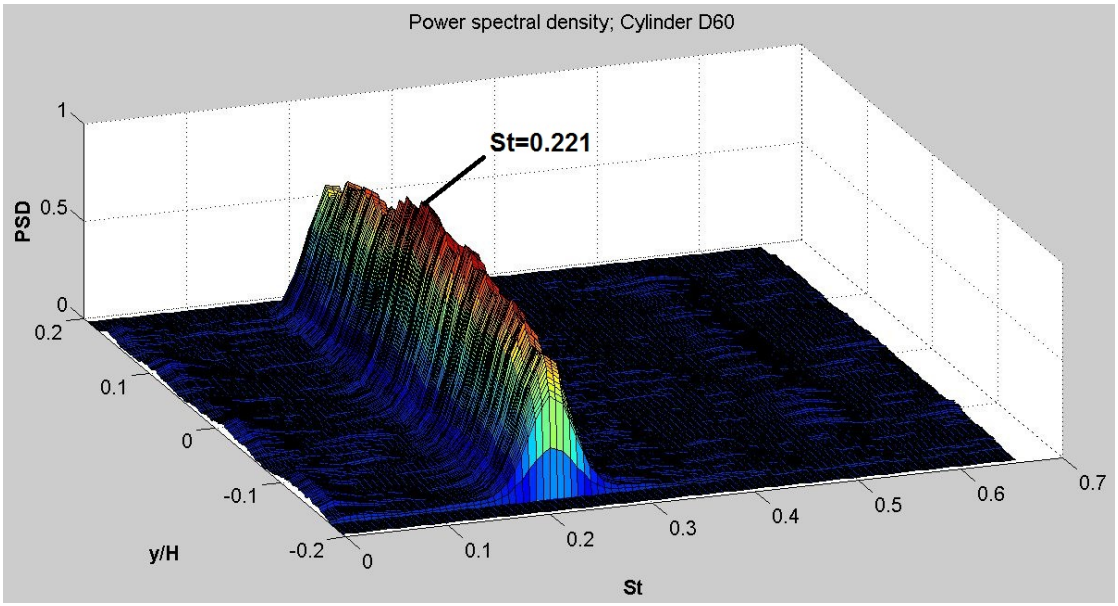


Figure 6.25: Power spectral density in the wake of cylinder D60 as a response to $Re_D = 2243.6$.

Based on the result for the reference cylinder, the spectral analysis was performed in the same manner for the step cylinder D/d=6/5. The out-of-plane component W is displayed as a function of time in Figure 6.26. The resulting spectrum is given in Figure 6.27.

From the velocity development with time it is seen that vortex shedding is not as regular for the step cylinder as it was behind the plain reference cylinder. Regular connections of vortices across the indicated step region occurs for example in the period between 30 and 50 seconds. However, the encircled regions exemplarily highlight locations where vortices come out of phase and do not connect to a direct partner on the other side of the step. Assuming as for the plain cylinder that one positive and one negative velocity region together form a vortexr, 31 vortex cores are counted behind the small diameter section, while only 27 vortices are found in the large diameter wake. At least two distinct vortex shedding frequencies are therefore expected as a result of the spectral analysis, the frequency in the smal diameter wake being higher than the frequency in the large diameter wake. With respect to the duration of the experiment of 216s that is displayed on the time

axis, vortex shedding frequencies of $f_{v_L} = \frac{27}{216s} = 0.125\frac{1}{s}$ and $f_{v_S} = \frac{31}{216s} = 0.144\frac{1}{s}$ are calculated from the plot. These correspond to Strouhal numbers with respect to the large diameter of $St_{D,L} = 0.214$ and $St_{D,S} = 0.247$.

Vortex shedding frequencies are found at locations of PSD maxima. In the wake of the large diameter section in Figure 6.27, the PSD maximum is located at $St_{D,L} = 0.214$, while in the small diameter wake, the peak is found at $St_{D,S} = 0.255$. The previously expressed assumtion of the vortex shedding frequency behind the small diameter section being higher than the frequency behind the large diameter section is therefore confirmed. The vortex shedding frequency behind the large diameter section is close to the previously calculated vortex shedding frequency in the wake of the reference cylinder. This is reasonable, since both the reference cylinder and the large diameter section of the step cylinder are of the same diameter. In the large diameter wake, the frequency results exactly as estimated with the help of the previous plot. The value for $St_{D,S}$ is very close to the estimation. The result for the PSD is therefore considered realistic.

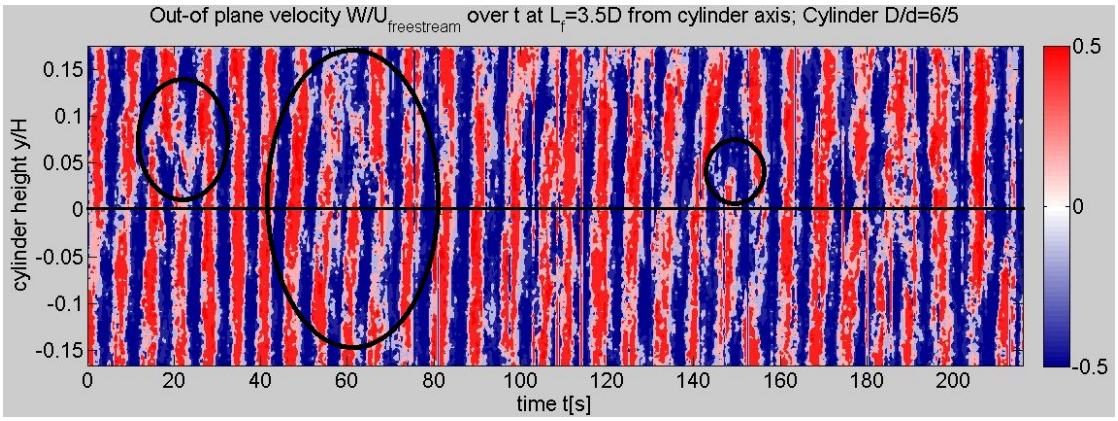


Figure 6.26: Out-of-plane velocity component as a function of time for the step cylinder D/d=6/5 at $Re_D = 2243.6$.

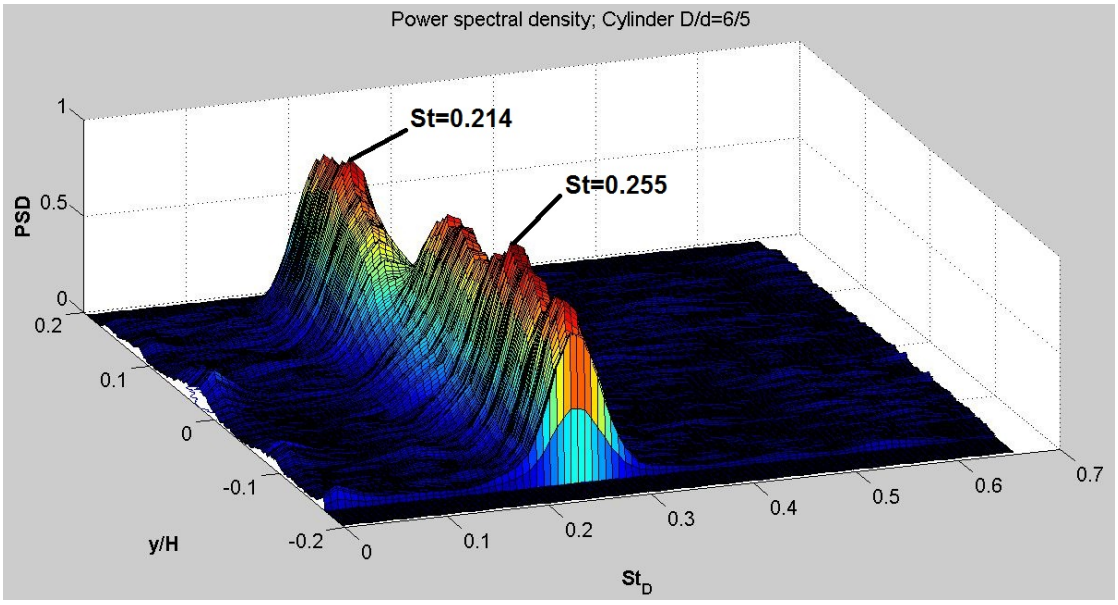


Figure 6.27: Power spectral density in the wake of cylinder D/d=6/5 as a result of a Reynolds number $Re_D = 2243.6$. Maxima are located at $St_{D,L} = 0.214$ in the large diameter wake and at $St_{D,S} = 0.255$ in the small diameter wake.

Finally, the spectral analysis was performed for Cylinder D/d=2. The out-of-plane component over time along with the PSD are presented in Figures 6.28 and 6.29. From Figure 6.28, 29 vortex cores are counted behind the large diameter section, while approximately 50 vortex cores are found in the wake of the small diameter section. It is obvious that the vortex shedding frequency behind the large diameter section is lower than behind the small diameter section. Shedding frequencies of approximately $f_{v,L} = \frac{29 vortices}{216 s} = 0.134$ ($St_{D,L} = 0.23$) in the large diameter wake and $f_{v,S} = \frac{50 vortices}{216 s} = 0.231$ ($St_{D,S} = 0.397$) in the small diameter wake are first estimates.

In Figure 6.29, maxima of the PSD are found at $St_L = 0.214$ behind the large diameter section and at $St_S = 0.4018$ for the small diameter wake. The vortex shedding frequency behind the large diameter section coincides with the vortex shedding frequency behind the large diameter section of Cylinder D/d=6/5 and the reference cylinder. The values for cylinder D/d=2 are close to the values expected from Figure 6.28. Close to the step region and in the large diameter wake, three additional maxima are found. The peak at St=0.1875 is identified as the beat frequency, created by substraction of $St_{D,L}$ from $St_{D,S}$. According to Lewis and Gharib, "The beat period corresponds to the time between each of

the local frequencies" [9], p.109. Additional vortex shedding cells with Strouhal numbers of $St_D = 0.275$ and $St_D = 0.355$ are discovered in the step region. The latter frequency is found close to the second harmonic of the beat frequency.

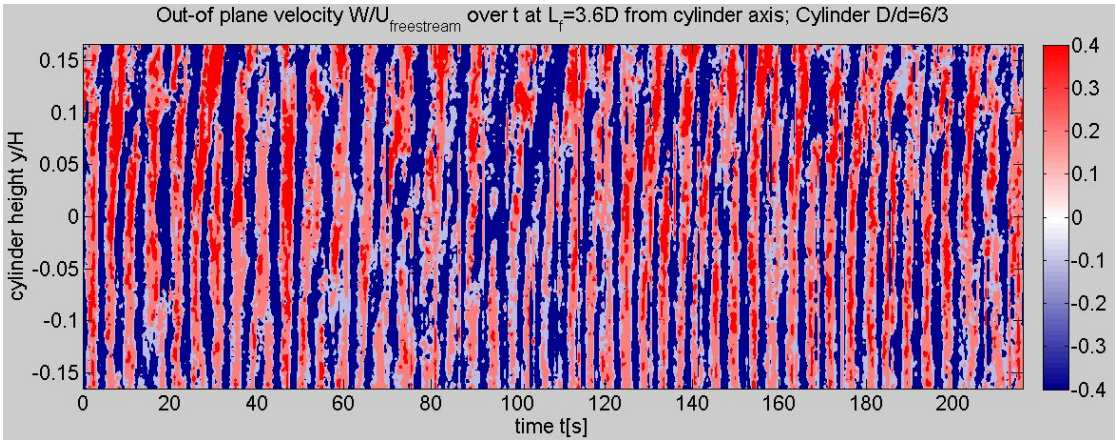


Figure 6.28: Out-of-plane velocity component in the wake of cylinder D/d=6/3 as a function of time. Measured at $L_f$. $Re_D = 2243.6$.

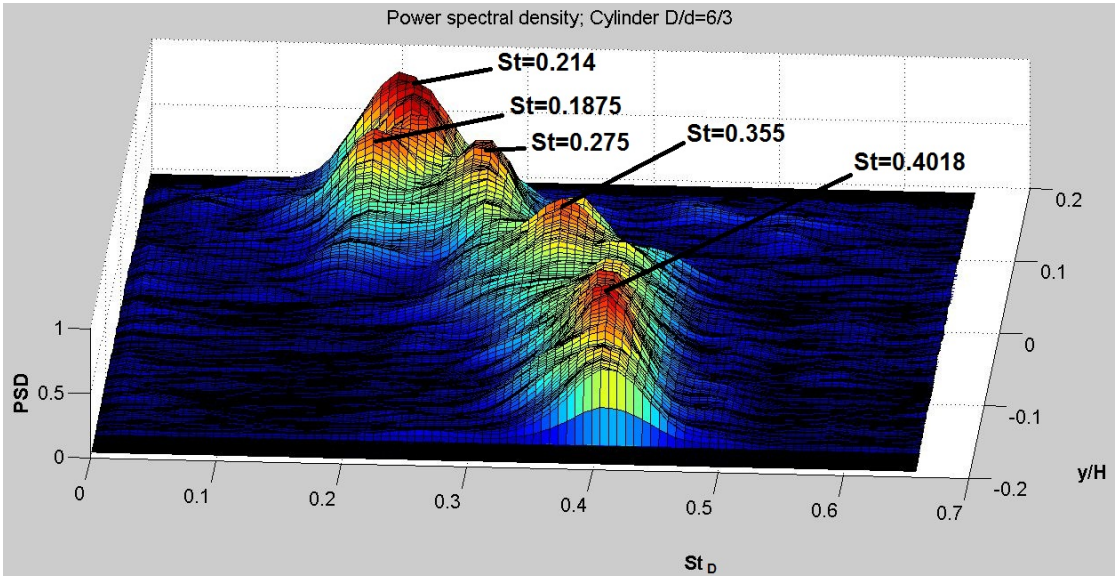


Figure 6.29: Power spectral density in the wake of cylinder D/d=6/3 as a result of $Re_D = 2243.6$. Spectral peaks are indicated in the figure.

The investigation in this chapter showed the occurance of several vortex shedding cells in the wake of step cylinders, in contrast to the plain cylinder, where one single vortex shedding cell could be located. Cylinder D/d=6/5 developed two disctinct vortex shedding cells in its wake, while in the wake of cylinder D/d=2,

five distinct vortex shedding frequencies were found. It is conluded that the size of the step has significant influence on the number of developing vortex shedding cells. A summary of the discovered values for the Strouhal number is found in Table 6.2 at the end of the following section.

**b) Reynolds number influence**

The effect of an increase in Reynolds number on the flow features is a main focus of this work. Spectral analyses were therefore performed for experiments 4.042 and4.044. The results will be compared to the results for the previously discussed Reynolds number $Re_D = 2243.6$.

Previously, the eddy formation region at a Reynolds number of $Re_D = 12820.5$ was located at $L_f = 1.8D$. The velocity signal was estimated at this location. The resulting plot of the out-of-plane velocity with time is seen in Figure 6.30, followed by the corresponding power spectrum in Figure 6.31.

As a first estimate from Figure 6.30, $f_{v,L} = \frac{36 vortexcores}{59s} = 0.610\frac{1}{s}$ ($St_{D,L} = 0.183$) and $f_{v,S} = \frac{81 vortexcores}{59s} = 1.373\frac{1}{s}$ ($St_{D,S} = 0.412$) are calculated. The figure illustrates the difference in shedding frequency behind the respective diameter sections very clearly.

The power spectral density plot shows peaks at $St_{D,L} = 0.182$ and $St_{D,S} = 0.398$. These calues are very close to the estimates from the previous figure. In contrast to the spectrum at a lower Reynolds number, the present spectrum shows only two distinct peaks, respresenting vortex shedding frequencies behind small and large diameter section. The peak in the small diameter wake however is pronounced as a double peak. There is no distinct maximum close to the step. As a conlusion, regular vortex shedding takes place further away from the step, but not in the step region. Vortex shedding activity in the large diameter wake is not discovered closer to the step than y=0.14D. Figure 6.13 supports this insight. In this figure, the fluctuation behind large and small diameter section was significantly stronger than in the step region.

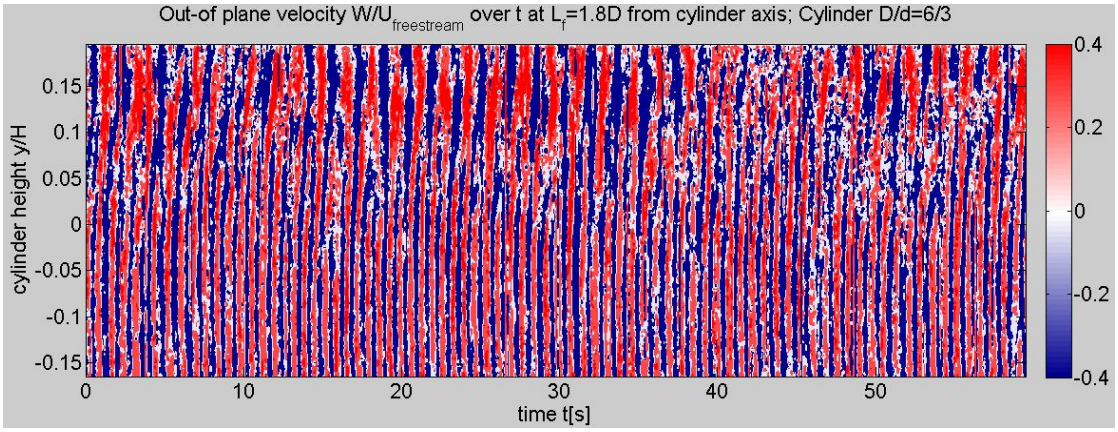


Figure 6.30: Out-of-plane velocity over time behind step cylinder D/d=2 at $Re_D = 12820.5$.

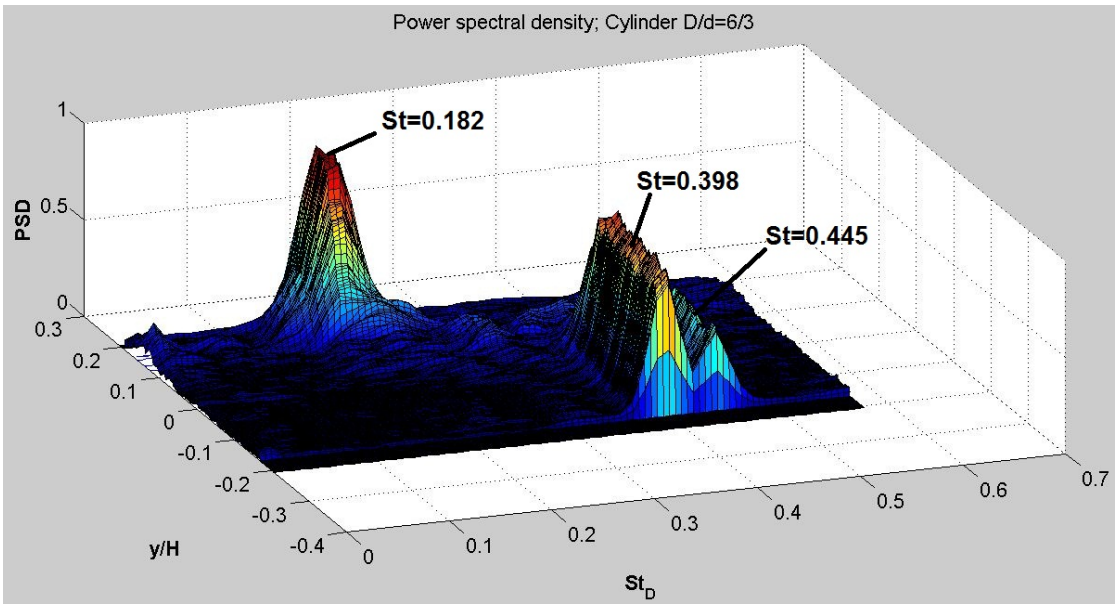


Figure 6.31: Power spectral density behind step cylinder D/d=2 at $Re_D = 12820.5$.

Figure 6.32 shows the power spectrum for $Re_D = 51282.1$. The velocity component over time is not presented in this case, due to a strong influence of turbulence that inhibits regular features to develop in a visible range. Turbulence also shows in the velocity spectrum as a large amount of small peaks. A distinct peak however is found at $St_{D,L} = 0.650$ in the large diameter wake. The peak is located at y=0.14, with respect to the diameter step. In the small diameter wake, no distinct peak shows. Maxima that seem rather unphysical develop however very close to St=0. Turbulence might play a decisive role in this case. Perhaps vortex activity in the small diameter wake is inhibited by chaotic fluctuation.

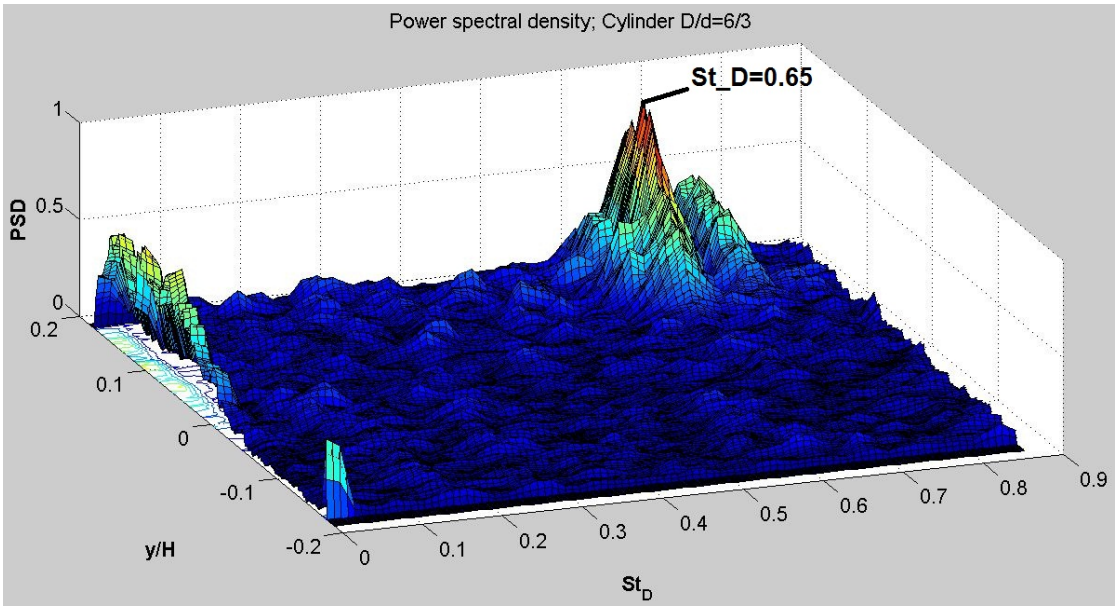


Figure 6.32: Power spectral density behind step cylinder D/d=2 at $Re_D = 51282.1$.

Table 6.2 summarizes the findings in the present and the previous chapter by listing values of Strouhal numbers discovered in all cases.

| Cylinder | $Re_D$ | $St_{D,L}$ | $St_{D,S}$ | additional frequencies |
|---|---|---|---|---|
| D/d=1 | 2243.6 | 0.221 | | |
| D/d=6/5 | 2243.6 | 0.214 | 0.255 | |
| D/d=2 | 2243.6 | 0.214 | 0.402 | 0.188, 0.275, 0.355 |
| D/d=2 | 12820.5 | 0.182 | 0.398 | 0.445 |
| D/d=2 | 51282.1 | 0.650 | | |

Table 6.2: Strouhal numbers $St_D$ that were found in the wake of the cylinder models at different Reynolds numbers.

Figure 6.33 shows the Strouhal number as a function of the Reynolds number for circular cylinders [17]. The Reynolds number range studied in the present work was marked by two vertical red lines. It is clearly seen that the Strouhal numbers in the small diameter wake of all step cylinders was significantly higher than suggested by the diagram. The larger the diameter step, the higher were the resulting values. It is therefore concluded that the presence of the step as a sharp edge has a significant influence on the vortex shedding frequency, especially in the small diameter wake.

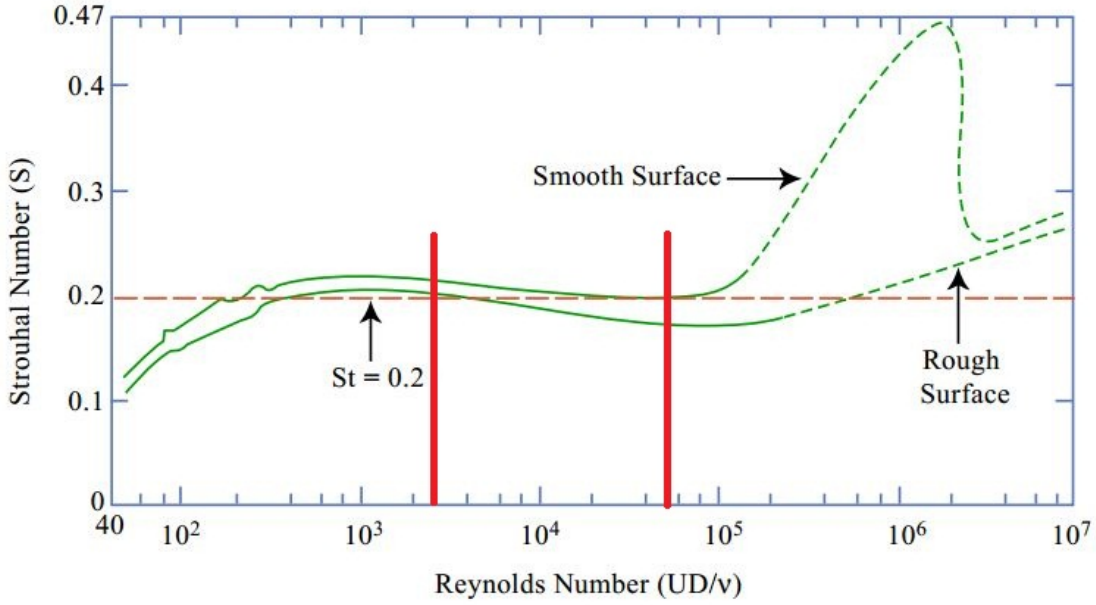


Figure 6.33: Strouhal number as a function of Reynolds number for circular cylinders [17].

## 6.4 Measuring in additional planes

The aim of the present chapter is to establish a model of the spanwise vortices behind the cylinder models. In order to do so, the light sheet on the cylinder was displaced out of the symmetry plane of the cylinder. This way, the flow field was measured in several planes parallel to the mid plane of the cylinder. The measurement planes are shown in Figure 6.34. In the following, the instantaneous velocity in these planes will be discussed, leading to the attempt of establishing a model for the vortex development in the wake of both the plain and the step cylinder with a diameter ratio of D/d=2.

In Figure 6.35, the flow field around a circular cylinder is illustrated for the Reynolds number range discussed in this report compared to a lower Reynolds number range with laminar flow features. It is seen that vortices detach alternatingly from the upper and lower side of the cylinder. If this illustration applies to the present case, vortex activity might be stronger in x-y-planes parallel to the cylinder axis than it was measured in the midplane. This is investigated by discussing results in three different planes parallel to the cylinder axis.

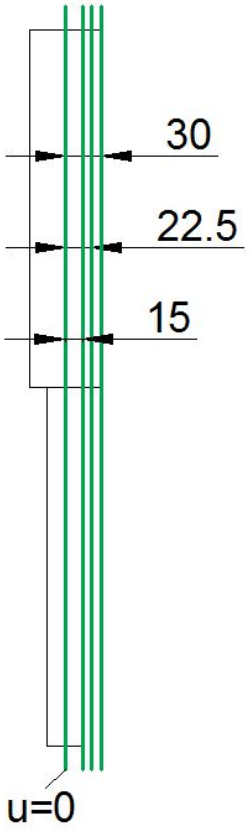


Figure 6.34: Lightsheet displacement for experiments 5.054-5.244, shown for the step cylinder D/d=2. The same distances from the symmetry plane were chosen for the plain cylinder.

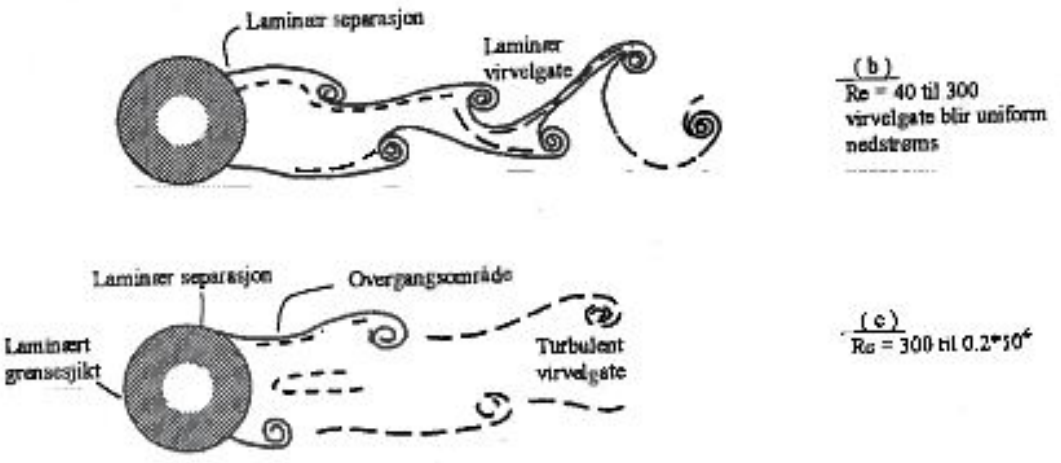


Figure 6.35: Flow field behind a circular cylinder at different Reynolds numbers [15]. All experiments discussed in this report were performed in the Reynolds number range represented by the lower sketch.

At first, a sequence of out-of-plane velocity plots in all measurement planes is presented for the reference cylinder D/d=1 at $Re_D = 2243.6$ in Figure 6.36. From top to bottom row, the lightsheet was moved further towards the outer edge of the cylinder.

In the upper row, which was captured in the symmetry plane of the cylinder, a regular alternation of out-of-plane velocity is observed, slightly disturbed by turbulent features that unravel the edges of the distinct velocity regions. The plots were previously discussed in Section 6.2 as part of a longer time series.

Regular flow features with a lower influence of turbulence are observed in the second and third row of the figure. The magnitudes of both positive and negative velocity regions are higher than for the central plane, while the borders between the velocity regions are defined more clearly. Velocity magnitudes are highest in the plane that was displaced by u=15mm with respect to the initial measurement plane. These observations lead to the assumption that the vortex core is found close to the plane at u=15mm. It is also seen that while the plots in the upper row show a region of zero out-of-plane velocity just behind the cylinder, the plots in the second and third row show velocity development much closer to the cylinder. An interpretation of this occurrence is illustrated in the following figure.

Finally, the last row shows a constant narrow area of negative velocity just behind the cylinder, followed by a region of zero velocity, and alternation in the velocity component further downstream. Here, the alternation is characterized by large regions of negative velocity, followed by slender regions of positive velocity.

All interpretations are summarized in Figure 6.37, which is also based on knowledge from Figure6.35.

Central plane (zero displacement):

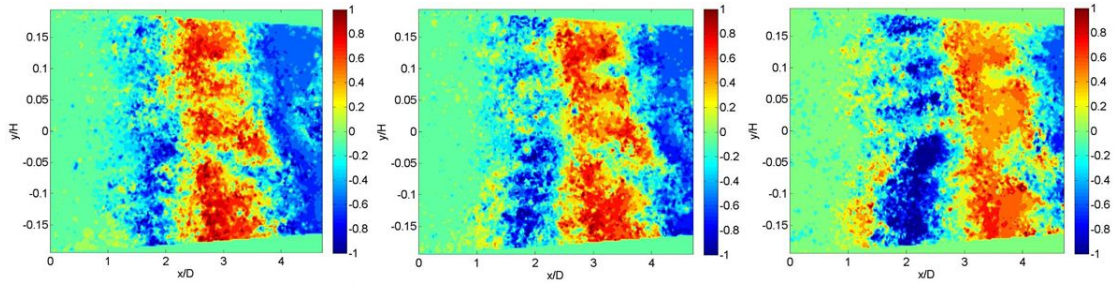


Displacement 15mm:

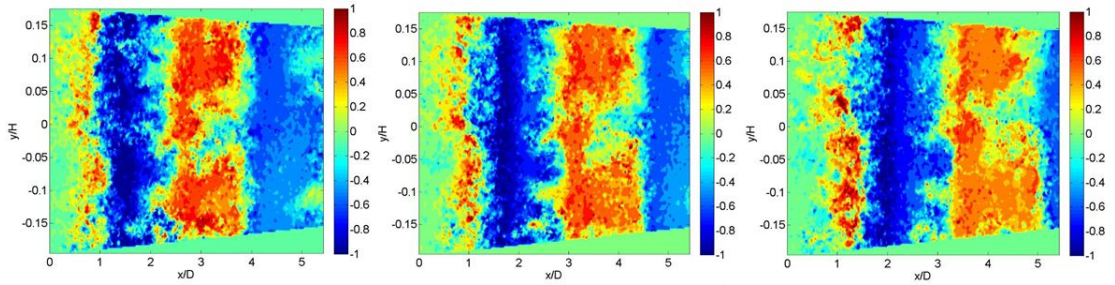


Displacement 22.5mm:

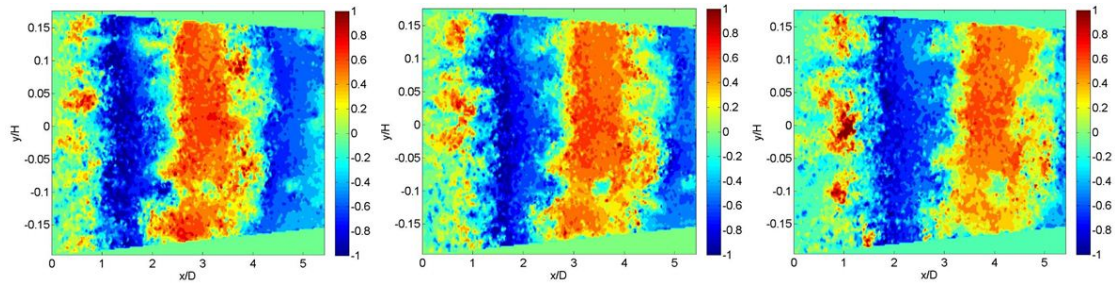


Displacement 30mm:

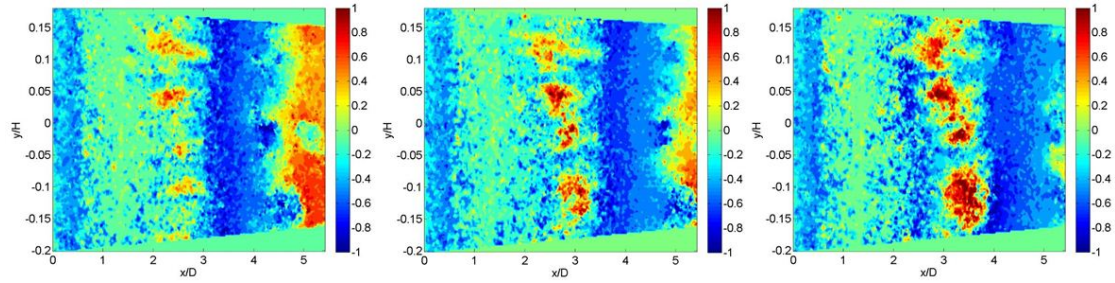


Figure 6.36: Out-of-plane velocity as a function of time as a result of $Re_D = 2243.6$. From top to bottom plots, the measurement plane was displaced from the center plain by the given value.

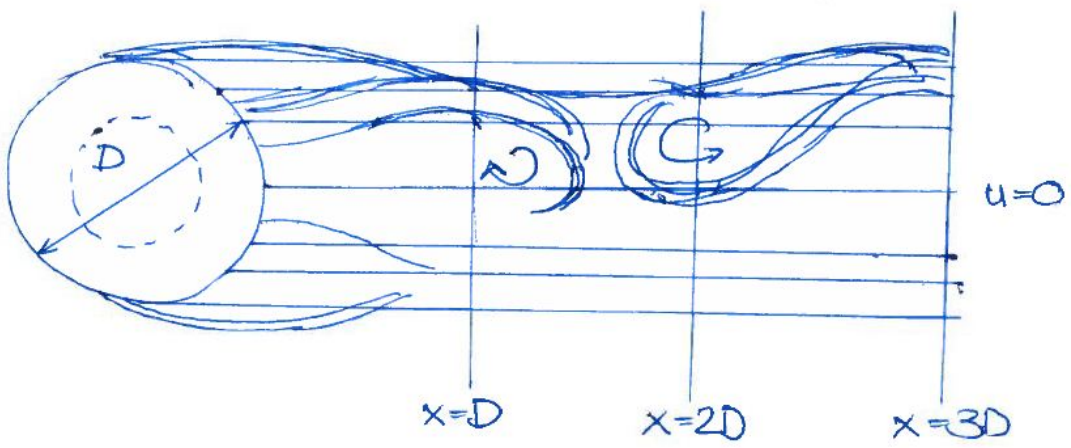


Figure 6.37: Interpretation of the measured flow characteristics behind cylinder D/d=1 at Re=2243.6.

Knowing some features of the 3D flow field behind the plain cylinder, it is now interesting to have a look at the step cylinder D/d=2 in this connection, in order to investigate the influence of the lower cylinder and the step on the flow behavior. Figure 6.38 presents four rows of instantaneous velocity plots, each row measured in one light sheet plane.

The plots in the first row were dicussed in Section6.2 as a part of a longer time series. The important feature is seen in the first plot as the connection of two negative velocity regions in the wake of the small diameter section with a single negative velocity region behind the large diameter section. In the subsequent plot, the connection to the first region in the small diameter wake dissolves. The last plot of the series shows the features of almost regular vortex shedding.

The further the light sheet was displaced out of the central plane, the stronger the decrease in velocity magnitude, both for positive and for negative velocity regions. Furthermore, the further out of the middle the measurement plane, the stronger the connection between one negative velocity region in the large diameter wake and two negative velocity regions in the small diameter wake. At the same time, the connection takes place further up on the span. With an increasing desplacement the level of disturbance of the flow features increases.

It is assumed that the cores of the vortices in large and small diameter wakes, which partly connect, are found closer to the symmetry plane than for the plain cylinder with a diameter corresponding to the large diameter section. Probably

vortices tend to lean not only backwards respectively forwards, but also outwards towards the outer measurement plane. This is derived from the observation that vortices in the outer planes connect in a higher location than in the symmetry plane.

Central plane (zero displacement):

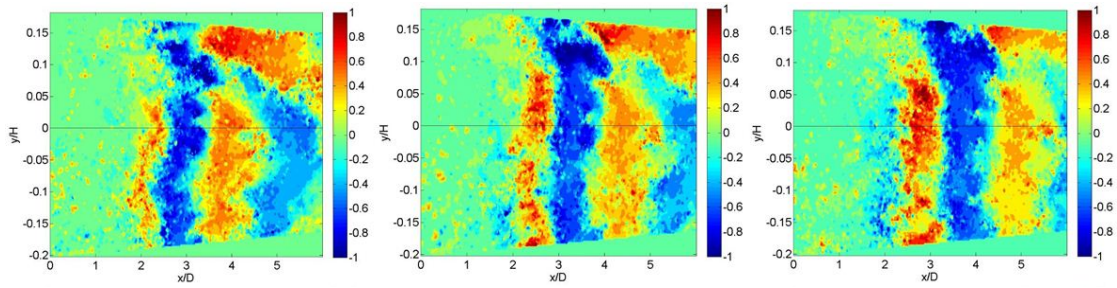


Displacement 15mm (outer egde of small diameter section):

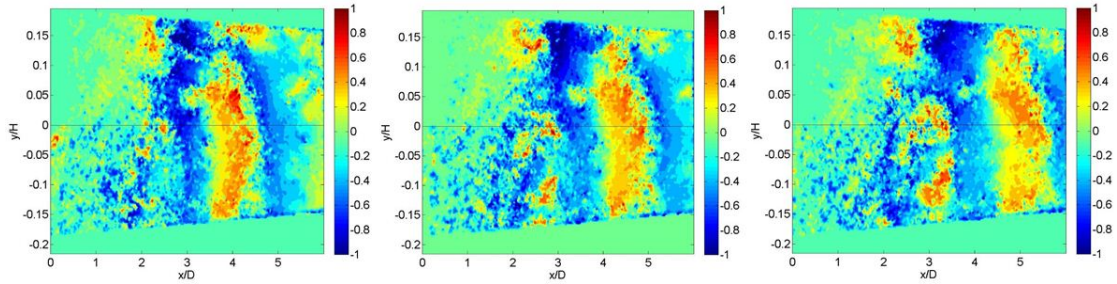


Displacement 22.5mm (on the step):

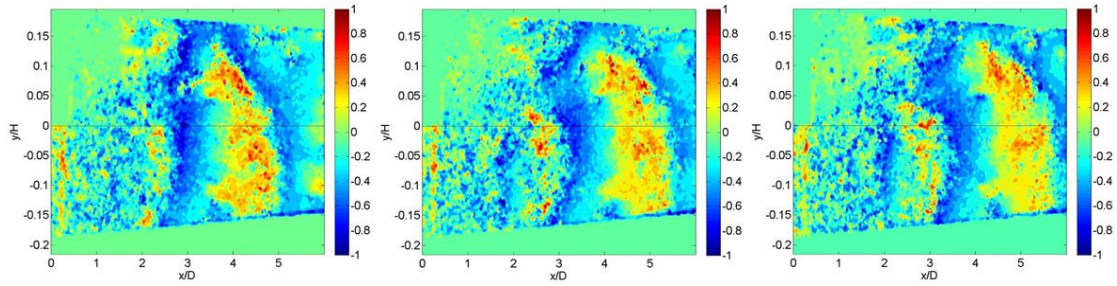


Displacement 30mm (outer edge of large diameter section):

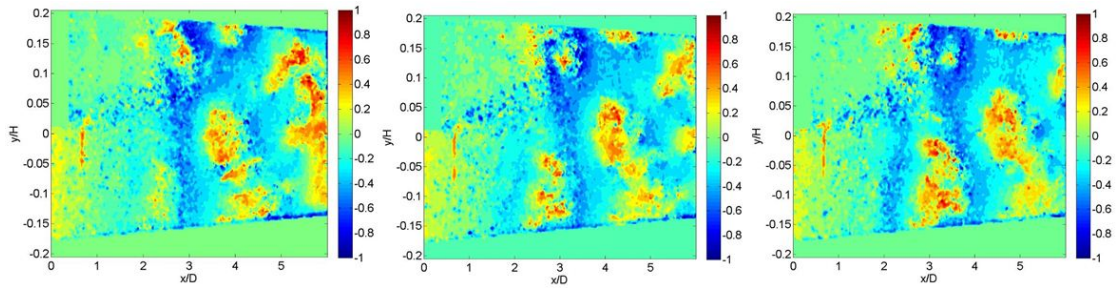


Figure 6.38: Out-of-plane velocity as a function of time as a result of $Re_D = 2243.6$ for the step cylinder D/d=2. From top to bottom plots, the measurement plane was displaced from the center plain by the given values.

The stated flow features are well illustrated by Morton, Yarusevych and Carvajal-Mariscal [13] (see Figure 6.39). Vortex cores and connections are found close to the cylinder axis. Coming from there, vortices lean forwards and backwards, as well as outwards.

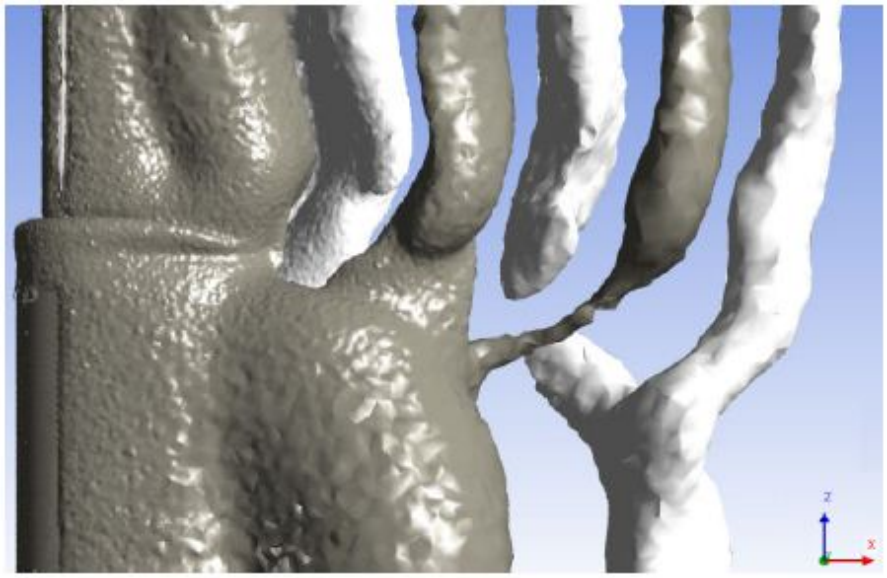

Figure 6.39: Computational result of flow behind a step cylinder [13]. Vortex locations and trends are illustrated. Note the reverse orientation of the cylinder, in contrast to the present report.

## 6.5 Measuring in the x-z-plane

### a) Symmetry plane

An additional set of experiments (6.041-6.044) was performed in order to receive further insight into vortex development. The lightsheet was now oriented in the x-z-plane (see Figure 6.47 and Figure 1.1 for axis orientations).
Instead of rotating the laser light sheet by 90°, the cylinder models were turned in order not to endanger involved people by a horizontally spreading light sheet. This was possible because it has been proven that the flow development in the wake of a step cylinder is not dependent on gravity (see [3, 18]). Therefore the arrangement of the cylinder model was not crucial.
With a camera setup as used in Figure 2.3 (Setup 1), data in the step region would be likely to get lost for one camera. Hence for this experiment series both cameras were mounted on the same side of the measurement section, as seen in Figure 6.40.

With this additional experiment series, it was aimed for verification of the findings on the eddy formation length in Section 6.1. In addition, it was intended to investigate the vortex positions with respect to the cylinder's symmetry axis and its accordance with Figure 6.35. Furthermore, a spectral analysis was performed on the data, in order to find previous results on vortex shedding frequencies supported or disclaimed.

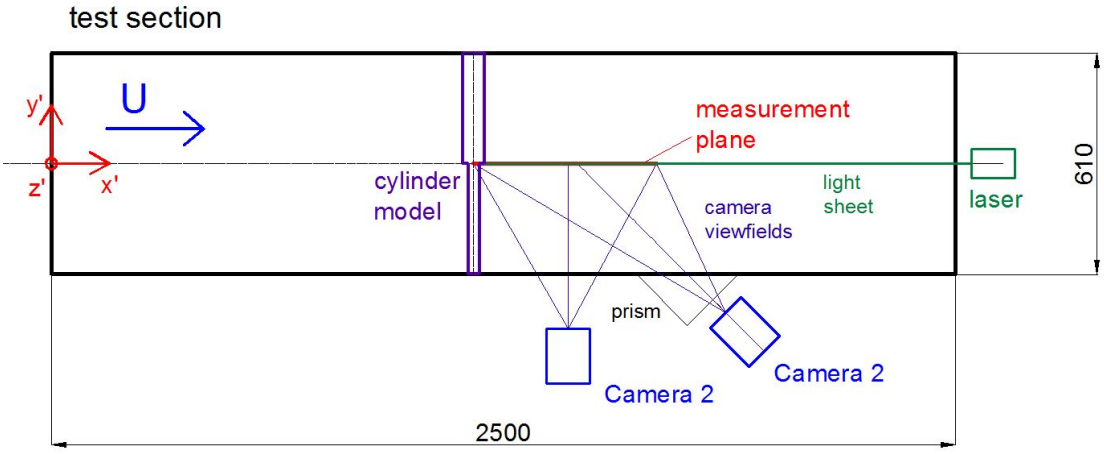


Figure 6.40: Setup 3 for the investigation of the horizontal cylinder. Both cameras are located on the same side of the measurement section, in order to avoid a shadow with data loss.

In experiment 6.044, the first measurement with Setup 3, the lightsheet was placed directly on the step. Figure 6.41 shows the view field of camera 1 as a basis for the following plots.

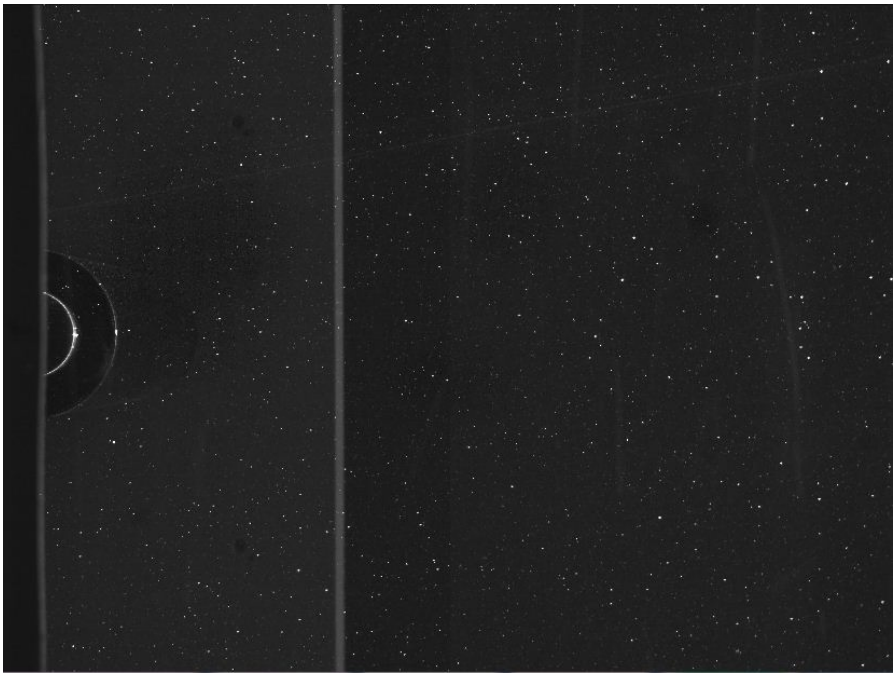

Figure 6.41: View field of Camera 1 for Setup 3: On the left edge, a part of the model frame is visible. In the data evaluation, this part will return zero velocity. The laser light sheet illuminates the small and the large diameter section. The vertical line in the image represents the model frame on the other side of the measurement section. Its reflection is dark enough not to disturb particle tracking.

Figure 6.42 presents a short sequence of instantaneous plots that show the characteristics of the wake field. From Figure 6.41 it is known that the region on the left edge of the image corresponds to the model frame. The position of the cylinder axis can also be estimated from Figure 6.41. Figure 6.42 intends to show the exact locations of spanwise vortices in the cylinder wake. The color coding represents the vorticity in the considered plane, which was calculated as $\zeta = \frac{\partial V}{\partial x} + \frac{\partial U}{\partial y}$ Locations of vorticity extrema represent vortex cores. As the y-axis points out of the plane towards the viewer, vorticity minima stand for clockwise vortices, while vorticity maxima represent anticlockwise vortices. The vector plot shows the in-plane velocity. Here, the inflow velocity was substracted from the streamwise velocity component, in order to illustrate the flow behavior around vorticity minima and maxima. The velocity vectors were magnified by a factor of 4. It is seen that the velocity is deflected by vorticity extrema and vortices are created.

In the upper plot, a vortex with positive sign is about to detach from the eddy

formation region. At the same time, a negative vortex forms on the upper side of the cylinder. In the bottom plot, the negative vortex is detaching, while a new positive vortex is about to form. Previous findings concerning the length of the eddy formation region $L_f$ are supported by this figure. While there is no vortex activity just behind the cylinder, the region of strong activity is discovered at approximately $L_f = 3D$ downstream of the cylinder axis. Due to the strong magnification of the velocity in the Figure, backflow behind the cylinder is observed stronger than in reality.

In addition, the results from experiments 5.054-5.244 with the displaced lightsheet are supported: vortex activity is spread over the entire cylinder diameter. This result also corresponds to the theory for the second regime in Figure 6.35.

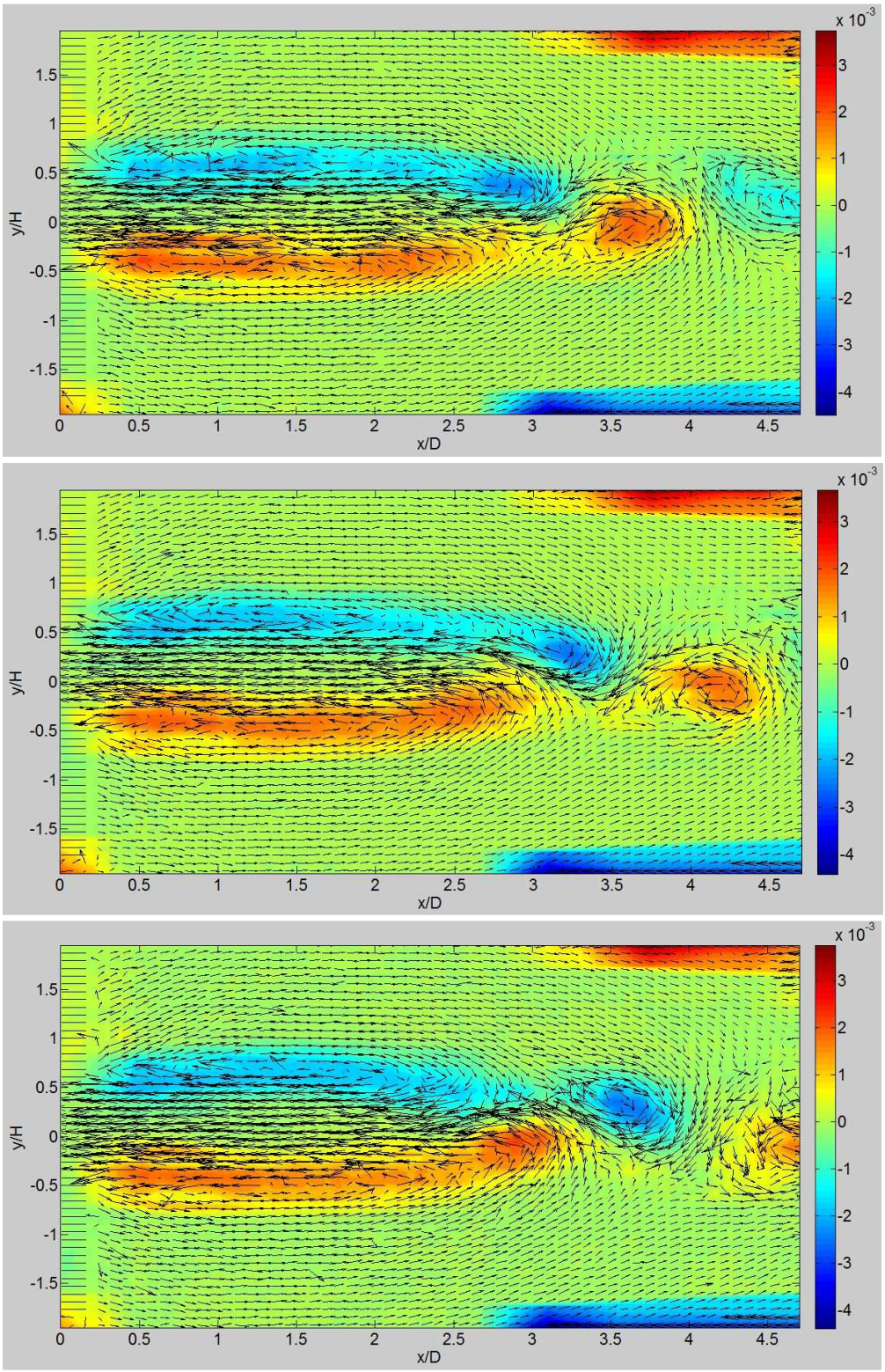


Figure 6.42: Wake flow field behind the step of cylinder D/d=2 at $Re_D = 2243.6$. The color coding represents vorticity in the plane, the vector plot shows velocity in the plane, respective $U_{inflow}$. The vectors have been magnified by a factor of 4.

Quantitative information about vortex shedding in the wake of the step cylinder is obtained from spectral analysis. Figure 6.43 shows the result of a spectral analysis where the signal of the velocity component W was used at x=3.5D, the location of strongest vortex shedding activity. A distinct peak is seen at $f_v = 0.111$, the corresponding Strouhal number is $St_D = 0.19$. A second peak is found at $f_v = 0.21$, which corresponds to a Strouhal number of St=0.36. In Table 6.3, the values are compared to values from previous evaluations in the present report. The second and third peak frequencies in the plot appear to be the second and third harmonics of the first and highest peak.

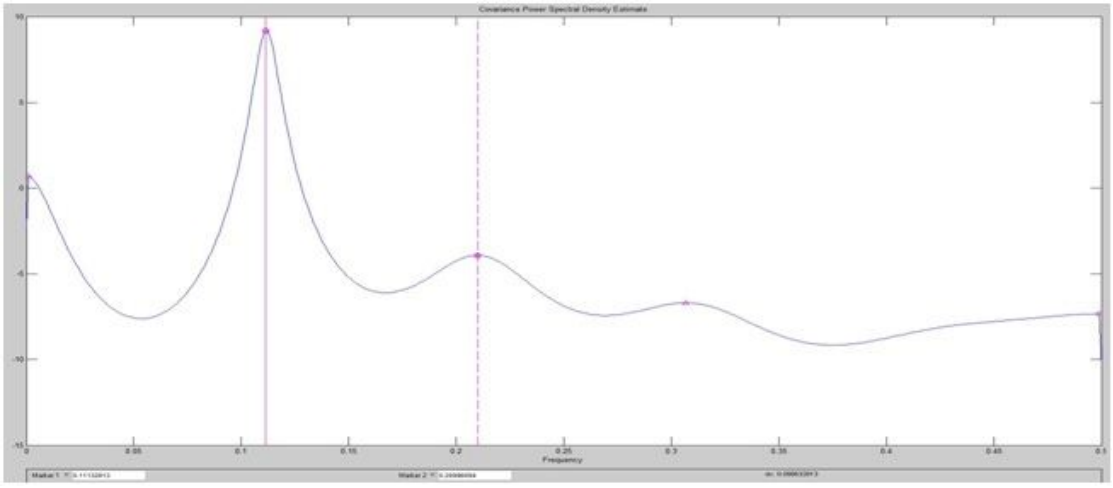

Figure 6.43: Power spectral density as a function of the vortex shedding frequency $f_v$, created from a signal from velocity component W. Cylinder D/d=2, Re(D)=2243.6. Maxima at $f_v = 0.111, 0.21, 0.36$.

In addition, a spectral plot was created for the streamwise velocity component U. This plot was expected to show the same peaks as the plot for the W-component, since the same vortices were represented. As a matter of fact, the values are very close: peaks in the spectral density plot are found at $f_v = 0.105(St = 0.18)$ and $f_v = 0.213(St = 0.365)$ (see Figure 6.44). The discrepancy of the values for the maxima is assumed to be a result of unsufficient data length. A longer data set would bring the resulting values closer.

Another characteristic is found when comparing the spectra in Figures 6.43 and 6.44: the peaks in the plot for the streamwise velocity are less pronounced than in z-direction. This is due to the fact that the fluctuation in z occurs about zero, while the fluctuation of the velocity in x must antagonize a positive mean value of

U, created by the inflow velocity. This was shown in the previous wake field plots in Figure 6.42, where the component W fluctuated between positive and negative values, while the streamwise component U fluctuated about a mean value and remained positive at almost all locations.

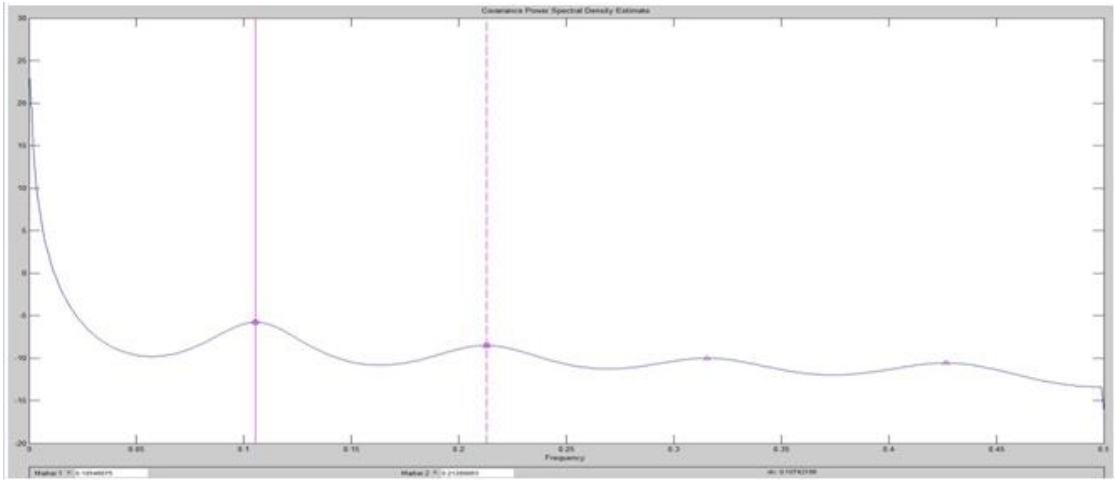

Figure 6.44: Power spectral density as a function of the vortex shedding frequency $f_v$, created from a signal from velocity component U. Cylinder D/d=2, Re(D)=2243.6. Maxima at $f_v = 0.105, 0.213$.

Next, the current results for a Reynolds number of $Re_D = 2243.6$ will be compared to results at the higher Reynolds number $Re_D = 51282.1$. The position of the highest vortex activity, as well as the vortex shedding frequency are of interest in this connection. In Figure 6.45, the instantaneous flow field is presented in the form of three plots, each with a time distance of $\Delta t = \frac{2}{15}s$. Comparing this plot with Figure 6.42, it becomes obvious that the area of strongest vortex activity has experienced a shift towards the cylinder to approximately x=2D. While for the low Reynolds number the plot showed about 3.5 vortices at the same time in the field of view, the plot for the high Reynolds number displays up to five vortices. From the colormap it is seen that the vorticity is up to 40 times stronger than in the low Reynolds number case.

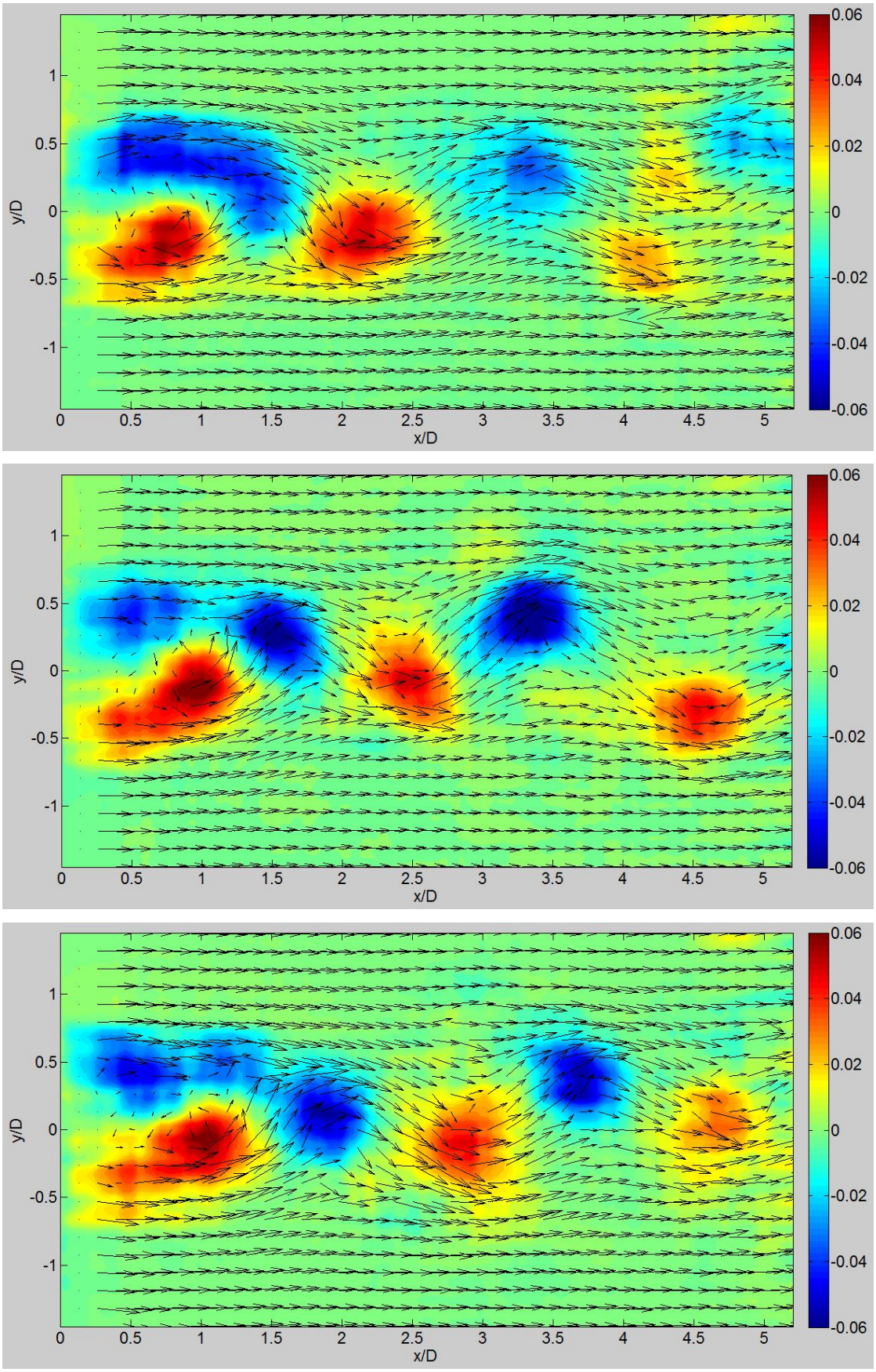


Figure 6.45: Wake flow field behind the step of cylinder D/d=2 at $Re_D = 51282.1$. Vector plot: in-plane velocity; Color plot: vorticity.

In Figure 6.46, the power spectral density was estimated from velocity signals in both x- and z-direction at x=2D. The curves show four distinct maxima that are comparable, but not identical in both cases. The values for frequencies and Strouhal numbers in both cases are listed in table 6.3.

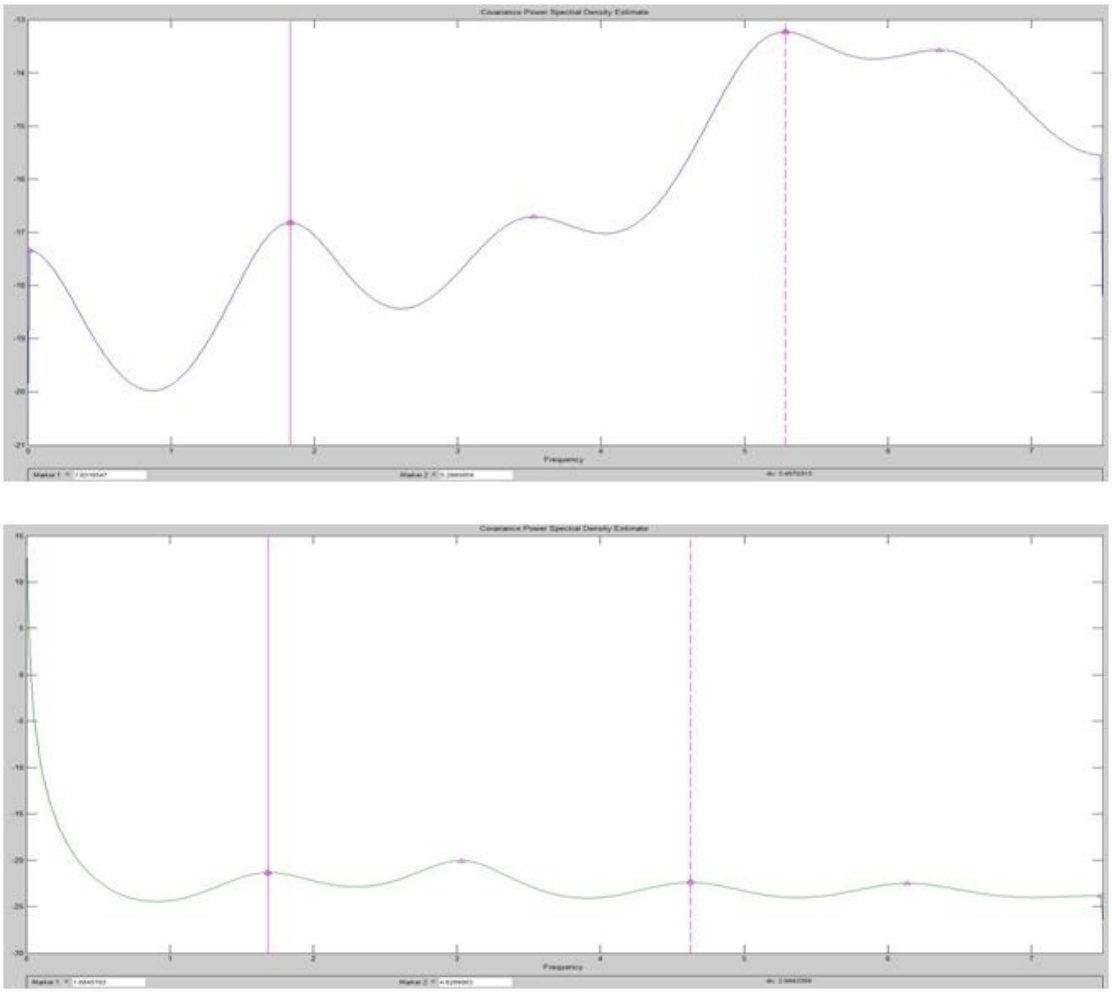

Figure 6.46: Power spectral density as a function of the vortex shedding frequency $f_v$, created from velocity signals in x- and z-directions. Cylinder D/d=2, $Re_D$ = 51282.1.

The section is concluded by a table that sums up the resulting values from all spectral analyses of the wake behind cylinder D/d=2 that were presented in the course of the present report. This includes the wake of the vertical cylinder in Setup 1 at different Reynolds numbers, as well as the wake behind the horizontal cylinder at different Reynolds numbers and for different flow components. It is found that for all measurements, except for at the largest Reynolds number, the Strouhal number behind the large diameter section is close to 0.2, as generally

suggested for circular cylinders in the given Reynolds number range in Figure 6.33. In the small diameter wake, the Strouhal number is close to 0.4 for all cases. It is interesting that additional Strouhal numbers were found in the wake of the cylinder at the lowest Reynolds number for Setup 1, but only for the highest Reynolds number for Setup 3. The additional Reynolds numbers for the respective cases do not coincide.

| Setup no. | $Re_D$ | Spectral component | $St_{D,L}$ | $St_{D,S}$ | additional St |
|---|---|---|---|---|---|
| 1 | 2243.6 | W | 0.214 | 0.402 | 0.188, 0.275, 0.355 |
| 1 | 12820.5 | W | 0.214 | 0.398 | 0.445 |
| 1 | 51282.1 | W | 0.65 | | |
| 3 | 2243.6 | W | 0.19 | 0.36 | |
| 3 | 2243.6 | U | 0.18 | 0.365 | |
| 3 | 51282.1 | W | 0.176 | 0.397 | 0.137, 0.265 |
| 3 | 51282.1 | U | 0.176 | 0.460 | 0.126, 0.227 |

Table 6.3: PSD maxima behind cylinder D/d=2 from spectral analyses performed for different setups at different Reynolds numbers.

### b) Measuring in additional planes

In order to add information about vortex development and vortex shedding frequencies along the cylinder to the current knowledge, experiments 6.144-6.444 were performed in additional planes parallel to the midplane (see Figure 6.47).

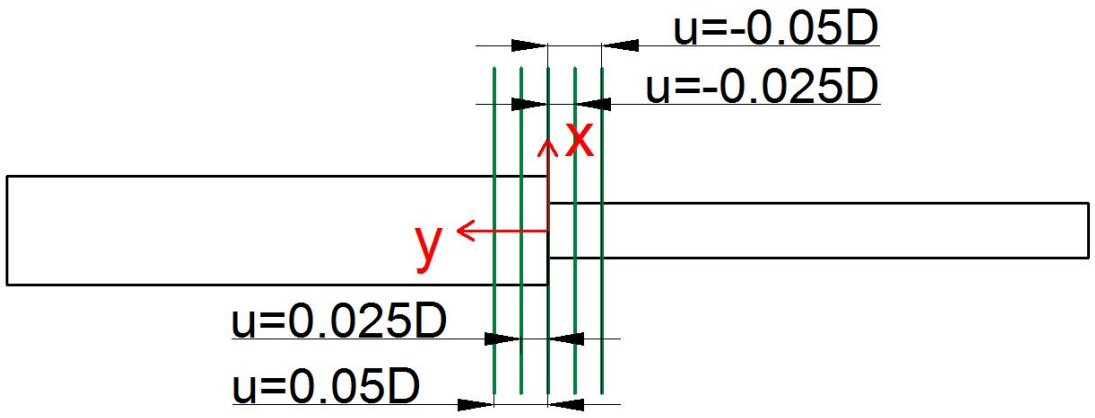


Figure 6.47: Moving the light sheet (green) from the midplane along the cylinder span in steps of 0.025D.

The results in the measurement planes are discussed coming from the positive

y-direction. All plots of the instantaneous wake are found at the end of this section.
At first, the measurement plane was displaced by u=0.05D from the step into the large diameter wake. The three plots in Figure 6.53 present captures of the instantanueous velocity in the wake with a time step of $\Delta t = 1s$. The color coding represents vorticity in the plane, the vectors show the in-plane velocity respective the inflow velocity in U. In the first plot, a vertical enlongation of the negative vortex on the right edge of the image is observed. In the second plot, the positive vortex elongates as well. It is seen that vortex shedding occurs on a regular basis, but with a deformation of vortices. This is interpretated as backwards stretching of vortices that connect to subsequent vortices, as it was seen in Section 6.2.

Next, results in the measurement plane at u=0.025D in the large diameter wake are discussed (see Figure 6.54). Vortex shedding does not appear regularly any more. Through the plots, a vortex with positive sign is observed to detach and move downwards in the plot, which corresponds to an outwards movement in reality. Vortices shed for the upper and the lower side of the cylinder have almost no contact with each other. Vortices on each side however connect and merge with subsequent vortices of the same sign.

In Figure 6.55, a short sequence of plots presents the wake flow characteristics in a plane at y=-0.025D, in the small diameter wake. Compared to Figure 6.42, where the flow field in a plane on the diameter step was discussed, vortex shedding is not limited to the symmetry plane of the cylinder anymore. But rather, the negative vortex that has detached in the second and third plot, moves upwards, which in reality means, to one of the sides. Previous observations as presented in Figure 6.39 are therefore supported. Vortices in upper and lower planes along the cylinder span lean to the outside.
Further, the present observation shows that the condition of vortices moving to the outside is not stationary and leaning might happen periodically or unregularly for a limited period.
At the same time it is discovered that vortices are accompagnied by smaller and weaker vorticity regions. These might be connections to other vortices by small

arms, as they were previously discovered by Dunn and Tavoularis [3] (see Figure 6.48).

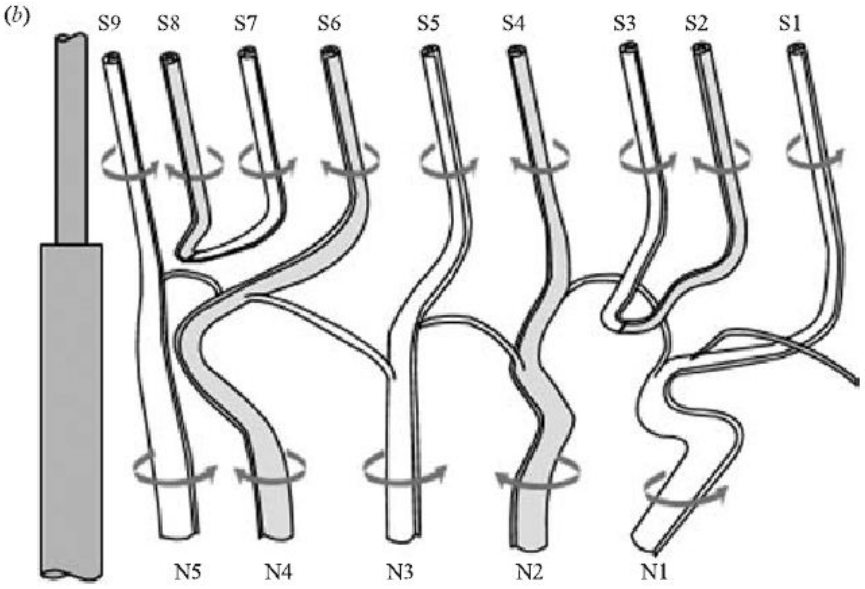


Figure 6.48: Visualization of connections between subsequent vortices by small arms, as found by Dunn and Tavoularis [3].

Finally, Figure 6.56 presents in four plots results of the measurement in a plane at y=-0.05D in the small diameter wake. Compared to the results from Figure 6.55, vortices now appear more elongated. Detachment from the eddy formation region takes place 0.5D to 1D further downstream than in the plane closer to the cylinder. Again, the statement of vortices leaning backwards is supported. While the second plot in the sequence shows indications of regular vortex shedding, in the subsequent plot two vortices are shed from the upper and the lower cylinder side at the same time. In the last plot, the negative vortex overtakes the positive vortex. From this figure it is mainly seen that the velocity with which positive and negative vortices progress, varies with time. This is assumed to be a result of vortices connecting to foregoing or subsequent vortices across the step and, depending on the progress speed of the connecting vortex, acceleration or deceleration.

The discussion of the mean wake plots supported statements in earlier Chapters and in the literature, concerning leaning of vortices backwards and outwards and the formation of connections with subsequent vortices, as well as vortices with a different peogressing speed on the other step side.

Subsequently, a spectral analysis was adopted to the data from all measurement planes. It was aimed to find out which vortex shedding cell the repective planes could be assigned to. Quantitative results of the spectral analysis in the respective planes are presented in Table 6.4, in the form of frequencies and Strouhal numbers. In addition, the eddy formation length is given.

| Location of measurement plane | Eddy formation length $L_f$ | Frequencies $f_v[\frac{1}{s}]$ | Strouhal numbers $St_D$ |
|---|---|---|---|
| y=0 | | | |
| y=0.025D | 3D | 0.0557, 0.283 | 0.0955, 0.485 |
| y=0.05D | | | |
| y=-0.025D | 2.5D | 0.0977, 0.186, 0.293, 0.394 | 0.167, 0.319, 0.502, 0.675 |
| y=-0.05D | 3.5D | 0.0977, 0.286, 0.399 | 0.167, 0.547, 0.684 |

Table 6.4: Maxima of the power spectral density from spectral analyses in different measurement planes along the cylinder span. The velocity component W was used for the calculation, as it delivers a stronger signal than the streamwise component U.

The result of the spectral analysis, which for every measurement plane was performed at the location of the strongest signal, is a graph representing the power spectral density with respect to the vortex shedding frequency. Figures 6.49 shows the result of the spectral analysis for all measurement planes.

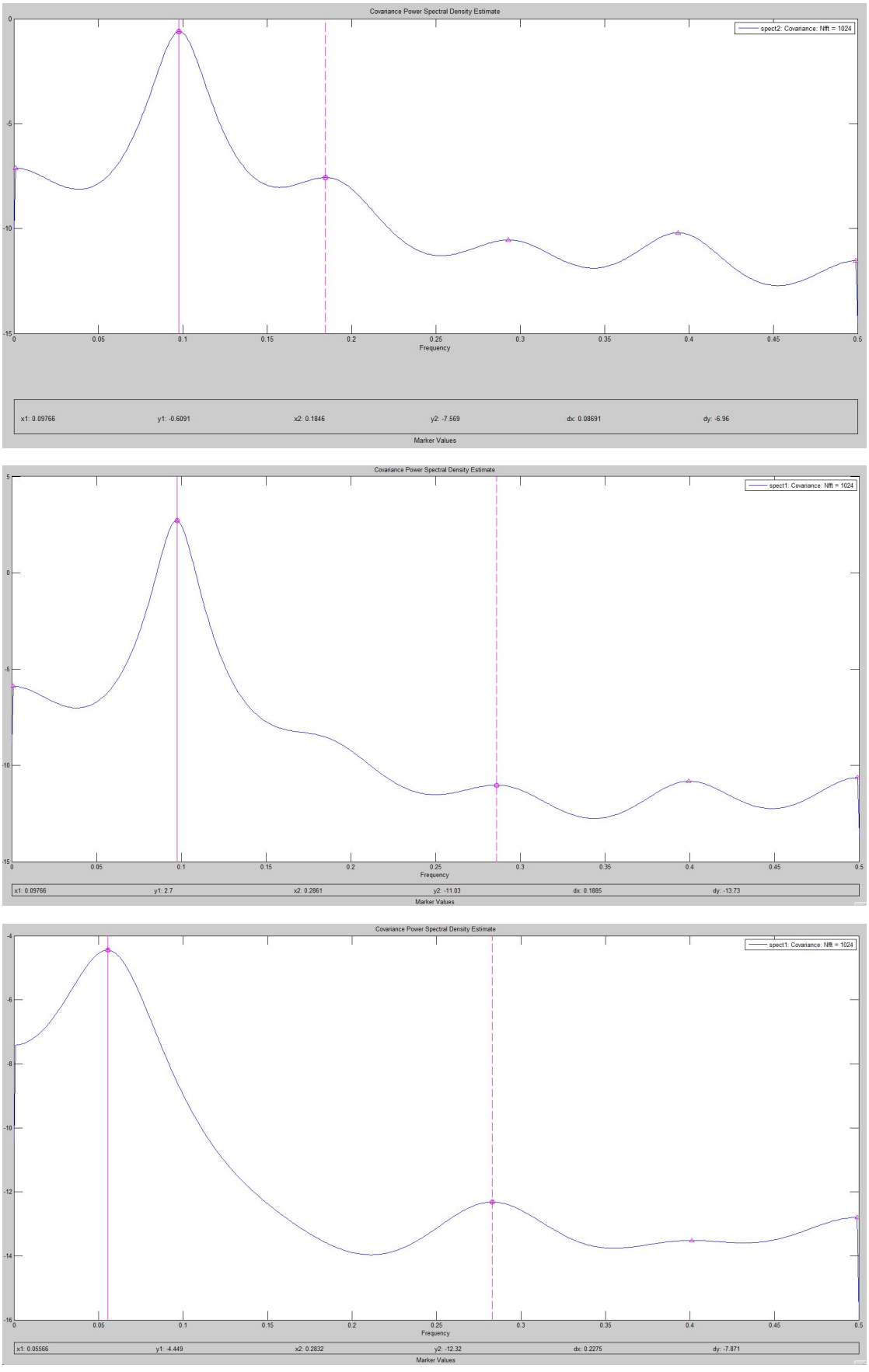


Figure 6.49: PSD from spectral analyses in several planes parallel to the x-z plane.

Previously it was shown with reference to Dunn and Tavoularis [3] that not only spanwise, but also streamwise vortices develop due to the presence of step cylinders (see Figure 6.15). In the following, the fluctuation of the spanwise velocity component V is investigated. Since V is not or only little influenced by the occurance of spanwise vortices, a high fluctuation in the spanwise component should indicate locations of spanwise vortices.

As a matter of fact, a distinct region of spanwise velocity activity is observed in all measurement planes in Figure 6.50. The strongest fluctuation is observed for the plane with zero displacement, which is located right on the step. This strengthens the assumption that the fluctuation represents a junction or an edge vortex. The fluctuation becomes weaker in the displaced measurement planes. In the small diameter wake, the fluctuation is actually only seen close to the cylinder, up to approximately x=1D. This leads to the conclusion that the junction vortex is led downwards when proceding further downstream.

All images in the figure show a region characterized by some vortex activity (magnitude about 50% of the activity close to the cylinder), located, depending on the position of the measurement plane, downstream between x=2D and x=5D. It is probable that the junction vortex rolls up here. A sketch of the drawn conclusions is presented in Figure 6.51.

Dunn and Tavoularis [3] visualized streamwise vortices by using electrolytic precipitation. Their interpretation, which is based on the analysis of video records, shows that streamwise vortices connect to spanwise vortices at approximately x=D for $Re_D = 118$ (see Figure 6.52). This might be the explanation for the region of streamwise velocity fluctuation in the present figure. It is possible that the streamwise vortices roll up due to a forming connection with spanwise vortices behind the eddy formation region.

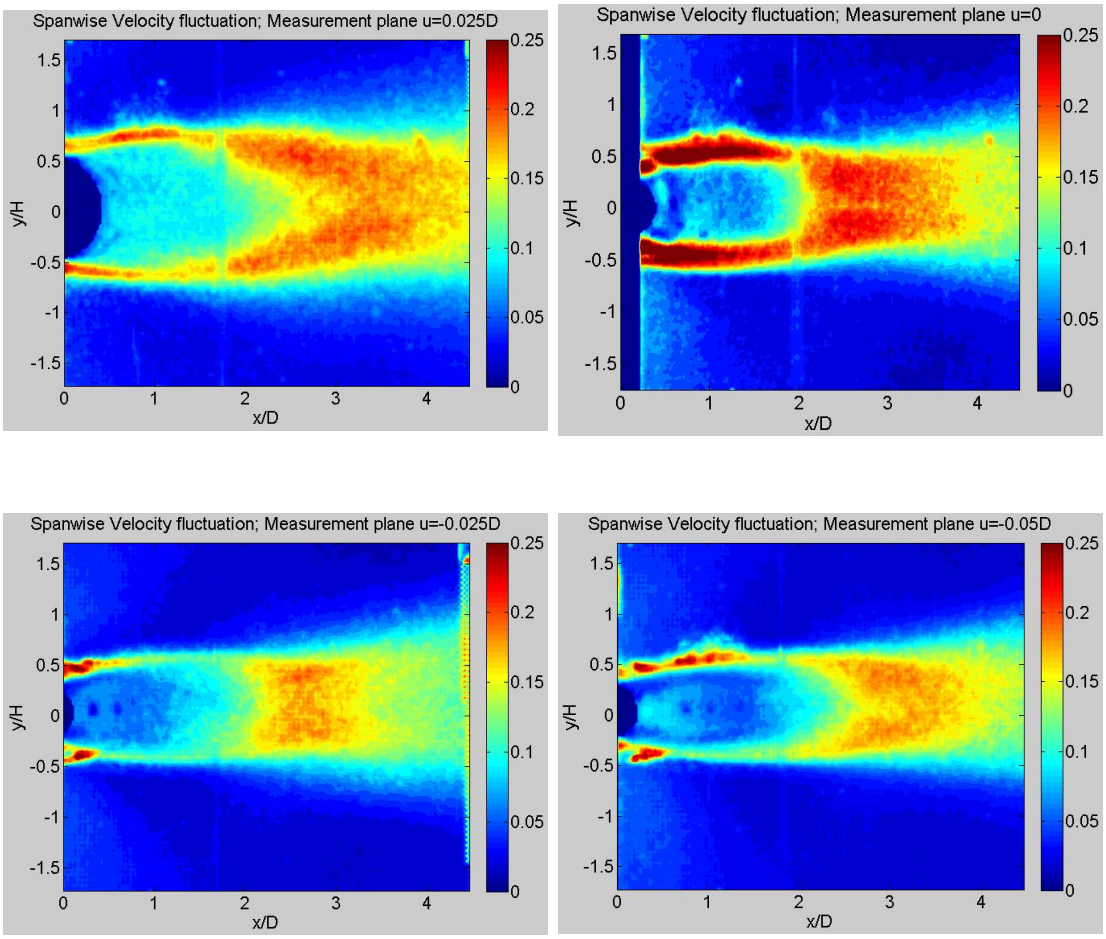


Figure 6.50: Spanwise velocity fluctuation in four measurement planes.

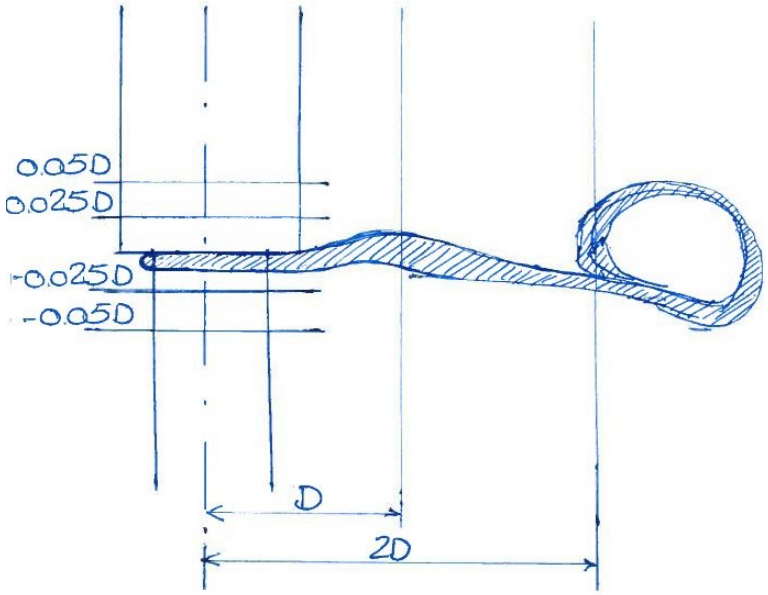


Figure 6.51: Interpretation of the results found from the evaluation of the spanwise fluctuation in several x-z planes. A streamwise vortex forms around the step, moves downwards and rolls then up further downstream than x=2D.

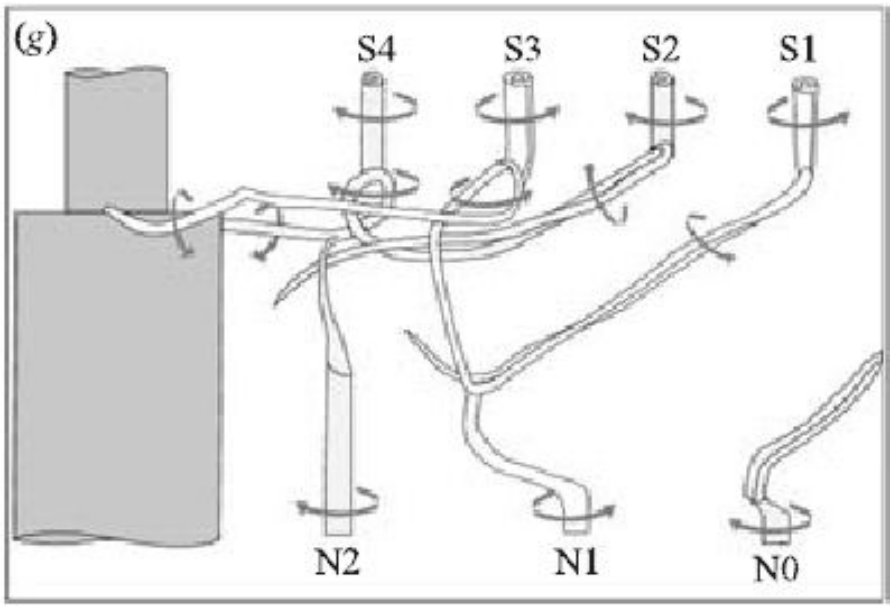


Figure 6.52: Connections of streamwise with spanwise vortices, as found by Dunn and Tavoularis [3]. In their report, they refer to the step region as N and to the region in the small diameter wake as S. This leads to the vortex annotations.

### 6.5.1 Appendix: instantaneous wake flow in the x-z plane

For visualization reasons, figures can consist of several plots distributed over multiple pages.

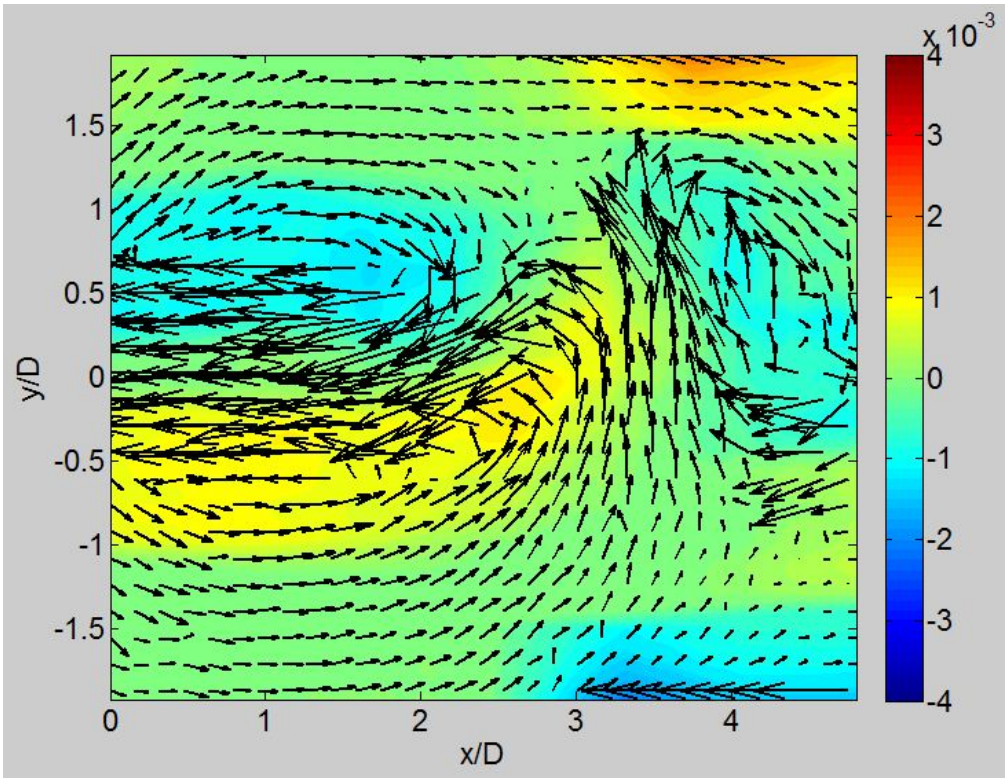


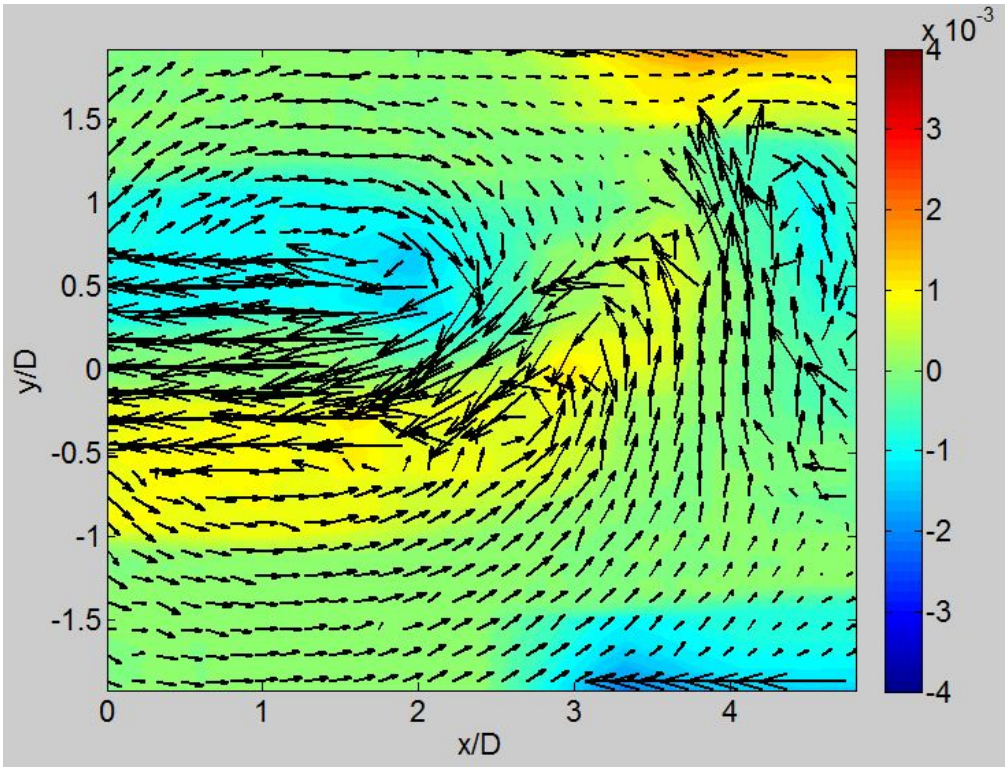

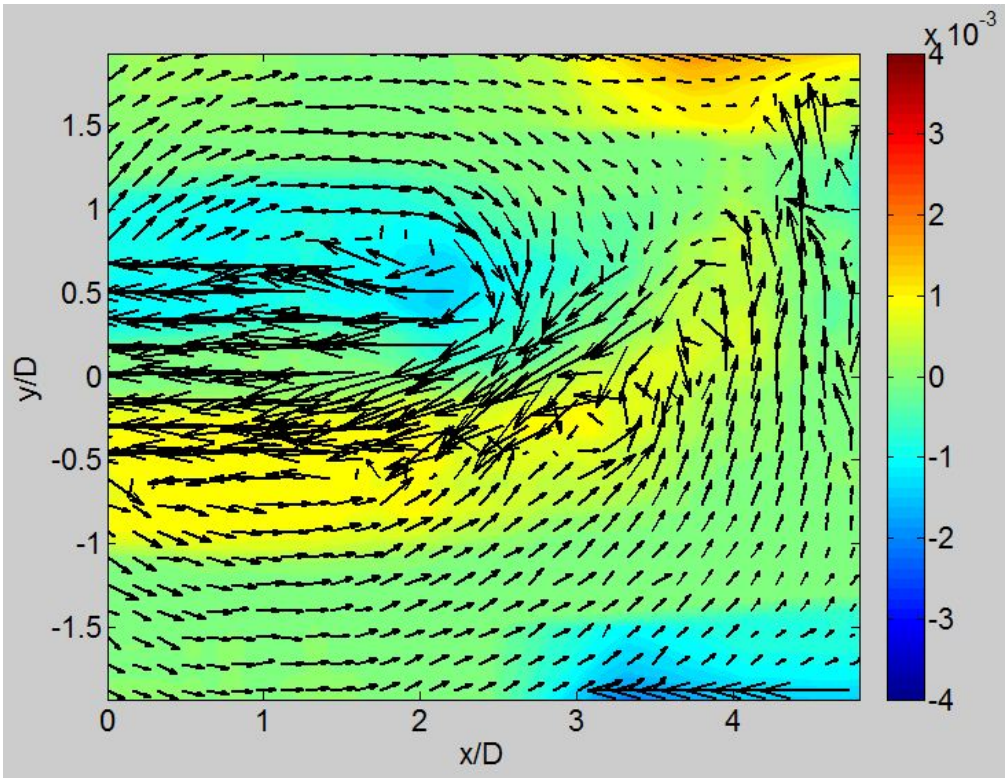


Figure 6.53: Wake flow field behind the cylinder D/d=2 in a plane at y=0.05D (large diameter wake). Time distance: $\Delta t = 1s$. Color coding: vorticity; vector plot: in-plane velocity.

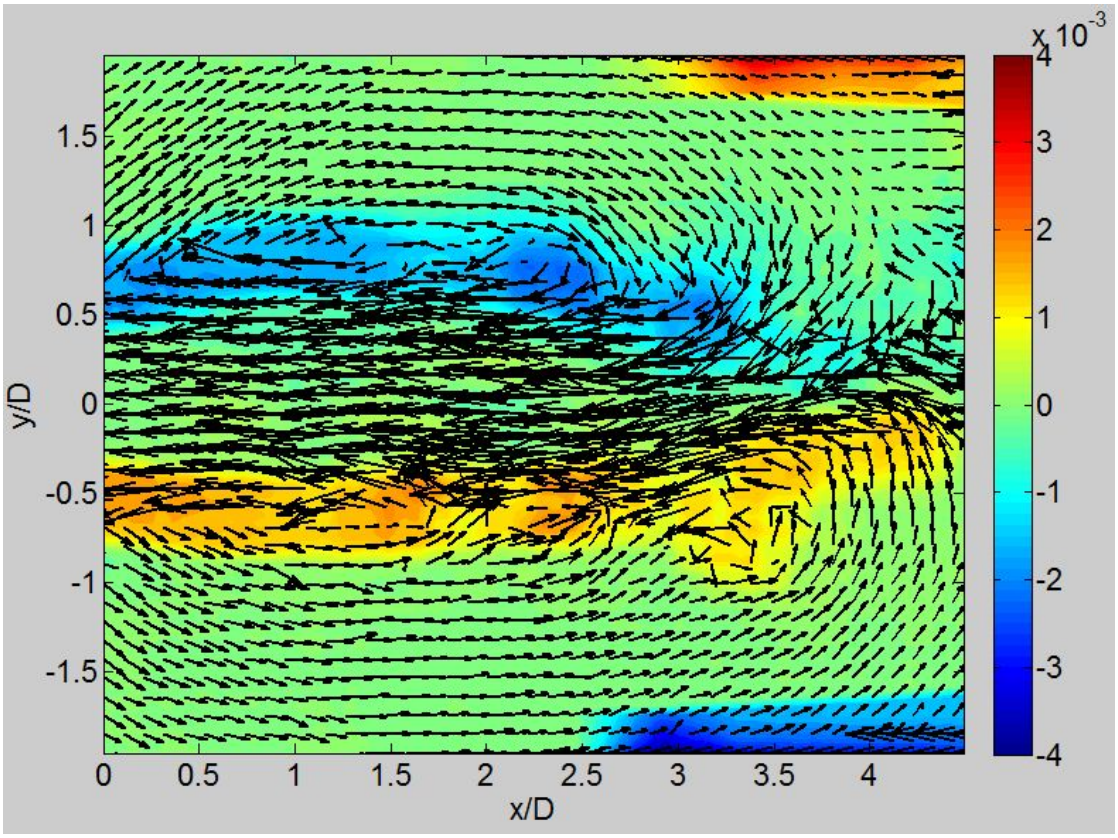

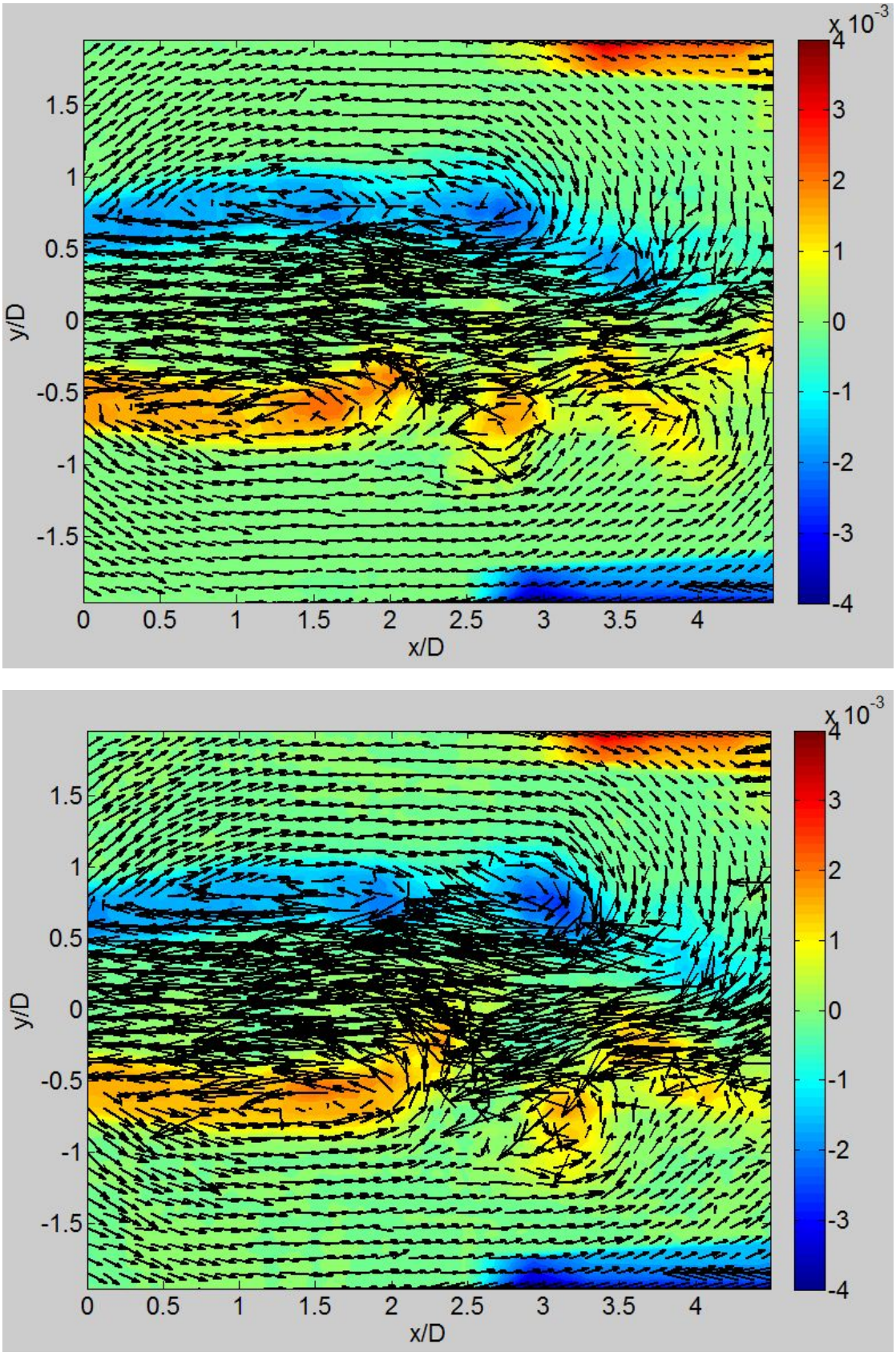


Figure 6.54: Wake flow field behind the cylinder D/d=2 in a plane at y=0.025D (large diameter wake). Time distance: $\Delta t = 2s$. Color coding: vorticity; vector plot: in-plane velocity, respective $U_{inflow}$.

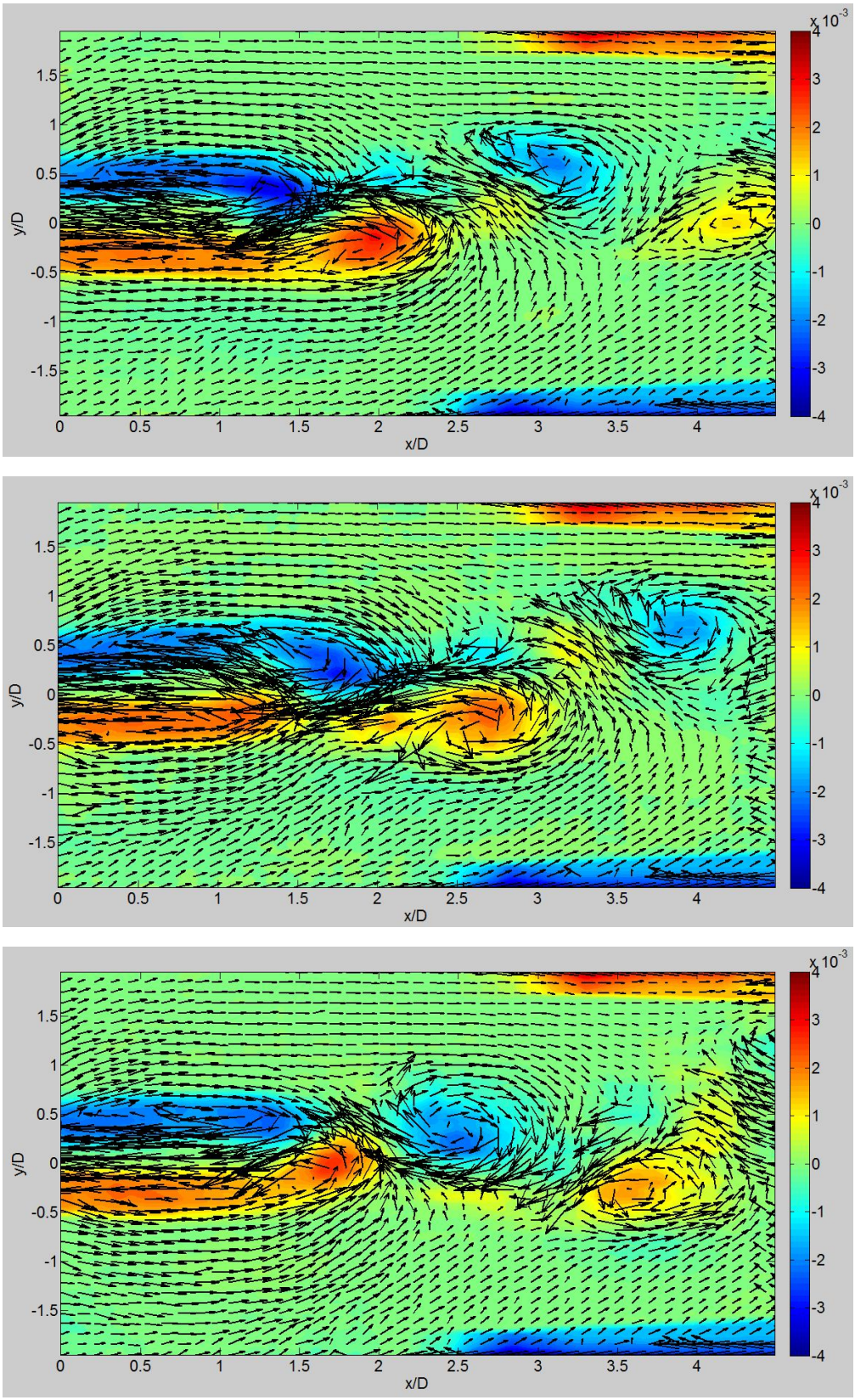


Figure 6.55: Wake flow field behind the cylinder D/d=2 in a plane at y=-0.025D (small diameter wake). Time distance: $\Delta t = 2s$. Color coding: vorticity; vector plot: in-plane velocity.

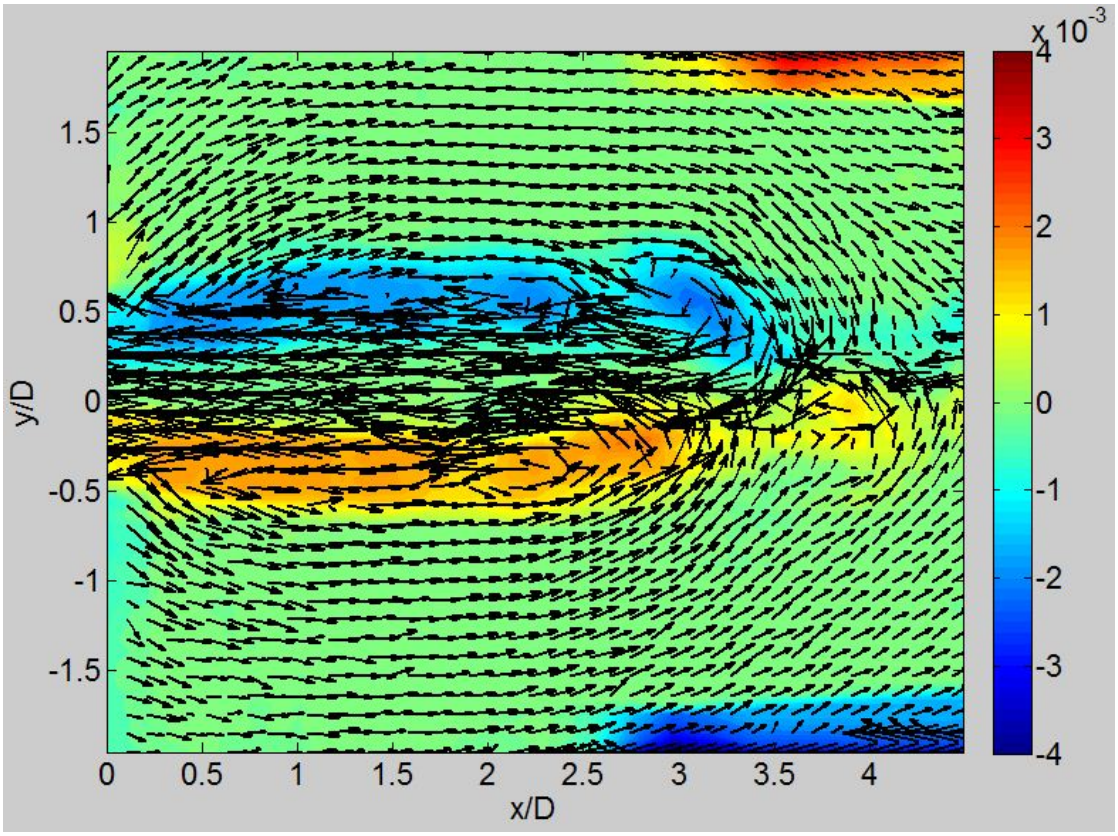
x 10^-3
4
3
2
1
0
-1
-2
-3
-4
1.5
1
0.5
0
-0.5
-1
-1.5
y/D
0
0.5
1
1.5
2
2.5
3
3.5
4
x/D

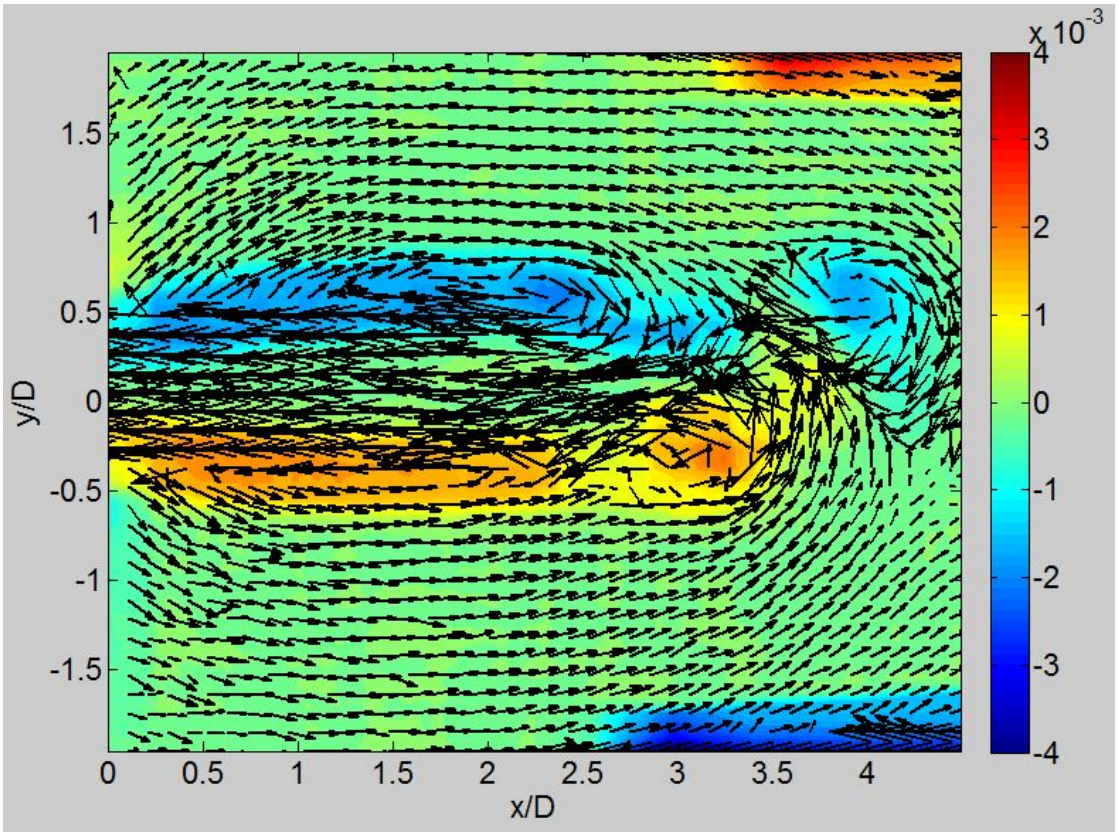
x 10^-3
4
3
2
1
0
-1
-2
-3
-4
1.5
1
0.5
0
-0.5
-1
-1.5
y/D
0
0.5
1
1.5
2
2.5
3
3.5
4
x/D

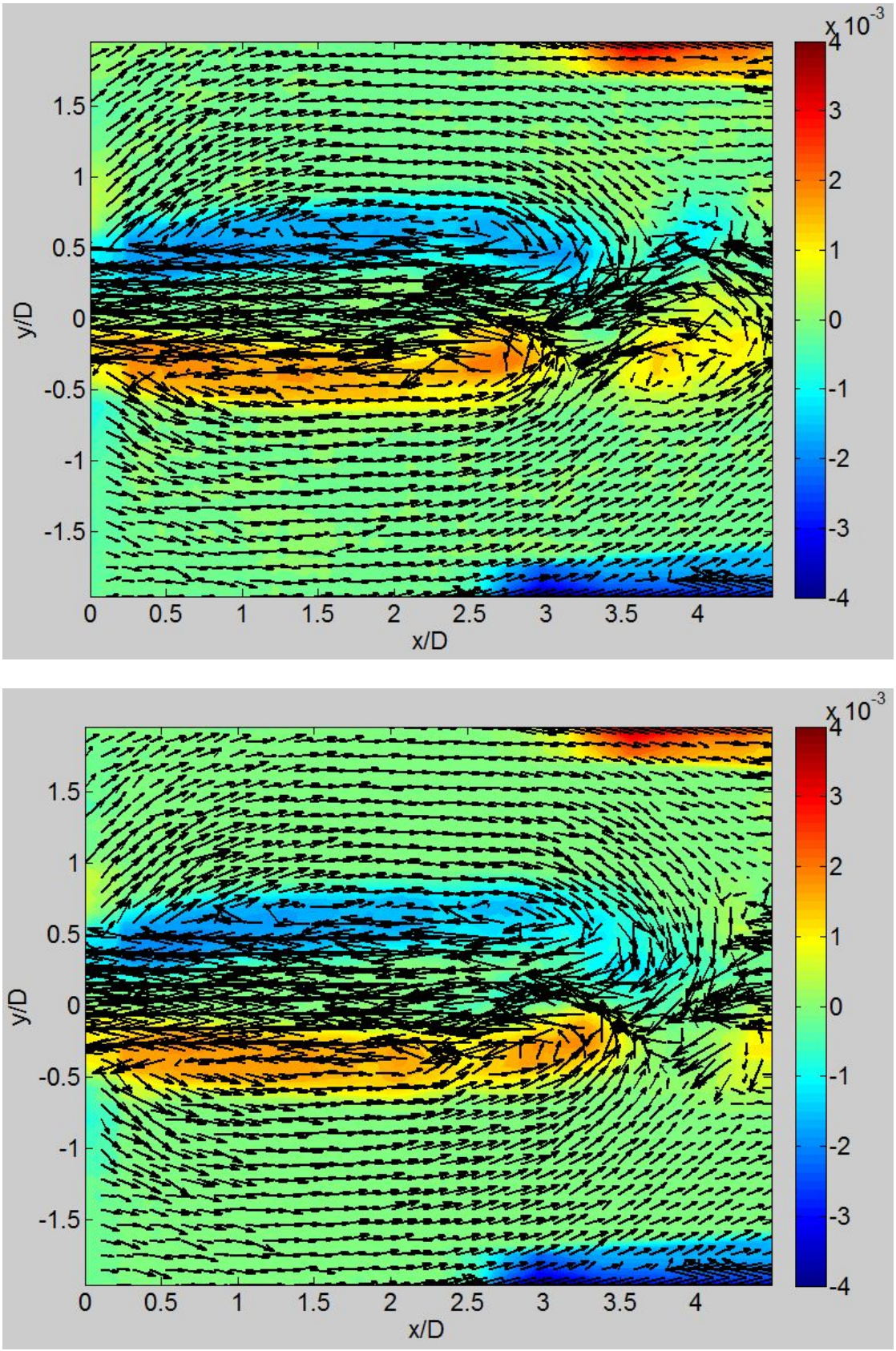


Figure 6.56: Wake flow field behind the cylinder D/d=2 in a plane at y=-0.05D (small diameter wake). Time distance: $\Delta t = 1s$. Color coding: vorticity; vector plot: in-plane velocity, respective $U_{inflow}$.

# 7 Conclusions

Flow characteristics in the wake of circular step cylinders were investigated by use of particle image velocimetry (PIV). A reference cylinder with D/d=1, as well as two step cylinders with D/d=6/5 and D/d=2 were analyzed at Reynolds numbers of $Re_D = 2243.5$, $Re_D = 12820.5$ and $Re_D = 51282.1$. Measurements were performed in both vertical and horizontal planes.

A significant influence of Reynolds number and diameter step size was discovered. It was found that an increase in Reynolds number causes a shift in flow development further upstream. The eddy formation length $L_f$ is shortened significantly by a Reynolds number increase. At the same time, the influence of turbulence increases with a higher Reynolds number.

An increasing diameter ratio leads to an increase in the number of vortex shedding cells. For the cylinder with the largest step, vortex shedding frequencies behind large and small diameter ratio differed in such intensity that vortices came out of phase and formed connections with subsequent vortices on the same side of the step.

In addition to spanwise vortices, a streamwise vortex was observed to develop around the step of the cylinder. An analysis of the spanwise velocity fluctuation led to the conclusion that the streamwise vortex forms connections with spanwise vortices at a location downstream of the cylinder.

The experimental results were found in agreement with previous results of experimental studies [3, 9, 11, 12] and numerical investigations [13]. PIV proved to be a sufficient method for the investigation of velocity and vorticity in the wake of step cylinders. The resolution of the postprocessed data was effectual with regard to occurrances in the flow field.

A limit of the setup was the restriction of the camera view field. With a field of view further expanded in y-direction, it might be easier to identify distinct vortex shedding cells. Probably the "leaning-back" that was observed for the vortices behind step cylinders takes place only close to the cylinder. The connection of this region to vortices in the large diameter wake would be interesting to observe. A limit of the PIV system in this connection was discovered when performing experiments with a thinner cylinder model. For a cylinder with a large diameter ratio of

D=12mm, it was not possible to observe characteristic flow features. One reason for this might be the comparably high thickness of the laser light sheet.
For the future, it might be of interest to combine PIV studies in the facilities with LDV measurements of the flow behind step cylinders. For cases with such three-dimensional flow development, it might also be considered to apply a tomographic PIV system.

ACKNOWLEDGEMENTS

With thanks to Professor Bjørnar Pettersen, Dr. Jan Visscher, Dr. Chittiappa Muthanna, Knut Arne Hegstad and the wonderful team in the NTNU workshop.

# References


[1] Artana, G., Sosa, R., Moreau, E. and Touchard, G., *Control of the near-wake flow around a circular cylinder with electrohydrodynamics actuators*, Experiments in Fluids 35, pp. 580-588 2003

[2] Dawson, D., *Wind over deep water*, http://www.compositesworld.com/articles/wind-over-deep-water 2011

[3] Dunn,W. and Tavoularis, S., *Experimental studies of vortices shed from cylinders with a step-change in diameter*, J. Fluid Mech. 555, 409-437 2006

[4] Green, R. B. and Gerrard, J. H., *Vorticity measurements in the near wake of a circular cylinder at low Reynolds numbers*, J. Fluid Mech., Vol. 246, pp. 675-691 1993

[5] Griffin, O. M., *A note on bluff body vortex formation*, J. Fluid Mech., Vol. 284, pp. 217-224 1995

[6] Von Kármán, T., *Über den Mechanismus des Widerstandes, den ein bewegter Körper in einer Flüssigkeit erzeugt*, Math. Phys. Klasse, Part1: 509-515, Part2: 547-556, Göttingen 1911

[7] Kestin, J., Sokolov, M., Wakeham, W. A., *Viscosity of Liquid Water in the Range -8 deg C to 150 deg C*, J. Phys. Chem. Ref. Data, Vol. 7, No. 3 1978

[8] Ko, N. W. M., Chan, A. S. K. and Kan, S. M., *Flow behind stepped and tapered coaxial cylinders*, Proc. 2nd Asian Congr. Fluid Mech., pp. 755-760 Beijing, 1983

[9] Lewis, C.G. and Gharib, M., *An exploration of the wake three dimensionalities caused by a local discontinuity in cylinder diameter*, Phys. Fluids A 4 (1), 104-117 1992

[10] Morton, C. and Yarusevych, S., *Vortex shedding in the wake of a step cylinder*, Physics of Fluids 22, 083602 2010

[11] Morton,C. and Yarusevych, S., *A combined experimental and numerical study of flow past a single step cylinder*, European Fluids Engineering Summer Meeting, Montreal, August 2010

[12] Morton,C. and Yarusevych, S., *Cross flow over cylinders with two stepwise discontinuities in diameter*, 7th International Symposium on Turbulence and Shear Flow Phenomena (TSFP-7), Ottawa, July 2011

[13] Morton, C., Yarusevych, S. and Carvajal-Mariscal, I., *Study of flow over a step cylinder*, Applied Mechanics and Materials, Vol 15, pp. 9-14 2009

[14] Norberg, C., *An experimental Study of the Flow Around Cylinders Joined with a Step in the Diameter*, 11th Australasian Fluid Mechanics Conference, 507-510, Hobart 1992

[15] Pettersen, B., *TMR4247-Marin Teknikk 3- Hydrodynamikk*, Lecture notes in the course TMR4247, NTNU, 2007

[16] Sumer, Mutlu B. and Fredsøe,J., *Hydrodynamics around cylindrical structures*, Advanced Series on Ocean Engineering, Vol. 26 2006

[17] Techet, A. H., *Vortex Induced Vibrations*, Lecture note Design principles for Ocean Vehicles, 2005

[18] Teutsch, I., *Experimental investigation of the flow field behind a stepped cylinder*, Project report, MARINTEK, Trondheim, September 2011

[19] Vallès, B., Andersson, H. I. and Jenssen, C. B., *Direct-mode interactions in the wake behind a stepped cylinder*, Physics of Fluids, Vol. 14, No. 4, April 2002

[20] Visscher, J., Pettersen, B. and Andersson, H. I., *PIV study on the turbulent wake behind tapered cylinders*, Advances in Turbulence XI, pp. 254-256 2007

[21] Visscher, J., *Application of PIV in marine engineering. Tchnical report.*, Doctoral Thesis, Norwegian University of Science and Technology 2011

[22] Zdravkovich, M. M., *Flow Around Circular Cylinders, Vol.1 and 2*, Oxford University Press, 1997 and 2003

[23] http://www.onera.fr/dafe-en/particle-image-velocimetry/piv.php Last updated 2 May 2011